

EFFECT OF MN ON HARDENABILITY AND GALVANIZING OF DP
STEELS

HARDENABILITY IMPROVEMENTS AND RATE-LIMITING REACTIONS
DURING HOT-DIP GALVANIZING OF HIGH-MN DUAL-PHASE
STEELS

By
RICHARD J. MEGUERIAN, B.ENG

A Thesis
Submitted to the School of Graduate Studies
in Partial Fulfilment of the Requirements
for the Degree
Master of Applied Science

McMaster University

©Copyright by Richard Meguerian, September 2007

MASTER OF APPLIED SCIENCE (2007)
(Department of Materials Science and Engineering)

McMaster University
Hamilton, Ontario

TITLE: Hardenability Improvements and Rate-Limiting Reactions During Hot-Dip Galvanizing of High-Mn Dual-Phase Steels

AUTHOR: Richard Meguerian, B.Eng (McMaster University)

SUPERVISOR: Dr. Joseph R. McDermid

NUMBER OF PAGES: xiii, 117

Abstract

Intercritically annealed steels, such as dual-phase steels, have found widespread use in automotive structural components due to their high strength and ductility. Elements such as Mn, Al and Si, added to improve the mechanical properties are selectively oxidized during heat treatment and limit the ability of the alloy to be reactively wet during continuous hot-dip galvanizing. Subsequently, a limit has been placed on the amount of alloy which can be used if the steel is to be subsequently galvanized. The specifics of this limit have not been explored in detail, nor has the mechanism of decreased wettability been well demonstrated in the literature other than to say that the galvanizing reaction is limited by oxides on the surface.

Using a force balance, it is shown that the presence of MnO on the surface of steels greatly reduces the wettability with a typical galvanizing bath (Zn-0.2wt%Al, Fe-saturated, 460°C). Furthermore, it was determined that this is caused by the additional and rate-limiting step of aluminothermic reduction of the oxide layer with the bath Al, required for subsequent inhibition layer formation. By using a low pO_2 during annealing, the wettability was improved by reducing the thickness of the MnO layer when compared to intermediate and industrially common values of pO_2 . Using a high pO_2 also resulted in improved wettability since the internal oxide which was formed did not reduce the wettability since it was not exposed to the bath alloy.

Improvements in hardenability were also explored via dilatometry showing that the formation of bainite is delayed with increasing Mn content, as well as a decrease in transformation temperatures from γ during cooling (i.e. M_S and B_S). At $\sim 5\text{wt}\%$ Mn, only the transformation to α_M could be observed. This opens the door to higher strength, galvanized steels - as well as possibly galvanized martensitic steels.

Acknowledgements

This work could not have been completed without the direction and guidance of Dr. McDermid. Our shared curiosity spurred insightful discussions and spirited debates which led to my continued ambition for this project in a topic which is relatively young and unexplored.

The friendship and discussions with my colleagues in JHE/A203 provided the perfect balance of distraction and focus to kept me motivated and grounded; creating an environment conducive to learning and discover - ideal for engineering research.

Financial aid from the McMaster Steel Research Centre, NSERC, and Stelco, Inc is greatly appreciated. As well, the use of XPS at Dofasco, Inc. resulted in much of my analysis being done much faster and with greater accuracy than would be possible otherwise. CANMET-MTL, through the AUAF, played the invaluable role of providing the experimental steel grades as well as allowing me to spend two weeks occupying their dilatometer and never hesitated to help in any way they could.

Finally, I can't forget to thank Lydja – who put up with my frustration and distraction over the last two years when many aspects of my personal life should have taken precedent over my work – but didn't.

Table of Contents

Abstract	iii
Acknowledgements	iv
List of Figures	viii
List of Tables	xiii
Chapter 1 Introduction	1
Chapter 2 Literature Review	3
2.1 Introduction	3
2.2 Intercritically Annealed Steels	3
2.2.1 Development of Strength and Ductility	4
2.3 Continuous Hot-Dip Galvanizing	9
2.3.1 Control of Oxidation Potential During Annealing	11
2.3.2 Reaction Products Formed upon Dipping	16
2.3.3 Effect of Surface Species on Reactive Wetting	19
2.3.4 Aluminothermic Reduction of MnO	21
2.3.5 Increasing the Wettability of High-Mn Steels	23
2.4 Quantification of Wetting Processes	25
2.4.1 Motivation	25
2.4.2 Young's Equation and the Triple Line	27
2.4.3 Current Methods Used to Measure Reactive Wetting	30

Chapter 3	Research Objectives	35
Chapter 4	Experimental Method	36
4.1	Introduction	36
4.2	Materials Systems Utilized	37
4.2.1	Substrates	37
4.2.2	Reactive Wetting Bath	37
4.3	Transformations During Continuous Cooling	38
4.4	Substrate Heat Treatments	41
4.4.1	Sample Preparation	41
4.4.2	Thermal Profiles	41
4.4.3	Annealing Atmospheres	42
4.4.4	Analysis of Oxide(s) Formed	44
4.5	Reduction of MnO with bath Al	46
4.6	Reactive Wetting Kinetics/Wettability	48
4.6.1	Effect of the contact angle on F_{buoyancy}	53
4.6.2	Observation of Interfacial Reaction Products	55
Chapter 5	Results	56
5.1	Introduction	56
5.2	Hardenability Variations With Mn Content	56
5.3	Selective Oxidation During Annealing	59
5.4	In-Situ Reduction of MnO	71

5.4.1	Reaction with Pure Zn Bath	71
5.4.2	Reaction with Zn-0.2wt%Al (Zn-Al) Bath	74
5.5	Reactive Wetting Measurements	76
Chapter 6	Discussion	86
6.1	Increasing Hardenability with Mn Additions	86
6.2	Oxidation Growth Modes During Annealing	88
6.3	Relating Surface State to Wettability	90
Chapter 7	Conclusions	96
Chapter 8	Recommendations	98
	Bibliography	100
	Appendix A Continuous Cooling Transformation Diagrams	105
	Appendix B Initial Wetting Force as a Measure of Reactive Wetting	112
	Appendix C Measurements and Analysis Using a Force Balance	115

List of Figures

1.1	Tensile strength-elongation relationship for automotive steels	2
2.1	Typical dual-phase steel microstructure	4
2.2	Fe-rich portion of Fe-C phase diagram	5
2.3	Effect of C on α_M formation	6
2.4	Strength-ductility-martensite relationships	7
2.5	M_S temperature and critical cooling rate as a function of Mn content . .	10
2.6	Effect of increasing Mn content on hardenability	10
2.7	Schematic illustration of a continuous galvanizing line	12
2.8	Calculation of atmospheric water content as a function of dew point . . .	13
2.9	Oxidation potential as a function of temperature and gas composition . .	14
2.10	Effect of Mn on oxides formed during annealing	15
2.11	Oxide surface coverage versus bulk composition	16
2.12	Zn-rich portion of the <i>metastable</i> Zn-Fe-Al phase diagram at 460°C . . .	17
2.13	Al, Zn, and Fe profiles through the steel/coating interface	18
2.14	Fe-Zn outburst after prolonged dipping (3600s) at 450°C	19
2.15	Un-wettable surface created with a Mn-Al steel	20
2.16	TEM-based EDX line scan of galvanized DP steel	22
2.17	Depth profiles for a dual-phase steel annealed at various dew points . . .	24
2.18	Surface composition vs. annealing dew point	25
2.19	Interfacial layer growth during galvanizing	26

2.20	Illustration of Young's equation and contact angle geometry	28
2.21	Progression of triple line configuration in reactive wetting	29
2.22	Schematic of sessile drop contact angle measurement	31
2.23	Rapid spreading of liquid sessile drop experiment	32
2.24	Contact angle evolution during sessile drop experiment	33
2.25	Effect of surface enrichment on wetting	34
4.1	Schematic illustration of the continuous hot-dip galvanizing process . . .	36
4.2	Dilation curve and transformation temperature identification	38
4.3	Dilatometer and sample set-up for hardenability measurements	39
4.4	Thermal cycle used in dilatometry experiments	40
4.5	Effect of Mn on transformation temperatures for a Fe-0.07C- <i>x</i> Mn alloy .	42
4.6	Thermal profile used for surface modification experiments	43
4.7	XPS survey spectrum for annealed CMn sample	45
4.8	Heat treatment used for reduction of MnO _{<i>x</i>} to MnO	47
4.9	Deposited film oxidation state and thickness	48
4.10	EDX line scan through deposited MnO film	49
4.11	Schematic illustration of the force balance simulator	50
4.12	Sample geometry used for reactive wetting experiments	51
4.13	Thermal profile used for reactive wetting experiments	52
4.14	Geometry and force balance used to determine wetting force	53
4.15	Effect of contact angle on buoyancy	54

5.1	Determined transformation temperatures as a function of Mn content . . .	57
5.2	Fe-rich portion of the Fe-Mn phase diagram	58
5.3	M_S and M_F transformation temperatures as a function of Mn content . .	58
5.4	Variation of the bainite transformation field with Mn content	59
5.5	Compositional depth profiles of the as-received samples	61
5.6	Partial XPS spectra showing Mn segregation to steel surface	62
5.7	Compositional depth profiles for IF after heat treatment	63
5.8	Compositional depth profiles for CMn after heat treatment	64
5.9	Compositional depth profiles for DP590 after heat treatment	65
5.10	Compositional depth profiles for DP-1 after heat treatment	66
5.11	Compositional depth profiles for DP-2 after heat treatment	67
5.12	Compositional depth profiles for DP-3 after heat treatment	68
5.13	Compositional depth profiles for DP-4 after heat treatment	69
5.14	Change in oxide thickness from -50°C to -30°C dew point	70
5.15	Interfacial microstructure of sample dipped in pure Zn for 60s	72
5.16	EDX line scan of steel/coating interface in samples dipped in pure Zn . .	73
5.17	Fe-Zn outburst through Fe-oxide	74
5.18	Details of sample immersed in Zn-Al bath for 5s	75
5.19	EDX line scan through interface for sample dipped in Zn-Al bath for 5s .	76
5.20	EDX line scan through steel/coating interface in Zn-Al dipped samples .	77
5.21	Example wetting curve	78

5.22	Effect of dew point on wetting curves for DP-3	79
5.23	Effect of Mn on wetting for samples annealed at a dew point of -30°C	80
5.24	Effect of Mn content on initial wetting force	81
5.25	Initial wetting force vs. dew point for all samples	82
5.26	Initial wetting force vs. pO_2 for all samples	83
5.27	Impact of Mn content on interfacial structures	85
6.1	Effect of Mn content on delaying bainite transformation	87
6.2	M_S and M_F transformation temperatures as a function of Mn content	88
6.3	Partitioning of C and Mn to γ during intercritical annealing	89
6.4	Effect of dew point on Mn enrichment depth (oxide thickness)	90
6.5	Effect of oxide thickness on wetting	92
6.6	Reaction in front of triple line during reactive wetting	93
6.7	Correspondence between grain boundaries and outbursts	95
7.1	Aluminothermic reduction in galvanizing process steps	97
A.1	CCT diagram generated for CMn alloy	106
A.2	CCT diagram generated for DP590 alloy	107
A.3	CCT diagram generated for DP-1 alloy	108
A.4	CCT diagram generated for DP-2 alloy	109
A.5	CCT diagram generated for DP-3 alloy	110
A.6	CCT diagram generated for DP-4 alloy	111

B.1	Effect of γ_{LV} on contact angle calculation	113
B.2	Effect of θ on $\frac{\partial\theta}{\partial t}$	114
C.1	Effect of steel thickness on the dynamic response of the electrobalance . .	116
C.2	Schemataic illustration of dynamic loss effect in reactive wetting tests . .	117

List of Tables

2.1	Typical DP steel compositions	5
2.2	Impact of alloying additions on α_M formation	9
4.1	Composition of substrates used in this study	37
4.2	Annealing temperatures and oxidation potentials used in experiments . .	43
4.3	MnO reduction sample processing variables	47
5.1	Experimentally determined transformation temperatures upon heating .	57

Chapter 1

Introduction

As one of the greatest contributors to greenhouse gas emissions, there seems to be an unwavering effort to decrease the weight of automobiles. One way this has and continues to be accomplished is by utilizing higher strength alloys in load-bearing and/or crash-critical components. As with the previous generation of steels, there is a requirement for corrosion resistance which exceeds the intrinsic resistance of the alloy. To accomplish this, the added protection of a surface treatment is utilized. Moreover, as the trend towards higher strength materials in automobiles continues, the smaller cross-sections used to decrease weight will succumb to corrosion perforation more quickly – increasing the need for and understanding of corrosion protection.

Galvanizing is the main method with which these steels are protected from corrosion. Having zinc (Zn) on the surface of the steel provides protection in two ways. First, as the name implies, it provides galvanic protection. Zn, being much less noble than the steel substrate, oxidizes sacrificially; greatly decreasing the rate of attack. Second, it provides a physical barrier between the substrate and the corrosive environment.

Within galvanizing, there are several sub-fields defined by distinct processing routes to deposit the Zn on steel. The first and least commonly used method is electrogalvanizing. This technique involves the electrolytic deposition of Zn onto the steel surface. As with most electrochemical techniques, this is suited to small, high value-added and even batch-type operations because of the expense associated with

it. The most common technique is hot-dip processing; referring to dipping the substrate in a molten bath to form the coating. This can be done both in a batch process and continuously, the batch technique being used mainly for products which are already in their final, or near-final shape. In the case of sheet products which are to be subsequently formed, continuous hot-dip galvanizing is used. In the following text, the term galvanizing will be used to refer to *continuous hot-dip galvanizing*.

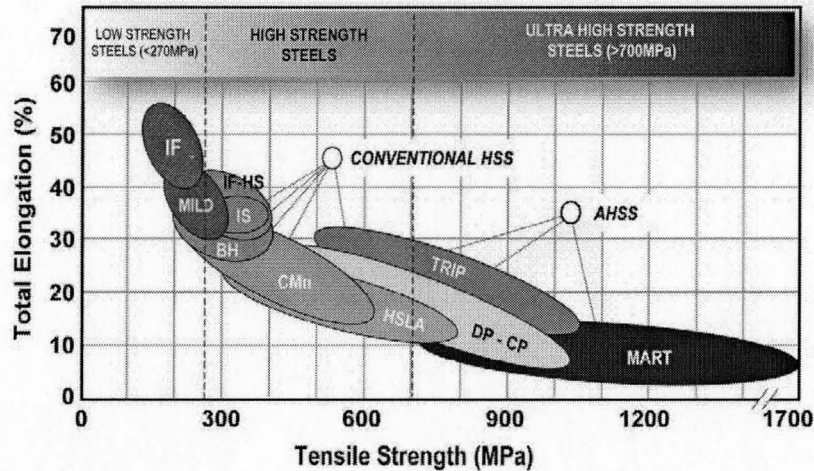


Figure 1.1: Tensile strength-elongation relationship for automotive steels and the categories they fall under. (ULSAB-AVC report, International Iron and Steel Institute, 2002)

When considering materials for forming operations, three properties are paramount. They are yield strength (YS), tensile or ultimate tensile strength (UTS) and ductility or elongation. A trade-off always exists between these properties as illustrated in figure 1.1, where an ideal material would possess both high tensile strength and elongation (top, right and empty quadrant of figure 1.1). The steels considered in this work are mainly dual-phase (DP) steels and tend towards martensitic (MART) steels. They comprise some of the strongest steels used both currently and in the near future in automobiles and are commonly referred to as advanced high-strength steels (AHSS).

Chapter 2

Literature Review

2.1 Introduction

This chapter will focus on the following topics related to continuous hot-dip galvanizing:

- Processing and properties of intercritically annealed steels
- Reactions in the galvanizing process
- Quantification of wetting phenomena as it applies to galvanizing

Particular emphasis will be placed on the effect of increasing the Mn content of the steel substrate on each of these topics.

2.2 Intercritically Annealed Steels

The term intercritically annealed steels refers to steels annealed at a temperature greater than the A_{c1} temperature[†] and below the A_{c3} temperature[‡]; referred to as the intercritical region. During intercritical annealing, pearlite present in the as-rolled microstructure transforms to C-rich austenite (γ) and, upon sufficiently rapid

[†] A_{c1} : temperature required to start forming γ -austenite during heating.

[‡] A_{c3} : temperature required to finish the transformation to γ -austenite during heating.

cooling, some or all of this γ will transform to harder phases such as martensite (α_M) or bainite (Nishiyama 1978).

Many materials fit into this category and are differentiated by the type and amount of each phase present after intercritical annealing. Two such examples are transformation-induced plasticity (TRIP) steels and dual-phase (DP) steels – the latter being the focus of this work. An intercritically annealed and quenched DP steel microstructure is shown in figure 2.1.

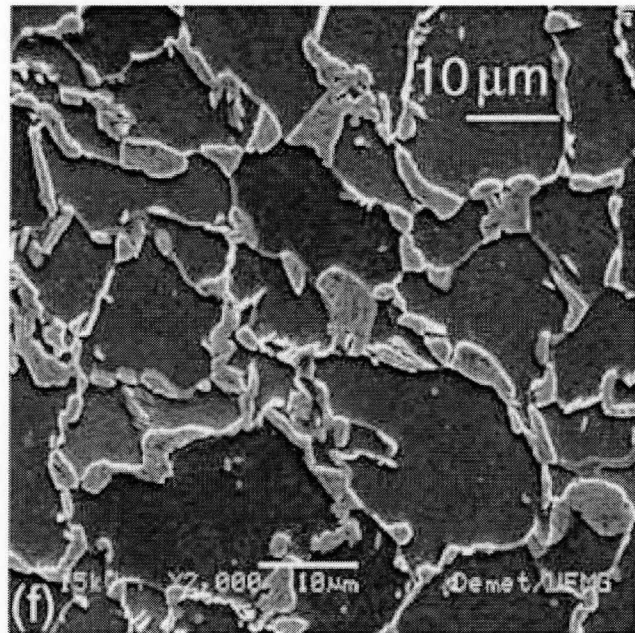


Figure 2.1: Typical post-annealing microstructure of a dual-phase steel with a dispersement of α_M (light, interconnected phase) in a matrix of α (dark phase). From Rocha et al. 2005

Typically, DP steels contain a variety of alloying additions, but the common range of major elements is listed in table 2.1.

2.2.1 Development of Strength and Ductility

Since these alloys are used in automotive structures, they are required to possess high strength. During forming operations to manufacture final components, extensive

Table 2.1: Composition range of typical DP steels (in wt%) from Oren and Goodwin (2004).

Element	Typical Content
C	0.06–0.20
Mn	1.0–2.5
Si	0.03–2.0
P	0.02–0.11
Nb	$\lesssim 0.13$
Ti	$\lesssim 0.05$

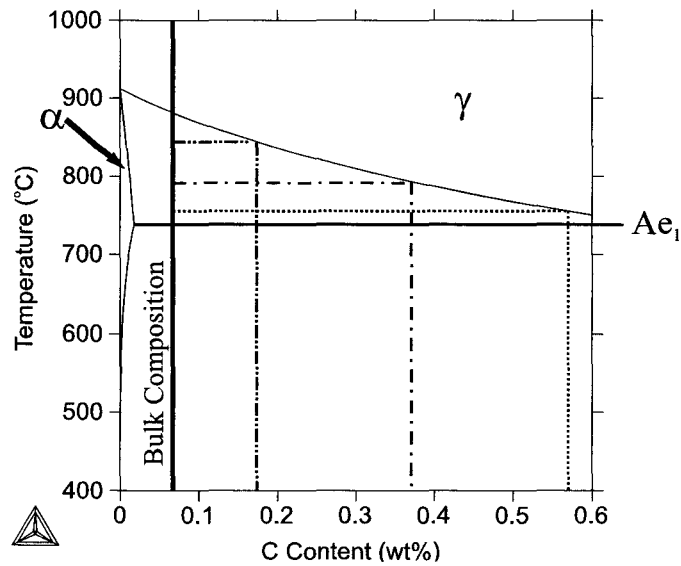


Figure 2.2: Partial Fe-C phase diagram exemplifying the effect of temperature on the amount of γ formed during annealing in the $\gamma + \alpha$ two-phase region and its C content. Calculated with Thermo-Calc® and the TCS steel database v.2.

deformation takes place; requiring that these materials also have high ductility. This combination of properties is achieved by altering the amount and morphology of the phases present in the final product (Speich and Miller 1979). For a fixed composition, this can be done by altering the intercritical annealing temperature, which affects the fraction of γ , as well as its C-content as shown in figure 2.2. For instance, an increase in annealing temperature (while remaining in the intercritical region) has two effects on the phase portrait: it increases the amount of γ , and decreases the carbon content

of the γ ; offering more γ to transform to α_M but decreasing its hardenability[§]. In figure 2.3, Speich and Miller (1979) have shown that increasing the volume fraction of γ by increasing the intercritical annealing temperature results in an increased volume fraction of α_M in a 1.5wt% Mn steel.

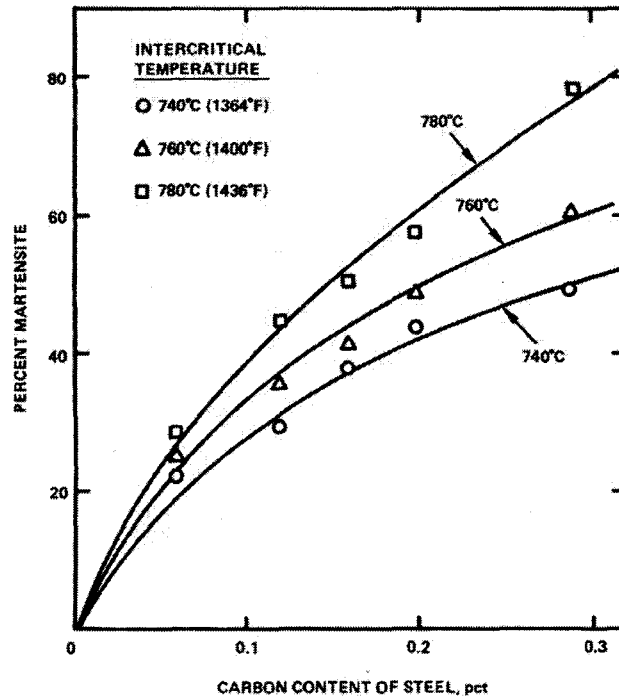


Figure 2.3: Relationship between C content and intercritical annealing temperature on α_M formation in Fe-xC-1.5Mn steels (Speich and Miller 1979)

After intercritical annealing, the microstructure of DP steels ideally consist of a matrix of α -ferrite and finely dispersed α_M (figure 2.1), effectively forming a composite of hard particles in a ductile matrix. Intrinsically, α_M is quite brittle and significantly decreases the ductility of the alloy but increases its strength (figure 2.4). Since α_M and bainite are not phases observed at equilibrium, the rate of cooling from intercritical annealing also plays a key role in the final phase portrait of these steels (Speich and Miller 1979). Relationships exist between composition and critical cool-

[§] hardenability: the propensity to transform to a harder, non-equilibrium phase (bainite and/or martensite)

ing rates to form a specific volume fraction of α_M . A comprehensive review of the effects of alloy content on transformations during continuous cooling can be found in the work of Zhao (1992). The simplest way to define hardenability is by a continuous cooling-transformation (CCT) diagram. An alloy with increased hardenability will form harder, non-ferritic phases at lower cooling rates, and therefore the nose of the CCT curve will be pushed to longer times.

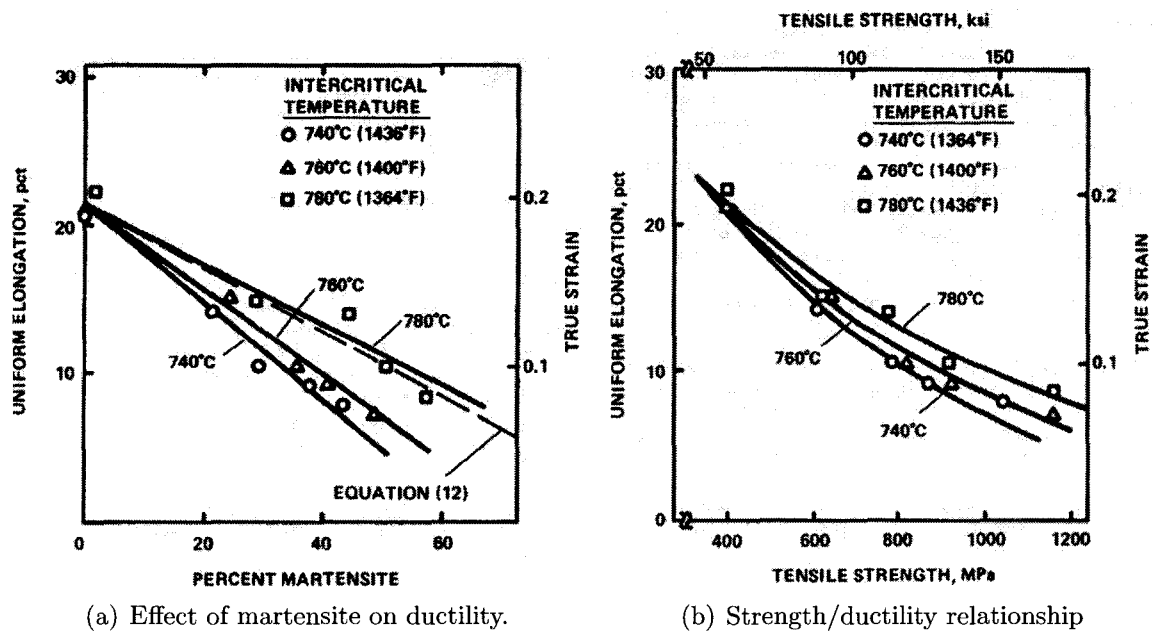


Figure 2.4: Composition/processing/property relationship for Fe-xC-1.5Mn steels (Speich and Miller 1979)

Effect of Increasing Mn Content on Structure and Properties

In terms of alloying additions, Mn plays a significant role in DP steels as an γ -stabilizer and solid-solution strengthener. An ideal DP steel requires a ductile, ferritic matrix with finely dispersed α_M . To achieve the most ductility in α , a minimal amount of alloying (especially interstitial species like C) is required. To aid in the

transformation of γ to α_M , an increased C content in γ is also needed. Therefore, the requirements for an alloying addition, as stated by Tanaka et al. (1979) are:

- It should not act as a solid-solution strengthener in α .
- It should retard the formation of bainite, delaying its formation and therefore aiding in the formation of α_M .
- It should be a γ -stabilizer – thereby promoting partitioning of C to γ , further stabilizing γ and aiding in the formation of α_M .

By possessing the last two properties, slower cooling rates can be used; increasing the amount of C which can diffuse from α into γ , continuing to stabilize it. Mn fits these criteria, as well as being a solid-solution strengthener in γ (Tanaka et al. 1979). Ghosh and Olson (1994) demonstrated that by modelling the driving force for the formation of α_M in the following way (equation 2.1), the impact of each alloy addition can be evaluated:

$$-|\Delta G_{M_s}^{\gamma \rightarrow \alpha_M}| [\text{J.mol}^{-1}] = 1010 - \sum_i a_i x_i^{0.5} \quad (2.1)$$

where x_i is the concentration of element i in the steel (in wt.%), and a_i is the weighted coefficient associated with the addition of element i . These coefficients are found in table 2.2 and it is evident that except for C and N (both interstitial solutes), Mn has the largest effect on the $\gamma \rightarrow \alpha_M$ transformation.

Consequently, a lower critical cooling rate is required to produce a phase portrait which would require higher cooling rates in a more dilute alloy as summarized in figure 2.5. This figure also shows the significant impact of Mn on the M_s temperature. Similarly, for a given cooling rate, an increase in Mn content will cause an

Table 2.2: Coefficients for equation 2.1 from Ghosh and Olson (1994) showing compositional effects on α_M formation.

i	a_i
C	4009
N	3097
Mn	1980
Si	1879
Cr	1868
Nb	1653
V	1618
Mo	1418
Cu	752
W	714
Ni	172
Co	-352

increase in hardness (figure 2.6). As with C, Mn is more soluble in γ than α and therefore partitioning is observed during intercritical annealing (Sun and Pugh 2000) – increasing the hardenability of the austenite which forms. Electron microprobe analysis by Speich and Miller (1979) of several DP steels determined that α_M found after intercritical annealing was enriched with Mn when compared to the surrounding regions - which can be owed to the partition of Mn to γ during intercritical annealing and the increase in hardenability it caused.

2.3 Continuous Hot-Dip Galvanizing

The ultimate goal of galvanizing is to deposit a layer of Zn on the steel surface to give both barrier and galvanic protection against corrosion. A continuous hot-dip galvanizing line (CGL) is shown schematically in figure 2.7. Following a strip as it enters the CGL, and using the labels in figure 2.7, there are several steps leading up to and following the galvanizing reaction (Marder 2000). First, there is a cleaning stage (1) to remove oils and other debris from upstream processing using an alkali solution

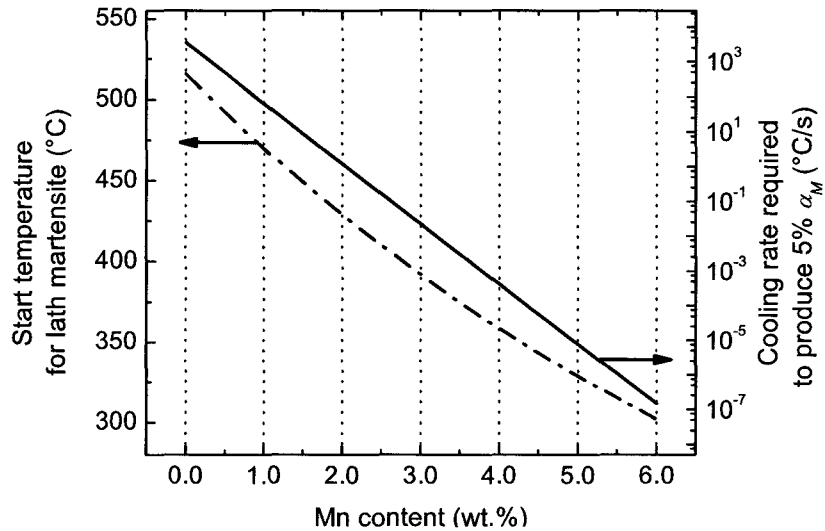


Figure 2.5: Martensite start temperature calculated from Zhao (1992), and cooling rate required to form 5% α_M calculated from expressions in Oren and Goodwin (2004) as a function of Mn content

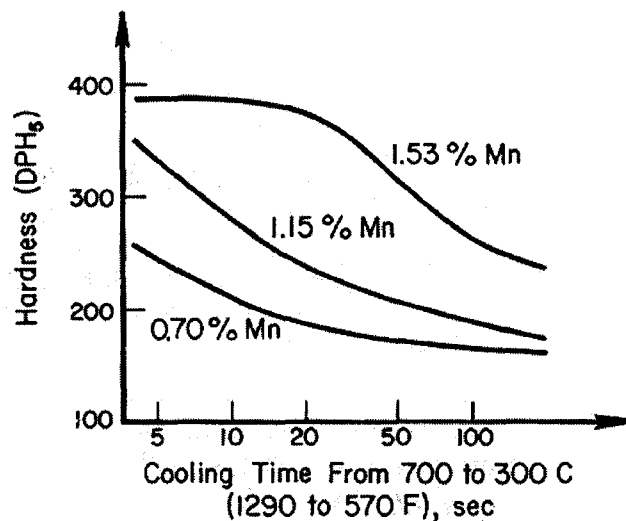


Figure 2.6: Hardness values from Bernard (1977) at various cooling rates for low-carbon steels with varying amounts of Mn.

and brushes. This is followed by a rinse in an electrolytic water system to remove strongly bound contaminants and finally drying with high velocity, low-pressure air to remove moisture. Subsequently, the strip passes through a radiant-tube, controlled-atmosphere annealing furnace (2) to recrystallize the cold-worked material and reduce Fe-oxides using an H_2 -containing atmosphere. Typically, the furnace is operated to produce an intercritical microstructure (see §2.2). Rapid cooling (3) cools the material from the annealing temperature and transforms the microstructure to the final phase portrait allowing control of the mechanical properties. The strip is then passed through a Zn bath (4), which typically contains 0.14–0.20wt% dissolved Al and is Fe-saturated, to form the galvanized coating on the surface. The coated sheet is then wiped with gas (typically air) knives (5) to remove excess liquid and achieve the desired coating thickness. At this stage, the product is cooled, any desired surface treatments applied and coiled after exit from the galvanizing line.

Two steps in the process are examined in greater detail in the following text: controlled atmosphere annealing and dipping in the molten Zn-Al-Fe bath.

2.3.1 Control of Oxidation Potential During Annealing

If an intercritically annealed steel is to be subsequently galvanized, the heat treatment has the requirement of controlling, or at least limiting, the amount of oxidation on the surface. This is done by controlling oxidation potential.

The oxidation potential controls which oxides are stable (i.e. which species are oxidized or reduced), along with their growth kinetics and morphology. During annealing, it is controlled as a means to reduce surface Fe-oxides to Fe^0 , resulting in a surface which can be reactively wet by the liquid Zn-Al-Fe alloy. The atmosphere is typically composed of a nitrogen (N_2) + hydrogen (H_2) mixture with a controlled

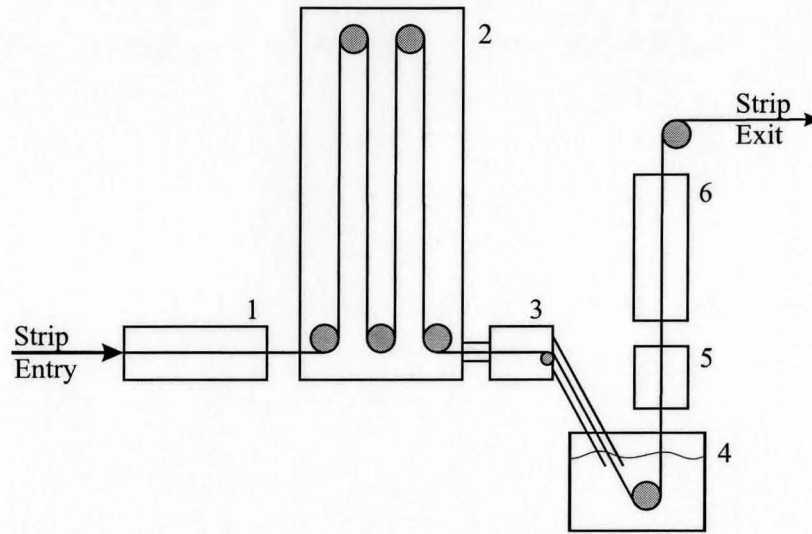


Figure 2.7: Schematic diagram of a continuous galvanizing line (CGL) including: 1) cleaning stage, 2) radiant tube furnace with controlled atmosphere, 3) cooling section, 4) molten Zn-Al-Fe bath, 5) gas wiping and 6) final cooling to coiler.

partial pressure of water ($p_{\text{H}_2\text{O}}$). With knowledge of the $\text{H}_2/\text{O}_2/\text{H}_2\text{O}$ equilibrium as seen in equation 2.2, the partial pressure of oxygen can be determined and fixed if the partial pressures of hydrogen and water are known and fixed.



In order to determine the partial pressure of oxygen, the value of the standard Gibbs energy of reaction 2.2 ($\Delta G_{\text{water}}^\circ$) needs to be known, and is defined in equation 2.3.

$$\Delta G_{\text{water}}^\circ = -RT \ln \left[\frac{a_{\text{H}_2\text{O}}}{a_{\text{H}_2} (a_{\text{O}_2})^{0.5}} \right] \quad (2.3)$$

where a_x is the activity of specie x relative to its standard state, R is the universal gas constant and T is the temperature in Kelvin. Assuming that the gases behave ideally (reasonable under high temperature, low pressure conditions as experienced during annealing), activities may be replaced with partial pressures resulting in equation 2.4.

$$\Delta G_{\text{water}}^{\circ} = -RT \ln \left[\frac{p_{\text{H}_2\text{O}}}{p_{\text{H}_2} (p_{\text{O}_2})^{0.5}} \right] \quad (2.4)$$

Since the amount of hydrogen is fixed by the composition of the $\text{N}_2 + \text{H}_2$ mixture, the partial pressure of water becomes the determining factor in the oxidation potential. Industrially, the amount of water in the annealing atmosphere is referred to in terms of the temperature at which the water vapour condenses - or the *dew point*. The relationship between dew point and water content is shown in figure 2.8.

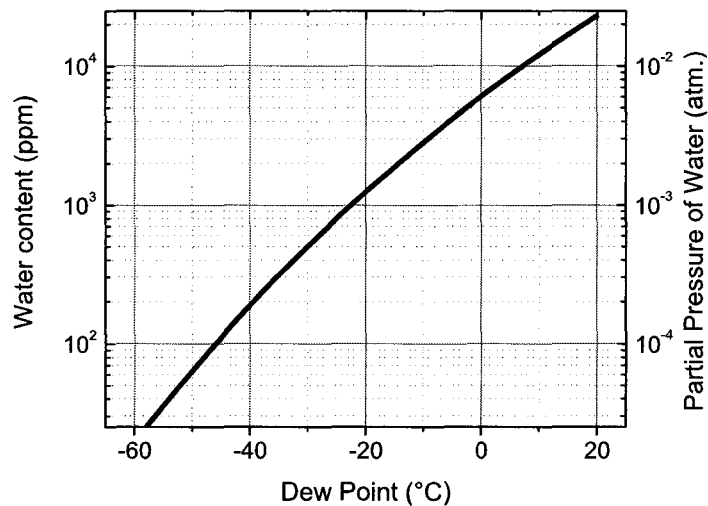


Figure 2.8: Relationship between water content and dew point as calculated with Thermo-Calc® and the SGTE pure substance database v.3.

If we write a general formula for the reduction of a stoichiometric oxide, M_xO_y , to its metallic state by a H_2 -containing atmosphere it would be as follows (Oleford et al. 1980):



As shown earlier with the $\text{H}_2/\text{O}_2/\text{H}_2\text{O}$ equilibrium, writing the standard Gibbs free energy for reaction 2.5 assuming ideal gases yields the ratio of $\text{H}_2\text{O} : \text{H}_2$ which can be subsequently used to determine the oxidation potential using equation 2.4.

$$\Delta G_{reduction}^{\circ} = -RT \ln \left[\frac{p_{\text{H}_2\text{O}}(a_{\text{M}})^{x/y}}{p_{\text{H}_2}(a_{\text{M}_x\text{O}_y})^{1/y}} \right] \quad (2.6)$$

Taking the activity of the oxide as unity ($a_{\text{M}_x\text{O}_y}=1$; stoichiometric oxide), the critical oxidation potential above which the oxide is stable and below which the oxide is reduced can be calculated assuming the activity of the specie being oxidized/reduced in the alloy (a_{M}) is known. This calculation was carried out with a readily available database of thermodynamic parameters (SGTE pure substance database v.3), and is shown in figure 2.9 for a variety of dew points and annealing temperatures. Included is the transition from pure Fe ($a_{\text{Fe}}=1$) to ferrous oxide (FeO; Wüstite), which is the lowest oxidation state of iron above the metallic state. This exemplifies the need for a controlled atmosphere during annealing.

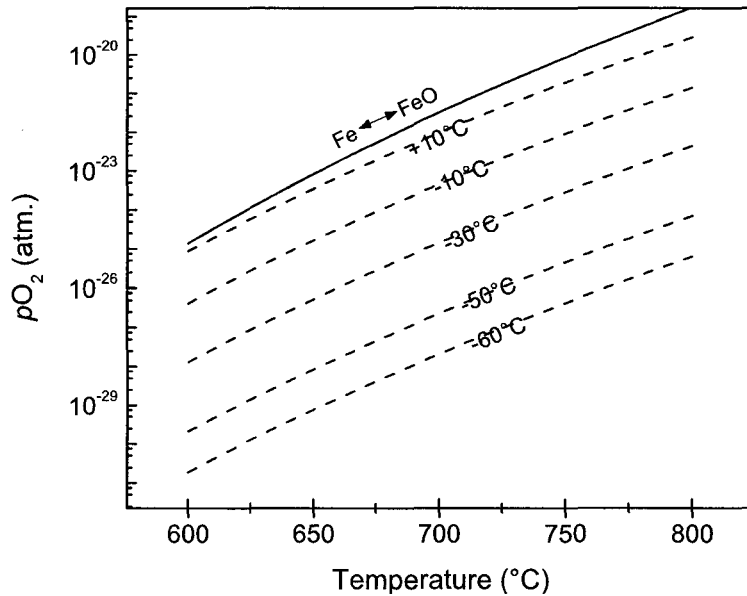


Figure 2.9: Effect of dew point and temperature on the oxidation potential of a $\text{N}_2/5\% \text{H}_2$ atmosphere with the Fe-FeO transition shown (calculated with Thermo-Calc® and the SGTE v.3 pure substance database).

Effect of Increasing Mn Content on Oxidation During Annealing

The treatment in the previous section deals only with the oxidation/reduction of Fe_xO_y . When the Mn/MnO transition is added to figure 2.9 using equation 2.6 with multiple values of a_{Mn} , the result is significantly different. Figure 2.10 demonstrates why it has been observed by many authors that Mn is selectively oxidized to MnO during annealing (Cvijovic et al. 2006, Oleford et al. 1980, Huin et al. 2004). Herein lies a major drawback with advanced high strength steels (AHSS): the typical heat treatment and process atmospheres used to produce a metallic Fe surface for galvanizing are oxidizing with respect to Mn, resulting in a layer of MnO on Mn-containing steels (Oleford et al. 1980).

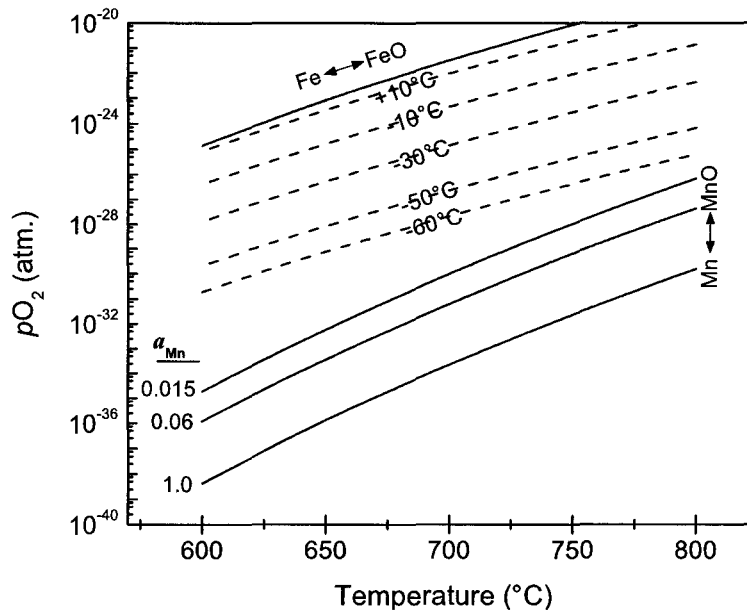


Figure 2.10: Demonstration of the relationship between process gas composition and the oxidation of Mn during annealing for a $\text{N}_2/5\%\text{H}_2$ atmosphere (calculated with ThermoCalc® and the SGTE v.3 pure substance database.)

Moreover, to increase their strength and hardenability, it is desirable to increase the amounts of Mn, Si and/or Al in AHSS – all of which have a high affinity for oxygen and whose oxides have a large negative enthalpy of formation (Bode et al. 2004)

making them prone to form during annealing. Work by Oleford et al. (1980) has shown that increasing the amount of these strengthening/oxidation prone elements causes an increase in the proportion of the surface covered by oxides; even at small additions. This is shown in figure 2.11, and extrapolated to compositions that are considered *low-alloy* by today's standards. From this explanation, and referring to table 2.1, it can be seen that a typical DP steel will have a very high fraction of its surface covered with oxides.

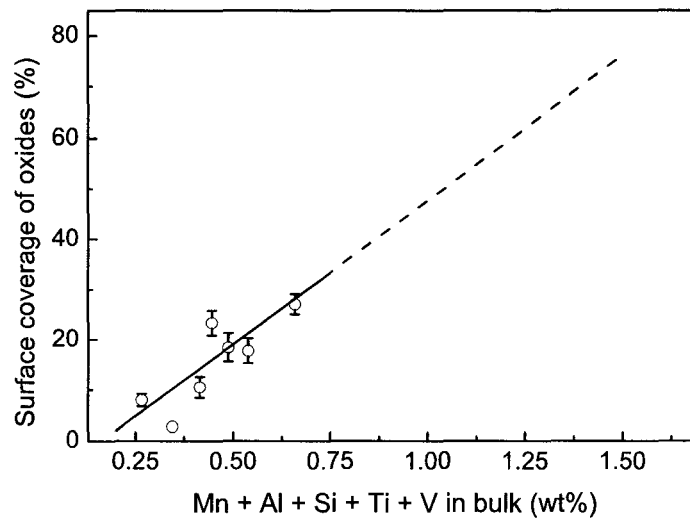


Figure 2.11: Amount of external steel surface covered with oxides after annealing as a function of bulk alloy content adapted from Oleford et al. (1980). The dotted line represents an extrapolation of the observed trend towards higher alloy (higher strength) steels.

2.3.2 Reaction Products Formed upon Dipping

Unlike the process of physical wetting which depends only on capillary forces, galvanizing is a reactive wetting processing owing to the formation of reaction products at the steel/coating interface. A typical galvanizing bath is operated at 450–470°C and commonly contains approximately 0.14–0.20wt% dissolved Al and is Fe saturated (Marder 2000). The addition of Al aids the process in several ways, most of which

arise from the change in equilibrium of a Fe-saturated bath from ($L + [\zeta$ and/or $\delta]$) to ($L + \text{Fe}_2\text{Al}_5$) as shown in figure 2.12.

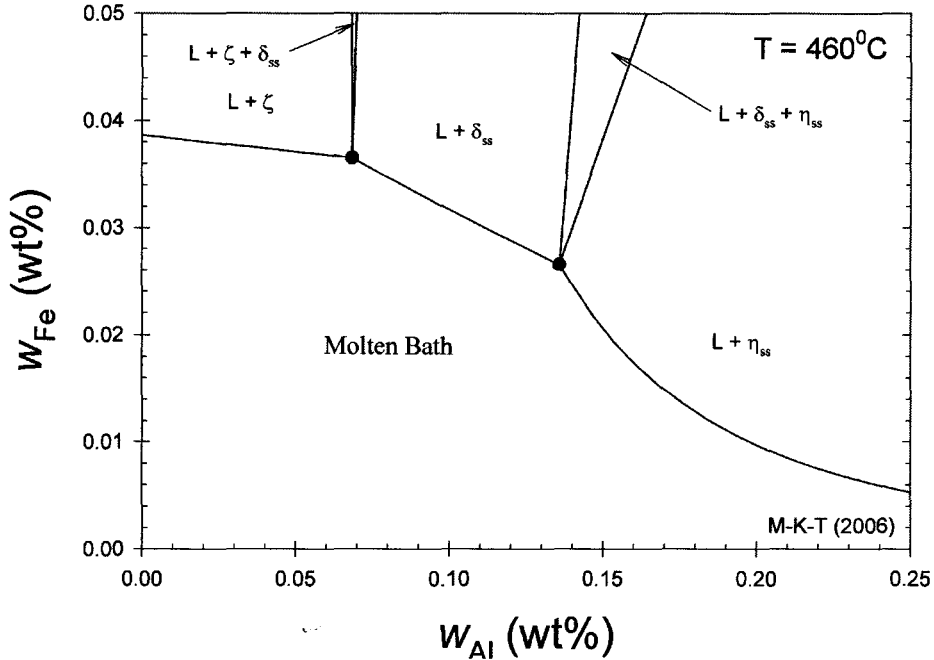


Figure 2.12: Zn-rich portion of the metastable (Γ suppressed) Zn-Al-Fe phase diagram at 460°C where η_{ss} refers to $\text{Fe}_2\text{Al}_5\text{Zn}_x$ and δ_{ss} refers to $\text{FeZn}_{10}\text{Al}_y$. From McDermid et al. 2007.

At very low levels (i.e. $0.005\text{wt}\%$ to $0.02\text{wt}\%$), Al is used to brighten the coating with the formation of a thin Al_2O_3 layer on the external surface (Marder 1989). This mechanism, along with decreasing the partial pressure of Zn, play an important role in decreasing the evaporative losses of the bath. Most importantly, by adding more than $\sim 0.1\text{wt}\%$ Al, the compound with the smallest nucleation barrier becomes Fe_2Al_5 and it precipitates on the steel surface rather than the more brittle series of Fe-Zn compounds (Guttman 1994). This thin ($\sim 250\text{nm}$) layer can be observed as an Al rich region between the steel substrate and Zn coating (figure 2.13).

The formation of this Al-rich layer is a metric for success in the galvanizing industry because its presence as a continuous layer of Fe_2Al_5 crystals inhibits the formation

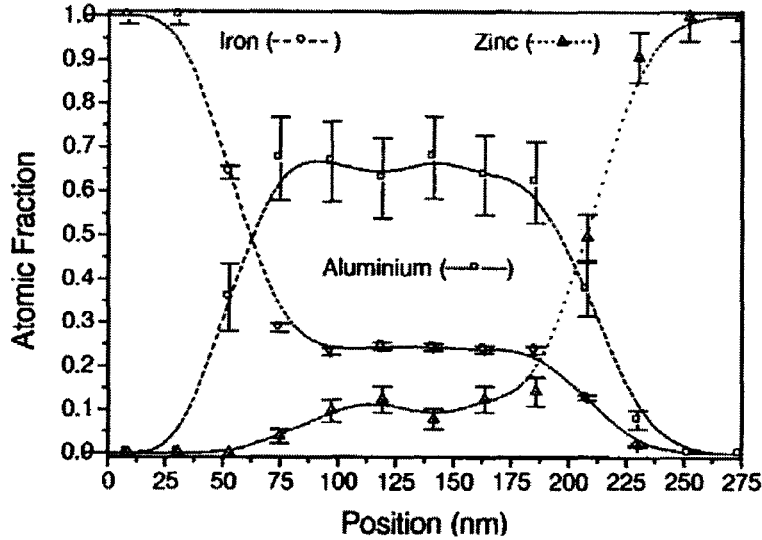


Figure 2.13: Composition profile for Al, Zn, and Fe through the steel/coating interface showing Al-rich layer formed after dipping in 0.18wt% Al bath (Baril and L'Esperance 1999).

of more brittle Fe-Zn intermetallic compounds, and it is commonly referred to as the inhibition layer (Marder 1989). However, the appearance/formation of this layer is only a transient state, and after prolonged exposure to the liquid bath the inhibition layer will break down. To understand this behaviour, it should be noted that although the liquid is in equilibrium with Fe_2Al_5 when the liquid contains more than $\sim 0.14\text{wt}\%$ Al and is Fe-saturated, the equilibrium between the substrate and the bath is not the same as the equilibrium that drives the system towards its final phase portrait for longer immersion times (Guttman et al. 1995). In this case, only $\Gamma\text{-Fe}_3\text{Zn}_{10}$ is stable with respect to $\alpha\text{-Fe}$, and the reactions are driven towards this as seen by observation of this phase on submerged hardware (Guttman 1994). The kinetics of this so-called inhibition breakdown are mitigated by the competition between inhibition layer growth and intergranular diffusion of Zn to the steel surface. As the growth rate of the Fe_2Al_5 decreases (approximately \sqrt{t}), intergranular diffusion of Zn becomes dominant and when a critical concentration of Zn at the steel surface is reached, $\zeta\text{-FeZn}_{13}$ becomes favoured for nucleation. This compound grows outward from the steel/coating interface at a rate exceeding that of the inhibition layer and it

physically displaces it in the process (Guttman 1994). Most commonly ζ -FeZn₁₃ will form so-called outbursts due its rapid growth rate. Their formation is detrimental to coating quality as the outbursts can be visible from the external coating surface. An example of an outburst is show in figure 2.14.

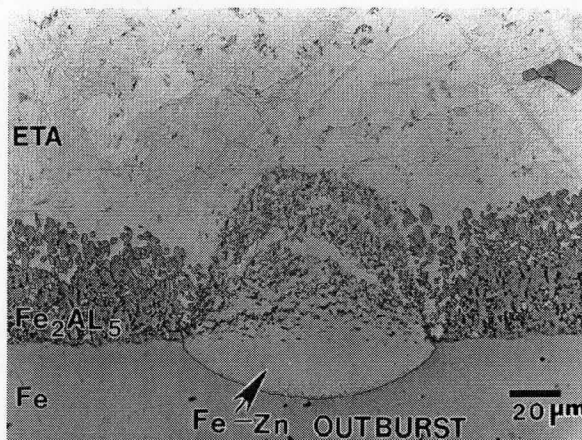


Figure 2.14: Formation of Fe-Zn IMC after prolonged (3600s) exposure to a 0.20wt% dissolved Al bath at 450°C. From Jordan et al. (1997)

Because it is only the dissolved Al which can react with the steel, this is the quantity which is of greatest importance. This value is commonly quoted in lieu of the bulk Al content and is often referred to as the *effective* Al in industry-specific literature.

2.3.3 Effect of Surface Species on Reactive Wetting

Under ideal conditions, reactive wetting during galvanizing would be performed on a surface comprising only metallic Fe. It is well established that oxide species on the surface of the steel can delay or prevent the reactive wetting process (Bode et al. 2004, Oleford et al. 1980). This was shown explicitly by the observations of Drillet et al. (2004) when an un-wettable surface was created when only a relatively small portion of the surface was covered with Mn and Si-bearing oxides (figure 2.15). Similarly,

Frenznick et al. (2004) used a modified spin-coating technique with a galvanizing bath alloy to show a significantly decreased reactivity with higher alloy steels. Specifically, it was shown that steels with Mn, Si and Al-oxides on the surface exhibited a greatly reduced rate of decrease of the contact angle (between the liquid/gas and liquid/solid interfaces) – indicating decreased wettability and reactive wetting kinetics.

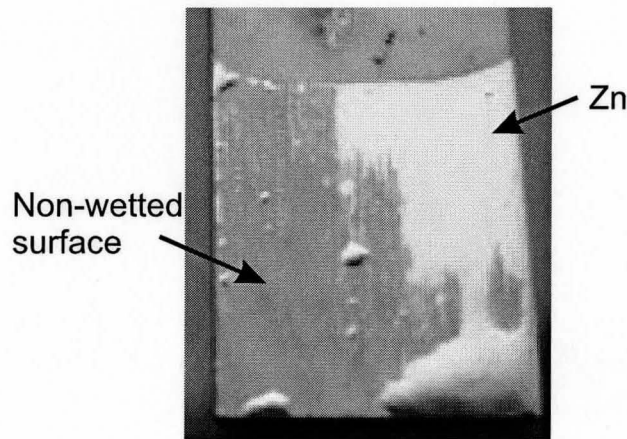


Figure 2.15: Example of an un-wettable surface created with an experimental high Mn-Al steel. From Drillet et al. 2004.

Observations like these are difficult since the oxide layer is thin (typically on the order of 100-200nm) and the results from these experiments are typically limited to qualitative observations of the surface after simulating hot-dip galvanizing (i.e. figure 2.15). This can result in binary and subjective conclusions as to the effect of alloying additions and processing atmospheres on reactive wetting. Comparing results between studies is also often difficult given that conditions such as bath stirring, heating rate, isothermal soak time and cooling rate during annealing vary significantly and have an impact on the amount of oxidation and subsequent wettability. Thus, there is little quantitative data pertaining to the increase or decrease in wettability as a function of alloy content or annealing parameters which can be universally applied since each author makes his/her own conclusions based on different measures.

One item over which there is little controversy is that a film of MnO is formed on Mn-containing steels using any reasonable annealing atmosphere and temperature, resulting in decreased wetting. Although this film doesn't necessarily *prevent* reactive wetting since Mn-containing steels are currently galvanized, a kinetic limitation prevents the addition of large amounts of Mn due to the increased amount of oxidation. From this, a limitation is placed upon the amount of Mn which can be added to steels if they are to be subsequently hot-dip galvanized. This was outlined by Oren and Goodwin (2004) as one of the main issues preventing high-Mn and Si steels from being galvanized. However, placing an exact value on this limitation is difficult when quantitative measures of wettability and reactive wetting kinetics in these systems do not exist.

2.3.4 Aluminothermic Reduction of MnO

Quantification of the reactive wetting process in galvanizing, as outlined in an upcoming section, is generally limited to measuring the composition, size and morphology of the Fe-Al interfacial layer formed upon dipping. This type of examination is, therefore, limited to the process of intermetallic compound formation and not the critical first step involving the removal of the oxide to expose a metallic surface for further reaction.

As seen in figure 2.16, after galvanizing a Mn containing dual-phase steel, there is no oxygen remaining at the steel/zinc interface and the Al-rich interfacial layer has been formed. The work of Khondker et al. (2007) has shown implicitly on a laboratory scale that it is possible to reduce MnO with the dissolved Al in the bath via the reaction:



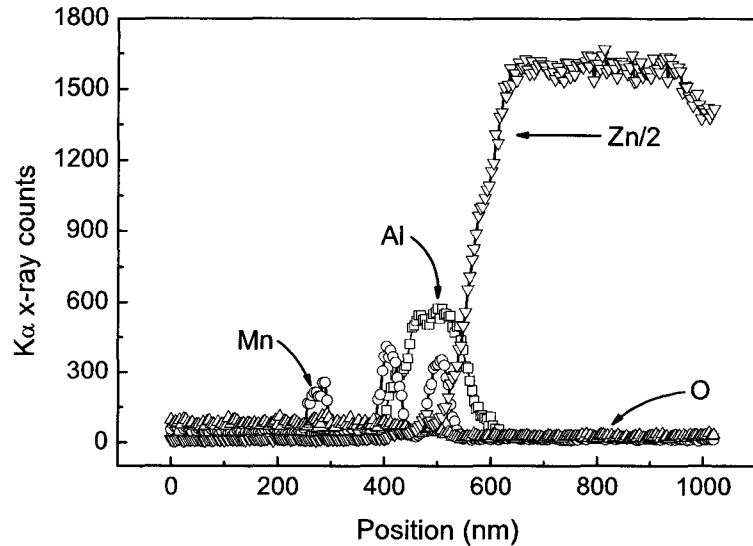


Figure 2.16: TEM-based EDX line scan of zinc/steel interface for a DP-600 (1.97wt% Mn) steel processed at a dew point of +5°C and dipped in a 0.20wt% Al bath showing the presence of an Al-rich interfacial layer and lack of oxides. From Khondker et al. (2007).

Thermodynamically, the process of aluminothermic reduction (equation 2.7) is favoured if $a_{\text{Al}} \gtrsim 10^{-16}$ in the bath. This is much lower than a_{Al} calculated (Nakano et al. 2007) for a typical 0.2wt% dissolved Al, Fe-saturated galvanizing bath ($\sim 10^{-4}$), and much less than is required to form the inhibition layer (Guttman 1994; Tang 1989).

The simplest way to prove this mechanism is to measure the accumulation of Mn in the bath. On an industrial scale this is difficult because the oxide is fairly thin ($\sim 100\text{nm}$), and the bath is quite large (hundreds of tonnes) - resulting in almost undetectable changes in dissolved Mn. Fortunately, Dubois (1998) conducted such measurements in an investigation where it was shown that there were increased levels of dissolved Mn in the bath after galvanizing many coils of Mn-containing steel. This offers empirical support for the mechanisms in equation 2.7. Unfortunately, neither the mechanism nor published experimental results aid in determining the kinetics of the process or the thickness of MnO which can be successfully reduced in the short period when the steel is immersed in the bath.

2.3.5 Increasing the Wettability of High-Mn Steels

To increase the wettability or increase the reactive wetting kinetics in systems prone to oxidation, several processing routes have been explored, all involving changing the surface prior to dipping. The idea behind this is that any technique which increases the amount of Fe^0 on the surface will increase the wettability.

One such investigation involved using reactive CO and NH_3 - containing atmospheres during annealing (Bleck and Beste 2004). The former atmosphere was used to carburize the steel prior to dipping and, therefore, limit the amount of oxides present at the surface before dipping and the latter was used with the intention of nitriding the surface for the same reason. It was shown that the process atmospheres with the highest a_C and NH_3 content limited the amount of external oxidation and increased the wettability of the steel. Although promising, applying this to an industrial galvanizing line would be expensive and, in the case of NH_3 , raises safety issues. Moreover, the control sample in this study, which was annealed with 10% H_2 and a dew point of -28°C , showed a number of bare spots which would not be typically found for a 1.5wt% Mn alloy. This was most likely caused by either a leak in the experimental apparatus, increasing the $p\text{O}_2$ during annealing, or improper measurement/control of the dew point. Consequently, the reliability of this work is questionable.

Another method involving the use of a high $p\text{O}_2$ annealing atmosphere by increasing the dew point in a typical $\text{N}_2/5\%\text{H}_2$ gas mixture has been proposed by Oren and Goodwin (2004). It was thought that this will increase wettability because: a) increasing the $p\text{O}_2$ sufficiently will result in internal oxidation, and b) internally oxidizing elements will result in an increased Fe^0 concentration at the surface. The effect of $p\text{O}_2$ on both internal oxidation and Fe^0 at the surface was studied by Vanden Eynde et al. (2002) and the results summarized in figures 2.17 and 2.18. This resulted in varying depths of oxidation and Fe^0 at the surface (figure 2.18), but

there haven't been conclusive results on the change in wettability from this modified atmosphere.

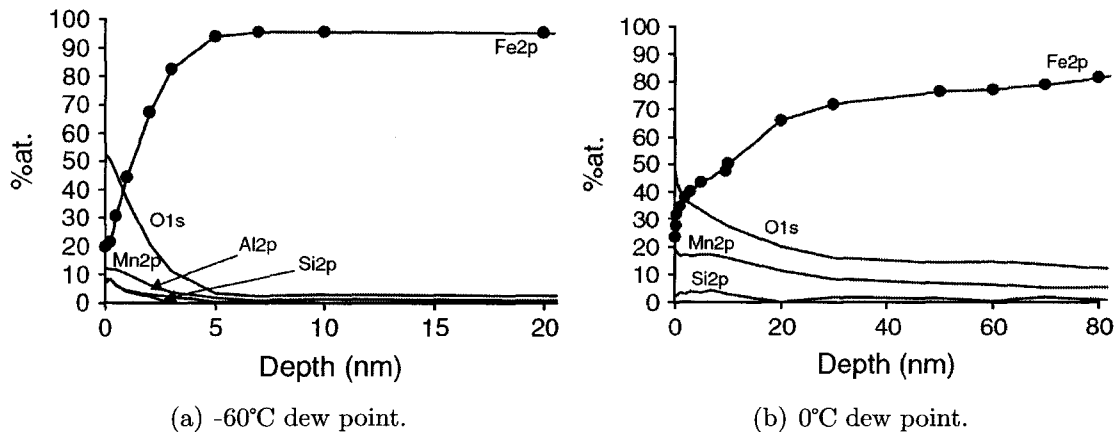


Figure 2.17: XPS Depth profiles from Vanden Eynde et al. (2003) for a dual-phase steel annealed in a $N_2/5\%H_2$ atmosphere with given dew point. Note the change in horizontal scaling.

Following this concept, Khondker et al. (2007) annealed a 1.97wt% Mn DP steel using atmospheres with various pO_2 and showed that oxide thickness was a function of the process atmosphere pO_2 and that with an adequately high pO_2 , internal oxidation of MnO was possible. Despite the large range of pO_2 explored, and various thicknesses of oxide films formed, the alloy exhibited excellent reactive wetting with the formation of a continuous layer of Fe_2Al_5 crystals. This means that with this composition and range of pO_2 , the threshold of wettability had not been crossed.

Further work on changing the nature of Mn oxidation by (Shi 2004) involved pre-oxidation of the substrate. Reference is made to the term ‘galvanizing’ numerous times in this work, but a GALVALUME[†] bath (Zn/55wt%Al) was used. Using a muffle furnace at $\sim 500^\circ C$, a high-carbon steel with 1.93wt.% Mn was oxidized in air with the

[†]GALVALUME is a trademark of BIEC International Inc., Vancouver, WA.

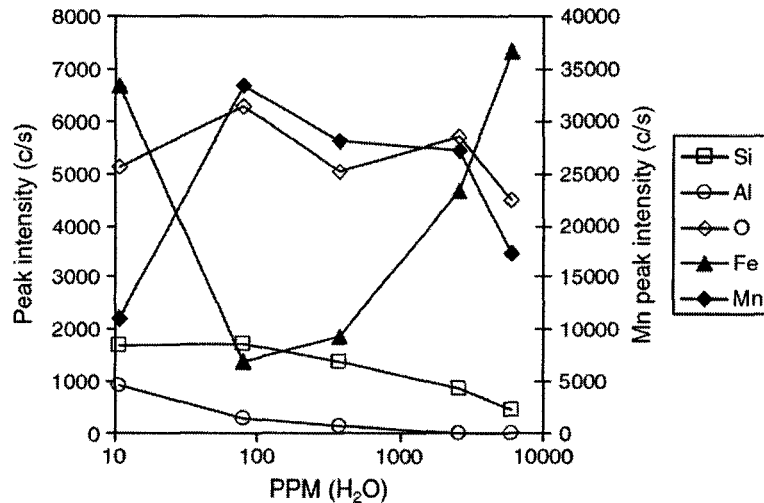


Figure 2.18: Evolved surface compositions after annealing a dual-phase steel as a function of dew point (Vanden Eynde et al. 2003)

objective of producing FeO_x on the surface prior to intercritical annealing. By doing this, it would require more time to reduce the oxide during intercritical annealing, leaving a shorter period of time remaining for Mn to be oxidized. The resulting surface structure was indistinguishable from one produced by intercritical annealing alone, likely due to the rapid nature of both FeO_x reduction and Mn oxidation.

2.4 Quantification of Wetting Processes

2.4.1 Motivation

Most commonly, the term wetting is found in electronics manufacturing, referring specifically to solder joints. In these systems extensive literature can be found in journals such as: Soldering & Surface Mount Technology, Journal of Microelectronics & Electronic Packaging, Journal of Electronic Materials, and Circuits Assembly referring to the wettability of specific substrate/solder systems.

Understanding the wetting kinetics in galvanizing are crucial to determining parameters such as immersion time. If the steel is not in the bath long enough, the inhibition layer will not be fully formed; immersion for too long will result in a breakdown of the inhibition layer as discussed in §2.3.2. Furthermore, in contrast to studying soldering in electronic components, galvanizing is rapid (~ 3 seconds), requires a controlled atmosphere and refers not only to physical wetting but reactive wetting with the formation of interfacial compounds. For these reasons, wettability measurements are typically limited to measuring the alloy content and size of the interfacial layer over time (Jordan et al. 1997; Borzillo and Hahn 1969; Baril and L'Esperance 1999) as shown in figure 2.19.

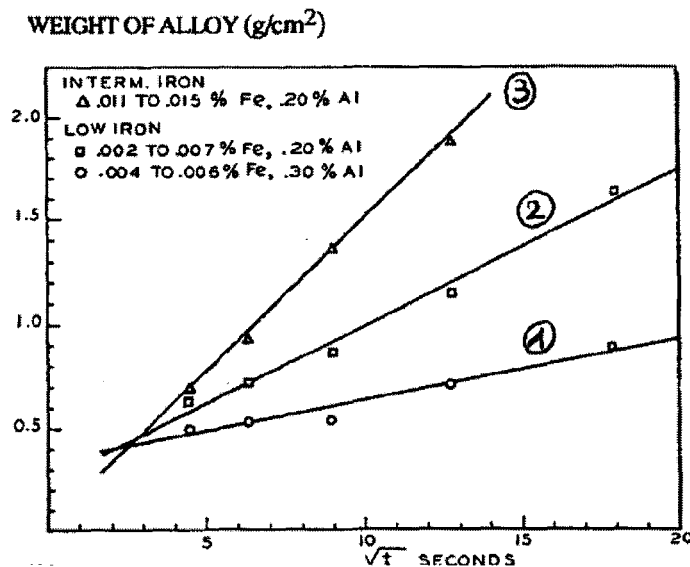


Figure 2.19: Interfacial alloy layer growth over time for various bath compositions. From Borzillo and Hahn (1969).

This technique applies well to alloys which already exhibit excellent wetting - usually due to low alloy content resulting in minimal oxidation before exposure to the bath. When dealing with higher alloy steels, it has been seen that the surface becomes un-wettable (figure 2.15) and is, therefore, limited by the process of removing the oxide(s) formed during intercritical annealing. If bare spots can be seen with the

naked eye (i.e. $\gtrsim 0.1\text{mm}$), the critical threshold of wettability has already been exceeded.

2.4.2 Young's Equation and the Triple Line

Physical wetting processes are well described by Young's equation (Young 1805) which is valid for systems where the liquid and solid are mutually insoluble (e.g. oil on glass), where the solid can be assumed to be rigid and there are no reaction products formed. With the contact angle and orientation of interfacial tensions shown schematically in figure 2.20a), Young's equation is expressed as follows for a system in static equilibrium:

$$\sum F_y^{\text{triple line}} = P[\gamma_{\text{SV}} - \gamma_{\text{SL}} - \gamma_{\text{LV}}\cos\theta] = 0 \quad (2.8)$$

where γ_{ij} is the interfacial tension between phase i and j ($i, j = \text{solid, vapour or liquid}$), θ is the contact angle between the liquid and solid phases and P is the length of the three-phase boundary.

This boundary between solid, liquid and vapour phases (S, L and V respectively) is referred to as the triple junction, or triple *line* in the case where the liquid phase is not a spherical drop. This latter geometry is illustrated in figure 2.20, where the triple line is normal to the page.

When reactive wetting is considered, the situation is complicated by the formation of reaction products altering the interfacial energy terms and bringing into question whether changes in the wetting angle are due to capillary effects (represented by the contact angle expressed by Young's equation) or changes in the system due to compound formation (Adda, Ambroise, and Barbier 1994). Additional constraints

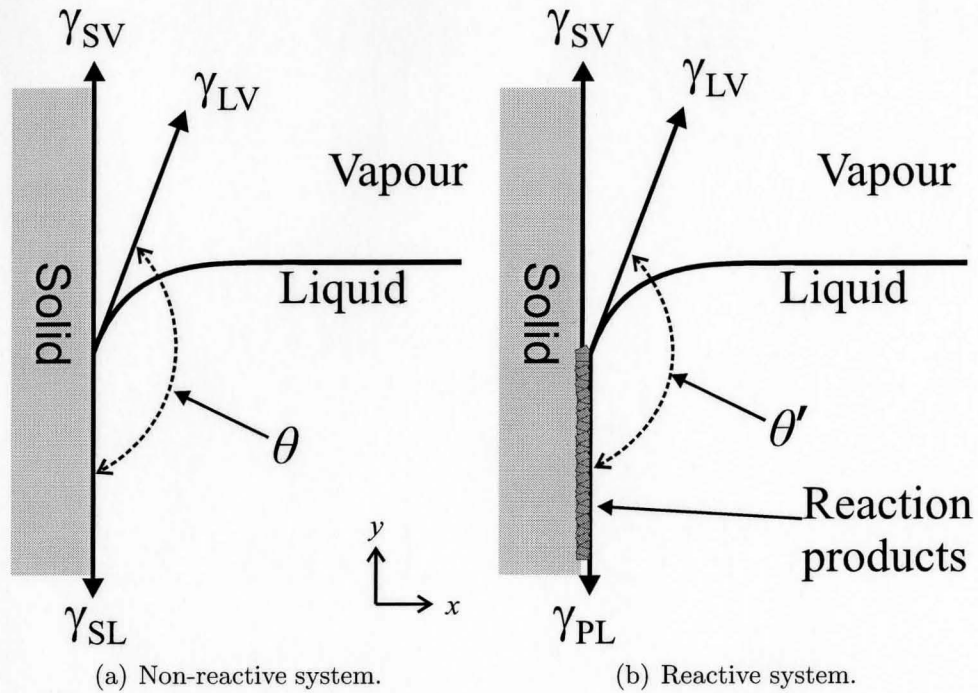


Figure 2.20: Schematic illustration of a submerged sample illustrating the contact angle and interfacial tensions acting on the solid for two different situations.

imposed by this situation are represented in figure 2.20b, where θ is modified to θ' and γ_{SL} has been replaced with γ_{PL} - representing the interfacial energy between the liquid and interfacial reaction products. Following this, it is unclear if the progression of galvanizing reactions is dominated by capillary forces or chemical reactions, and if it is possible to separate the physical and chemical contributions (Adda et al. 1994). The nature of Young's equation has led to arguments pertaining to its validity in reactive wetting systems. The unbalanced forces in the x -direction (figure 2.20), the effect of gravity (Garandet et al. 1998), as well as the effects in mass-transport limited systems (Adda et al. 1994) such as seen in galvanizing reactions have led to numerous discussions (Liu and German 1996; Marmur 1996) and few concrete conclusions. Moreover, since galvanizing reactions are transient in nature, a galvanized sample is considered to be at a state of metastable equilibrium (Guttman 1994) where equi-

librium is actually unfavourable as it leads to breakdown of the of the inhibition layer (see §2.3.2). This allows a certain freedom in calculations by permitting assumptions about the process, resulting in treatments which vary between authors. Furthermore, there is no agreement as to the measurement and meaning of the contact angle in reactive wetting. A reactive liquid drop in contact with a solid goes through several stages during reactive wetting, passing through metastable regimes with dissolution of and reaction with the substrate as shown in figure 2.21. Each of these stages results in different values of the contact angle with reference to the phases formed.

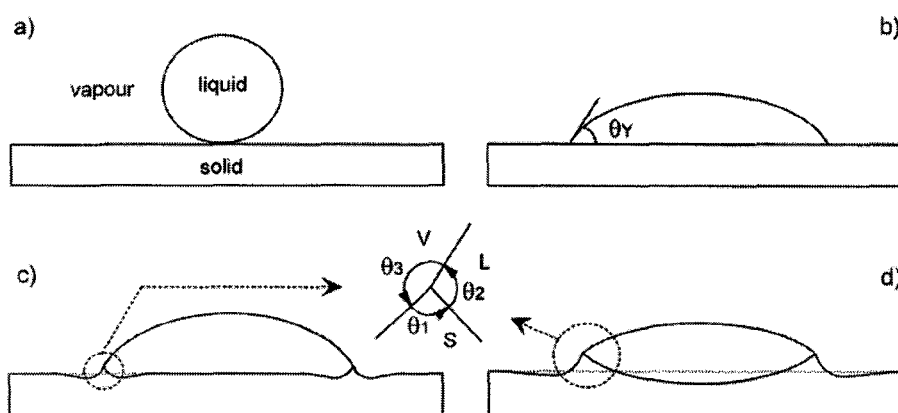


Figure 2.21: Progression of triple line configuration in reactive wetting from: a) initial contact \rightarrow b) metastable configuration \rightarrow c) stable configuration of triple line \rightarrow d) stable configuration of the whole system (Garandet, Drevet, and Eustathopoulos 1998).

Regardless of how the triple line and contact angle are treated in reactive systems, it is agreed upon that a decrease in contact angle is indicative of an increase in wetting (Aksay et al. 1974), thereby forming the basis for the evaluation of solid/liquid wettability. This has led to continued study of the contact angle in reactive systems, including galvanizing.

2.4.3 Current Methods Used to Measure Reactive Wetting

The mechanisms of inhibition layer formation are well established using techniques involving measurement of both the thickness and composition in systems which are not rate limited by the presence of oxides (i.e. Baril and L'Esperance 1999, reviewed in Guttman 1994 and Marder 2000). By comparison, there has been very little established with regards to kinetics for oxidation prone systems – specifically in quantitative terms. Measuring the thickness/composition of the interfacial layer in these systems is not feasible for several reasons:

1. A small sample is not necessarily representative of the bulk processes.
 - Observations of bare spots indicates reactive wetting occurring at different rates in different locations likely due to slightly varying oxide thicknesses/chemistry across the surface, resulting in Al depletion and decreased reaction rates.
2. By the time the inhibition layer has formed, the transition from non-wettable to wettable has been surpassed.
 - Ideally, the experiments should see this transition, or measure the formation of the inhibition layer when limited by surface oxidation.

One technique which has been explored is known as the sessile drop method . This method utilizes a controlled atmosphere furnace to anneal a horizontally-oriented substrate followed by a drop of the reactive bath alloy being placed on the substrate surface from a syringe. To measure wetting, a high speed camera is focused on the point where the liquid comes into contact with the solid. Figure 2.22 shows the measurement technique and figure 2.23 shows images captured in such experiments from Ebrill et al. 2000.

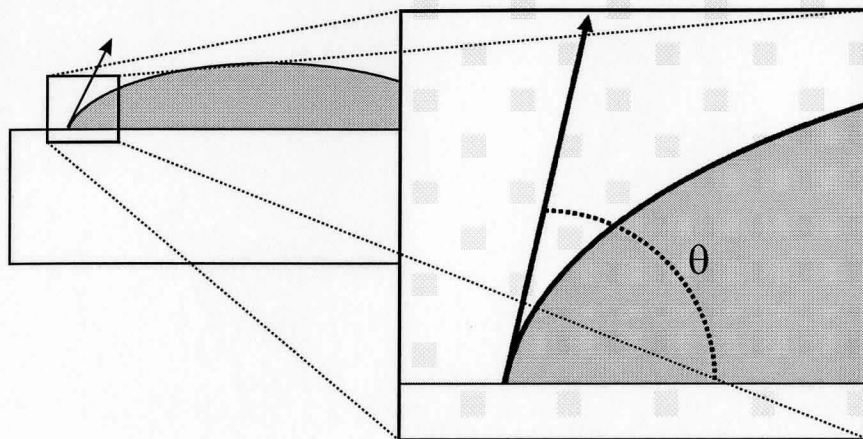


Figure 2.22: Schematic illustration of the contact angle (θ) measurement during a sessile drop experiment. The difference between observed contact angle in the inset and outset demonstrates the subjective nature of this method.

Several aspects of this type of experiment make it problematic for galvanizing experiments:

1. The rapid nature of wetting.

- In low-alloy steels, it requires measurements in the millisecond range. As shown in figure 2.24, the contact angle changes very rapidly, and it could be argued that after ~ 10 ms the reaction has reached a steady state – offering little insight into reactive wetting kinetics.
- Perturbations in the data remove the ability to identify the incubation period, or early time ($\lesssim 100$ ms) kinetics. Moreover, the noise seen in figure 2.24 is likely a function of the geometry of the system (drop size, distance from syringe to substrate) and not indicative of the reactions being explored.

2. The finite size of the drop limits solute available for the reaction.

- Work with higher alloy steels (limited by oxides on the surface) show negligible reaction rates (Frenznick et al. 2004), likely due to the increased

consumption of Al through aluminothermic reduction of the oxide on the surface and the finite size of the drop.

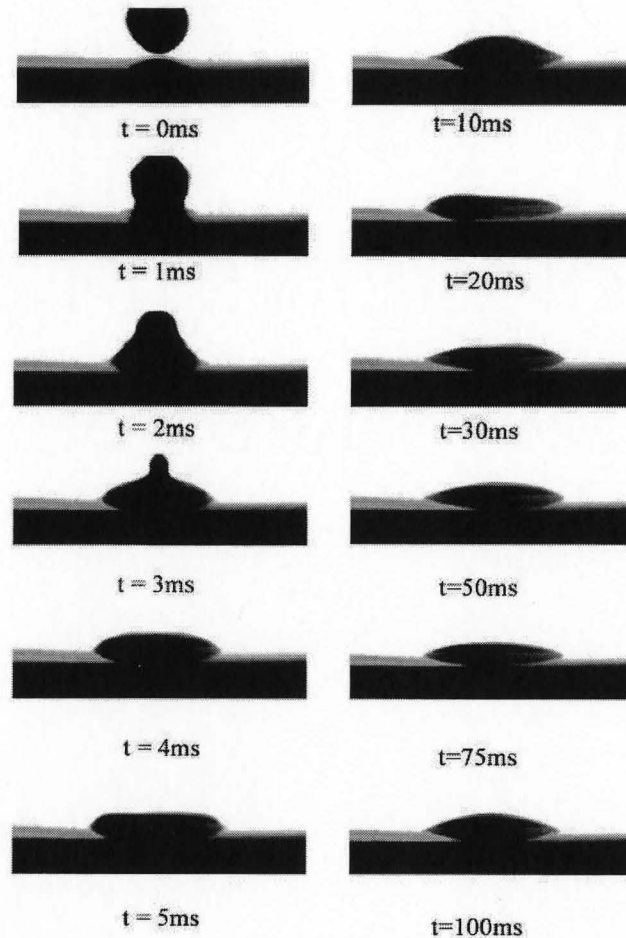


Figure 2.23: Progression of drope profiles in a Zn-Al wetting experiment utilizing the sessile drop technique. From Ebrill et al. (2000).

The resulting data from sessile drop experiments is either too rapid to give quantitative results or too slow to be representative of the nearly infinite Al supply in a CGL. These limitations have resulted in galvanizing experiments on higher alloy steels being limited to qualitative observations of the surface. One such set of experiments by Drillet et al. (2004) utilized several experimental high Mn, Si and Al steels. The resultant lack of wetting allowed a conclusion to be drawn that the

threshold of wettability had been exceeded. Whether it was significantly exceeded or by a small margin cannot be said. In an attempt to quantify a subjective measure, Bode et al. (2004) conducted galvanizing experiments with steels similar to the study of Drillet et al. (2004), and quantified their results based on the appearance of the galvanized surface. The results of this work, shown in figure 2.25 show a trend towards decreased wetting with increased Mn surface enrichment, and increased wetting as a function of Fe^0 surface content.

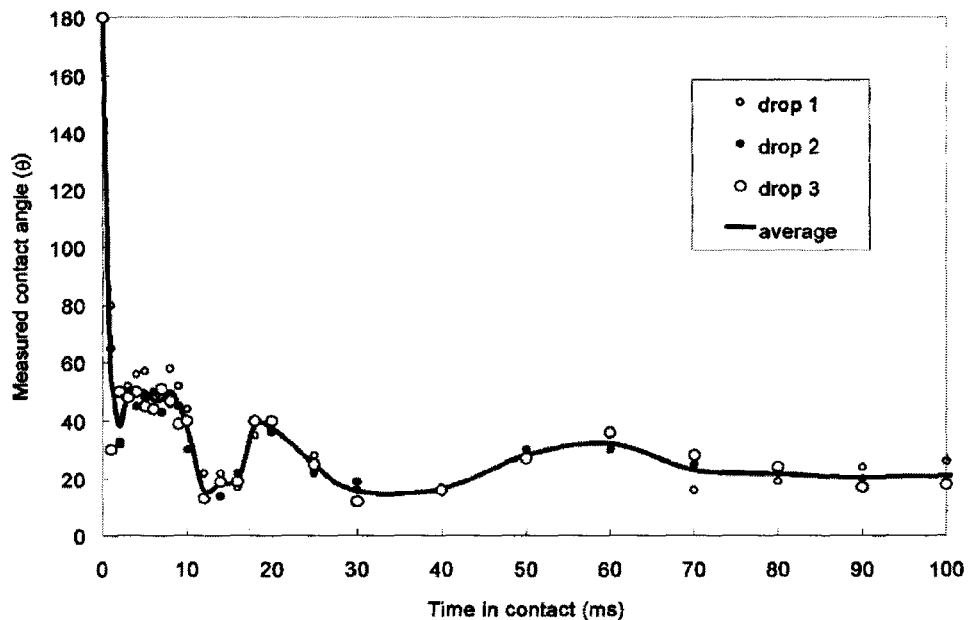


Figure 2.24: Progression of the contact angle in a Zn-Al wetting experiment utilizing the sessile drop technique. From Ebrill et al. (2000).

In soldering systems, wettability has been characterized with the use of a force balance in a manner consistent with that of Wang et al. (2006). There is minimal data of this type for galvanizing systems – limited to only three bodies of work. The earliest work was that of Renaux and Sylvestre (1989), where the metric of ‘ultimate wetting force’ measured at longer times ($\sim 20s$) was used, offering little in the way of kinetic measurements. Second, Hashimoto et al. (2003) used Mn and Si containing steels, and again measurements were quoted at 30s – well beyond the reaction time

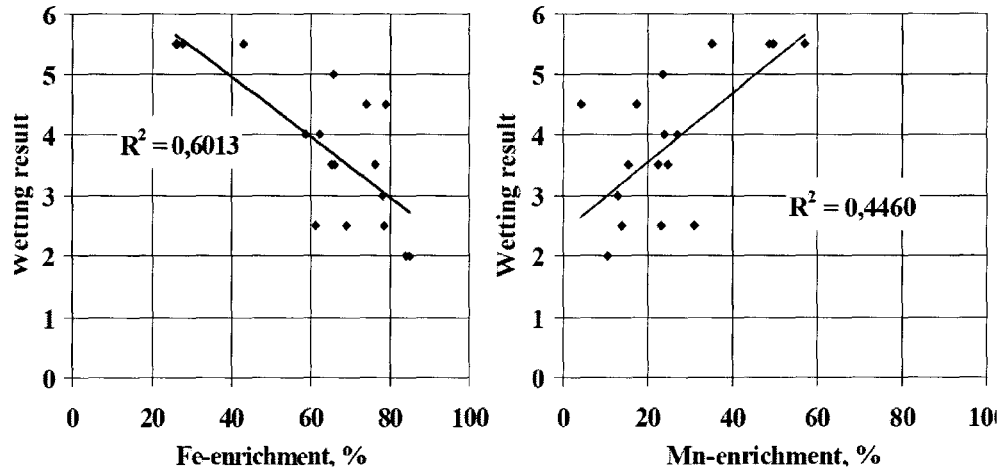


Figure 2.25: Qualitative quantification of coated sample appearances as a function of surface enrichment. A lower number representative more favourable wetting. From Bode et al. (2004).

in a continuous galvanizing line. Moreover, they used a pure Zn bath, negating the important effects of Al. Recently, Bode et al. 2004 introduced a modified version of this technique showing only a single figure and presenting no discussion of the results - but it did show decreased reactive wetting of a Mn-containing steel when compared to an interstitial free (IF) steel. This emphasizes the gap in data and understanding of galvanizing reactions limited by oxides on the annealed surface.

Chapter 3

Research Objectives

Since the reduction of tenacious oxides on the surface of AHSS produced during annealing may be the rate-limiting step during galvanizing (as shown with the appearance of bare spots), this may ultimately limit the compositions of alloys which can be successfully galvanized. Thus, the objectives of this thesis are:

1. Develop a method to quantitatively characterize reactive wetting kinetics.
 - Utilize a commercial force balance simulator (used for non-kinetic, quasi-equilibrium measurements) to determine the kinetics of reactive wetting.
2. Prove explicitly that Al in the bath reduces MnO on the surface of intercritically annealed steels during galvanizing.
3. Investigate the reactive wetting kinetics of high-Mn alloys in a galvanizing bath as a function of alloy Mn content and annealing atmosphere (specifically pO_2) with the goal of increasing the compatibility of the surfaces with commercial line capabilities.

Chapter 4

Experimental Method

4.1 Introduction

As stated in the the previous section, the objective of this study is to evaluate the effect of Mn on the galvanizability of advanced high-strength steels (AHSS). Since the galvanizability is greatly dependent on the surface structure, it is critical to understand how the surface evolves prior to dipping. For this reason, there are three main parts to this chapter. First is an evaluation of the hardenability of high-Mn steels. Second is an investigation of the effect of oxidation potential during annealing on surface evolution prior to dipping, and finally to evaluate how the previously established surface affects reactive wetting kinetics during galvanizing. The overall process is outlined with respect to a continuous galvanizing line in figure 4.1.

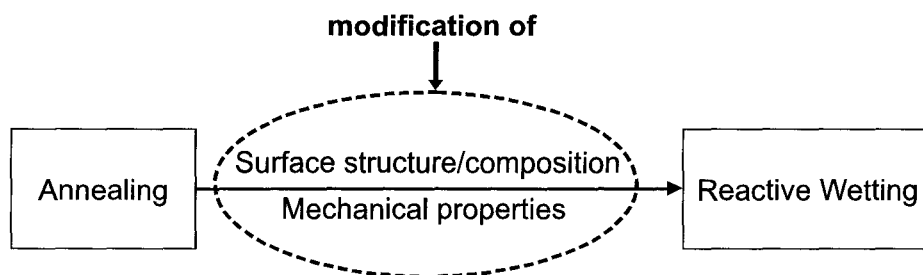


Figure 4.1: Schematic illustration of the two main steps in the continuous hot-dip galvanizing process.

4.2 Materials Systems Utilized

4.2.1 Substrates

This study was conducted with several steels, both laboratory grades and commercially available (table 4.1): an interstitial free (IF), a basic carbon manganese (CMn), a commercial dual-phase (DP590), and four laboratory-prepared dual-phase steels (DP-1 through DP-4). Although the chemistries listed show some compositional variations between alloying elements, the experimental variable being explored is the Mn content. As shown in table 4.1, the Mn content in this series of materials has a range of 0.14wt% to over 5wt%.

Table 4.1: Composition of substrates used in this study (in wt%)

Alloy Name	C	Mn	Mo	Si	Nb	Al	P	S	O (ppm)	N (ppm)
IF [§]	0.003	0.14	—	0.007	0.017	0.032	0.006	0.007	—	20
CMn [§]	0.060	1.40	0.003	0.090	0.071	—	0.008	0.001	—	60
DP590 [§]	0.070	2.36	0.070	—	0.002	0.049	—	—	—	80
DP-1 [†]	0.068	2.47	0.110	0.037	0.020	0.003	0.003	0.003	38	57
DP-2 [†]	0.077	2.98	0.086	0.028	0.022	0.007	0.005	0.003	30	42
DP-3 [†]	0.062	3.46	0.083	0.036	0.020	0.005	0.006	0.006	43	47
DP-4 [†]	0.071	5.10	0.086	0.030	0.021	0.005	0.005	0.004	36	49

[§] provided by Stelco, Inc., Hamilton, ON, Canada.

[†] fabricated at CANMET-MTL, Ottawa, ON, Canada.

Each steel was received as cold-rolled sheet in a range of thicknesses between 0.7mm and 1.9mm.

4.2.2 Reactive Wetting Bath

In the reactive wetting experiments, the bath composition was maintained at 0.20 \pm 0.02 wt% dissolved Al and was saturated with Fe as determined using figure 2.12.

To maintain this saturation, sufficient Fe was added to supersaturate the liquid and any Fe_2Al_5 which precipitated was skimmed prior to dipping experiments. All experiments were conducted using a bath temperature of 460°C . This alloy was prepared from special high grade (SHG) Zn and Zn-4.46wt%Al shot provided by Noranda, Inc.

4.3 Transformations During Continuous Cooling

To better understand the ability of these steels to be hardened through different heat treatments (also known as hardenability), a dilatometric investigation was undertaken. Dilatometry was used to identify austenite transformation temperatures during heating (A_c temperatures) and their counterparts during cooling (A_r temperatures) from their respective dilation curves. These experiments were also used to identify the temperatures associated with the formation of other products such as pearlite, bainite and martensite (α_M). By heating samples to a temperature above the A_{c3} temperature and quenching at different rates, the effect of cooling rate on transformation kinetics was investigated. An example treatment of the dilation vs. temperature curve is given in figure 4.2 where all transformations have been identified.

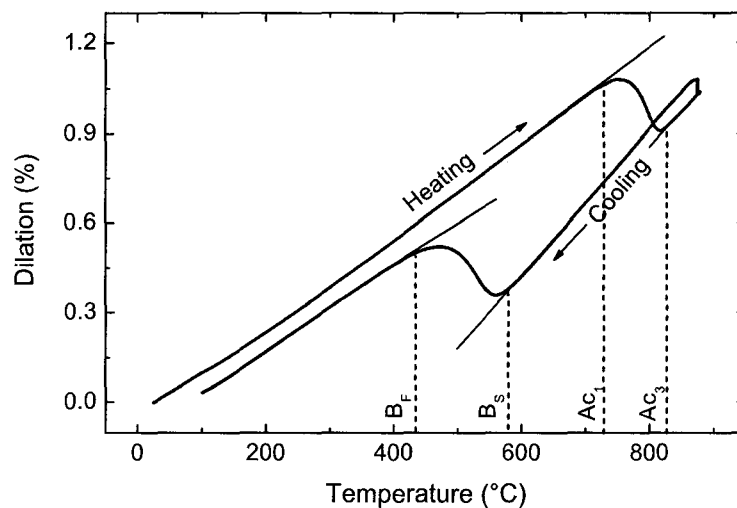


Figure 4.2: Example dilation curve for DP-2 at a cooling rate of $5^\circ\text{C}\cdot\text{s}^{-1}$ with treatment to identify transformation temperatures.

Dilatometric experiments were conducted on a BÄHR Thermoanalyse GmbH DIL805A quench/deformation dilatometer. This device utilizes a high frequency induction coil for heating, a linear variable displacement transducer (LVDT) for in-situ dilation measurements, and a coil inside the heating coil to carry the quenching gas (figure 4.3).

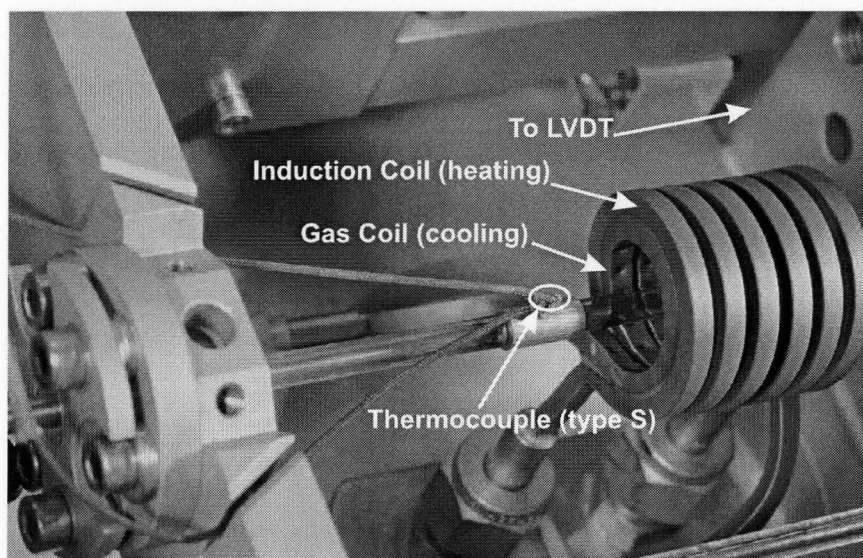


Figure 4.3: The dilatometer with sample mounted outside of induction/cooling coils before conducting a test.

Before each cycle, the sample chamber was evacuated to $\leq 5 \times 10^{-2}$ Pa and this was maintained throughout the heating and isothermal soaking stages. Quenching was conducted with either Ar or He gas depending on the required cooling rate. Sample temperature was monitored/controlled with a 0.1mm type-S thermocouple welded to the surface of the sample. The thermal profile for each sample involved rapid heating to the peak annealing temperature (PAT), isothermal soaking at the PAT for 5 min, followed by controlled Newtonian cooling (figure 4.4). Accuracy of the cooling rate was ensured by using a flow rate of gas that would cool the sample more quickly than desired and utilizing the induction coil to achieve the desired cooling rate. Since the

resultant thermal profile during cooling was non-linear, the target cooling rate was defined as the time required for the sample to cool from 800°C to 500°C ($t_{8/5}$).

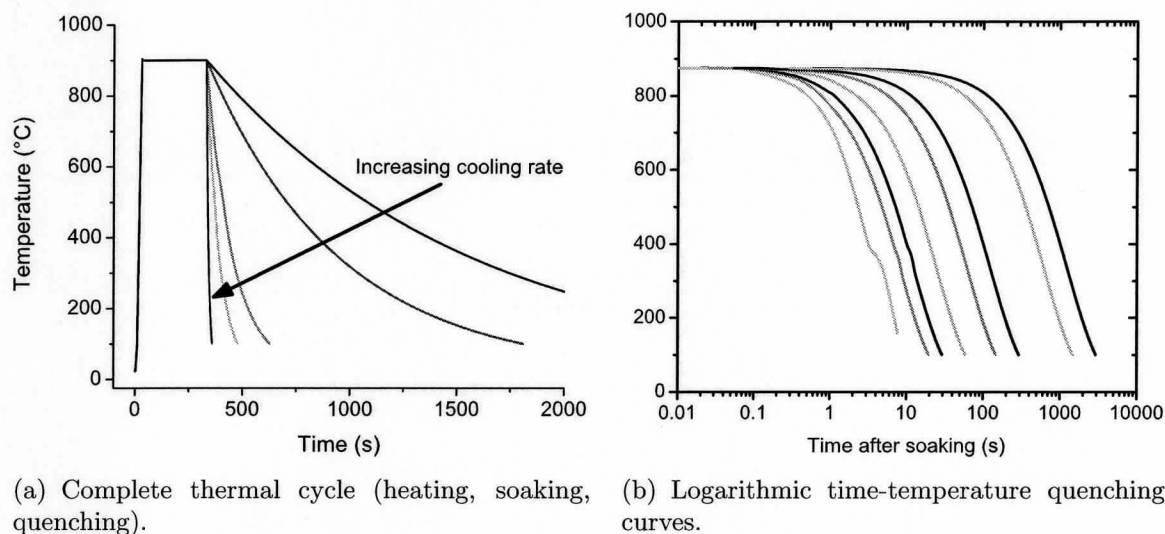


Figure 4.4: Schematic of thermal profiles used for the dilatometric experiments.

Samples from the experimental DP steels took the form of 10mm (L) \times 5mm (ϕ) cylinders machined from the hot-rolled billet. These samples were heated to 100°C in 10s, and then at the required rate to reach the PAT in an additional 20s.

Since the CMn and DP-590 alloys (table 4.1) were received as cold-rolled sheet, the samples comprised 10mm (L) \times 4mm (W) \times the cold-rolled thickness (\sim 1.6mm) coupons. In this case, the heating rate was decreased to reduce possible thermal distortion from rapid heating such that heating to the PAT from 100°C took 60s rather than 20s.

The Ac_1 and Ac_3 temperatures for all materials were determined by heating the sample slowly ($2^\circ\text{C}\cdot\text{min}^{-1}$) and determining the transformation temperatures with the dilation curves as shown in figure 4.2. To ensure that the samples were 100% γ before

quenching, the PAT for the quenching tests was taken as 50°C above the determined A_{C_3} .

4.4 Substrate Heat Treatments

4.4.1 Sample Preparation

Before samples were cut from the cold-rolled sheet, the sheet surfaces were ground with 1200 grit SiC paper to produce a uniform surface with minimal roughness. Cleaning followed with a solution of soap and water with a brush to dislodge any dirt or oil, then rinsed with water. This was repeated with an aqueous solution of 5% NaOH. Test coupons, 10mm × 50mm, were subsequently made with an abrasive water jet or mechanical shear depending on the thickness of the alloy. Immediately prior to heat treatment, the surface of the coupon was wiped with acetone. This process was deemed adequate by subsequent surface analysis which showed no measurable levels of contamination and supported by the similar results of Menéndez et al. (2007).

4.4.2 Thermal Profiles

Annealing experiments were conducted on a Rhesca® Force Balance Simulator, to be discussed in §4.6. Annealing cycles were carried out in a gold image infrared furnace surrounding a quartz tube which isolated the sample and process gas from the atmosphere.

All samples were heated to a PAT which, at equilibrium, would produce a microstructure containing approximately 30% γ and 70% α -ferrite. Thermo-Calc® and the TCS steel database v.2 were employed to determine this value for each steel. As

shown in figure 4.5, Mn is a γ stabilizer and decreased the PAT as it's concentration was increased.

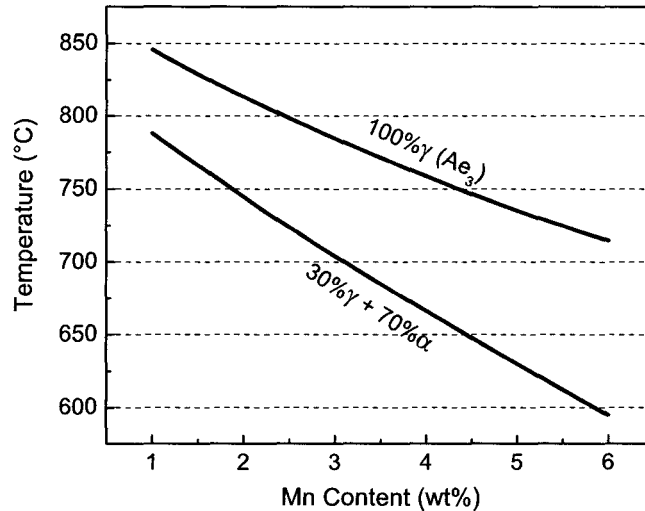


Figure 4.5: Variation in Ae_3 and intercritical annealing temperature as a function of Mn content for a typical low-carbon (0.07wt%) steel. (Calculated with Thermo-Calc® and the TCS steel database v.2.

The heating rate and soak time were chosen to mimic the Stelco, Inc. Z-line. In each case the thermal profile consisted of heating to the PAT in 200s, soaking for 120s and rapid cooling to room temperature in approximately 200s (figure 4.6).

4.4.3 Annealing Atmospheres

Different annealing atmospheres were used to determine how the substrate surface structure/composition varied as a function of Mn content and oxidation potential during intercritical annealing, and how this subsequently affected reactive wetting. As shown in §2.3.1, the oxidation potential of an isothermal, isobaric $N_2/5\%H_2$ atmosphere is controlled by the water vapour partial pressure, referred to in terms of the dew point. Four different dew points were explored ranging from $-50^\circ C$ to $+5^\circ C$. Oxidation potentials for each dew point at the alloy PAT are given in table 4.2 and

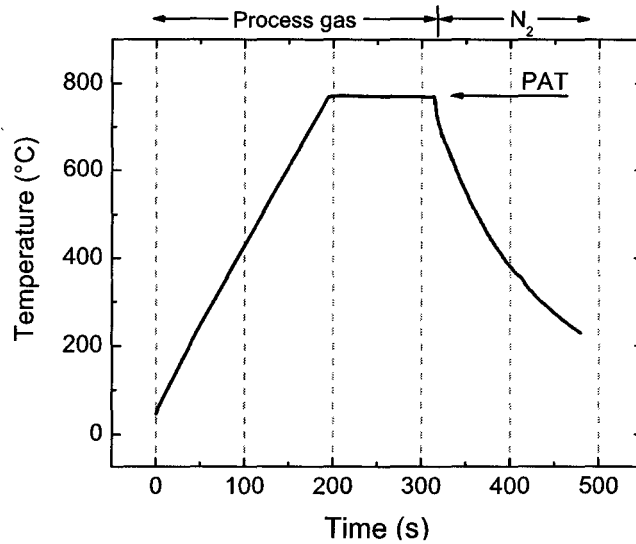


Figure 4.6: Thermal profile used for substrate heat treatments with peak annealing temperature (PAT) labeled.

were calculated using Thermo-Calc® with the SGTE pure substance database v.3 and the TCS steel database v.2 respectively.

Table 4.2: Peak annealing temperatures and oxidation potentials (in atm./at PAT) with given dew point used for substrate heat treatment and reactive wetting experiments.

Alloy Name	PAT (°C)	Dew point (°C)			
		-50	-30	-10	+5
IF	750	4.687×10^{-26}	2.935×10^{-24}	9.233×10^{-23}	8.549×10^{-22}
CMn	770	1.433×10^{-25}	8.977×10^{-24}	2.824×10^{-22}	2.615×10^{-21}
DP590	730	1.466×10^{-26}	9.183×10^{-25}	2.888×10^{-23}	2.675×10^{-22}
DP-1	724	1.026×10^{-26}	6.422×10^{-25}	2.020×10^{-23}	1.871×10^{-22}
DP-2	704	3.018×10^{-27}	1.890×10^{-25}	5.946×10^{-24}	5.505×10^{-23}
DP-3	685	9.012×10^{-28}	5.643×10^{-26}	1.775×10^{-24}	1.644×10^{-23}
DP-4	630	2.053×10^{-29}	1.286×10^{-27}	4.045×10^{-26}	3.745×10^{-25}

Before each sample was run, a vacuum was drawn on the sample chamber until the pressure reached ~ 10 Pa. This step was employed to remove oxygen and adsorbed moisture from the sample chamber before the annealing cycle. At this point, the chamber was re-filled with N_2 to ambient pressure and the $N_2/5\%H_2$ process gas

turned on. The process gas flow rate was $15.79 \text{ L}\cdot\text{min}^{-1}$ ($15 \text{ L}\cdot\text{min}^{-1} \text{ N}_2 + 0.79 \text{ L}\cdot\text{min}^{-1} \text{ H}_2$), as metered through rotameters until the isothermal soak was completed, after which ultra-high purity (UHP) N_2 was introduced. The use of UHP gas reduced the amount of oxidation after intercritical annealing, and allowed a much higher flow rate to increase the cooling rate.

4.4.4 Analysis of Oxide(s) Formed

Determination of the oxide thickness and oxidation state of surface species was performed using X-ray photoelectron spectroscopy (XPS). Although X-rays penetrate quite deeply into the sample, photoelectrons are very low energy and can only escape from very near the surface ($\sim 100\text{\AA}$). Analysis was conducted on the binding energy of the photoelectrons released from the sample via the following energy balance:

$$E_{\text{binding}} = h\nu_{\text{photon}} - E_{\text{kinetic}} - \phi \quad (4.1)$$

where h is Planck's constant, ν_{photon} is the frequency of the incident photon (X-ray), E_{kinetic} is the kinetic energy of the emitted photoelectron as measured by the spectrometer and ϕ is the work function of the instrument (calibrated for the specific instrument). An example of a spectrum acquired from the external surface of a sample is given in figure 4.7 as a function of binding energy and with the various peaks labeled.

To determine the oxidation state of Mn on the surface, the binding energy has to be resolved down to $\pm 0.25 \text{ eV}$. This requires that the acquired spectra be standardized by shifting it with respect to a known peak. In the case of steel samples, the well characterized Fe- $2p_{3/2}$ peak (at 706.62 eV) was used. After the spectra were shifted accordingly, the binding energy of the Mn- $2p_{3/2}$ peak could be determined and compared to published values for Mn-bearing oxides.

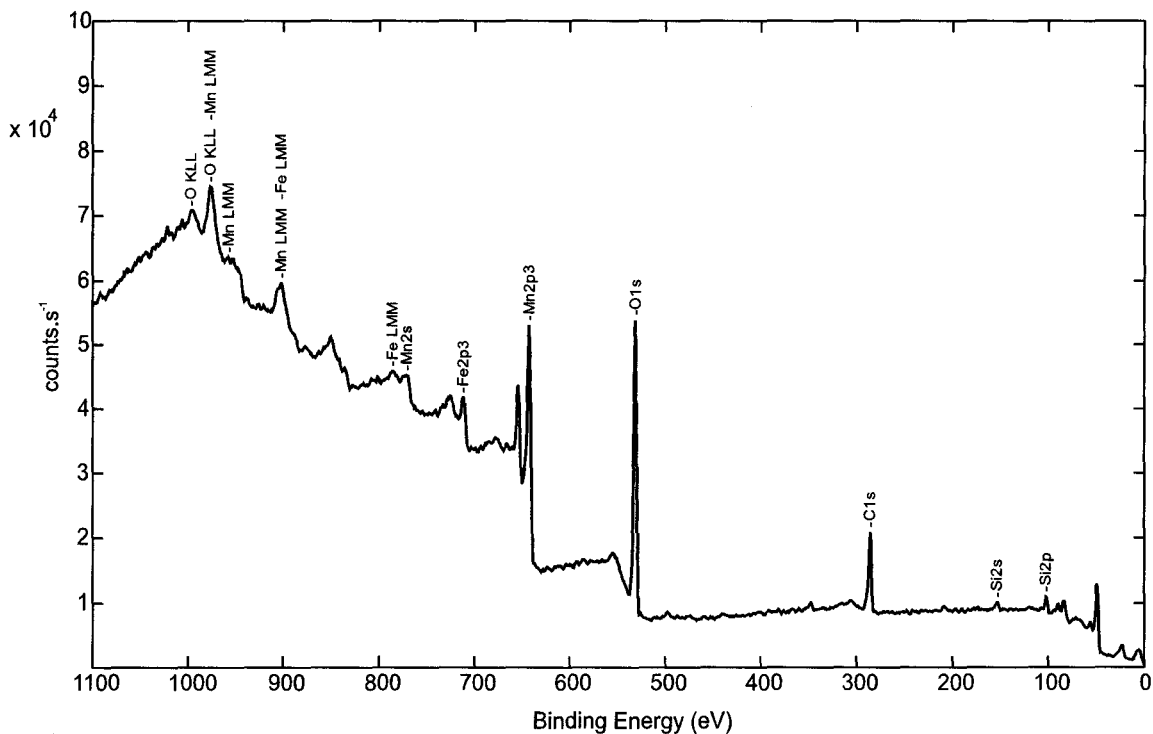


Figure 4.7: XPS survey spectrum acquired from CMn sample annealed using -30°C dew point atmosphere with various peaks labeled.

The instrument employed was a Physical Electronics Quantera SXM with an Al-K_{α} X-ray source using a $200\ \mu\text{m}$ beam size operating at $50\text{W}/15\text{kV}$. Detection of photoelectrons was conducted using a hemispherical energy analyzer with a pass energy of 140eV . After a spectrum was collected from the sample (i.e. figure 4.7), a sample area of $2\text{mm} \times 2\text{mm}$ was sputtered with a $4\text{kV}\ \text{Ar}^{+}$ ion beam and the analysis repeated to generate a compositional depth profile. Due to the change in composition throughout the depth of interest, the sputtering rate changes as a function of position causing the sputtering depth to not be completely accurate if a single rate is employed (Wetzig et al. 1997). Due to these constraints, all depths quoted in this work will be the equivalent depth in pure Fe, which carries an intrinsic error of $\pm 10\%$.

4.5 Reduction of MnO with bath Al

It has been argued that the ability to currently galvanize Mn-containing steels is implicit evidence of aluminothermic reduction (Khondker et al. 2007). Conversely, it could be argued that since oxides observed tend not to be continuous due to preferential oxidation at grain boundaries (Thorning and Sridhar 2007), the remaining steel surface reacts with the bath and the oxide particles are *'bridged'*. Looking forward, when the alloy content is increased and the oxides formed during annealing are thicker and more continuous, an un-wettable surface is observed (Drillet et al. 2004). A lack of oxide reduction during galvanizing has been observed with Ti and P-based oxides by Guttman et al. (1995), but this may not be the same with respect to MnO.

To determine if Al in the bath reduces MnO on the steel surface, an artificial steel/MnO system was prepared. Samples of IF steel were prepared with an electrodeposited layer of MnO_x . This was conducted with a solution of 20mM KMnO_4 , a current density of $2\text{mA}\cdot\text{cm}^{-2}$ and deposition time of two minutes. The technique of electrolytic deposition from KMnO_4 was adapted from the work of Wei et al. (2007). To ensure that the only species in the deposited layer was MnO, the resulting film was reduced to MnO using the heat treatment shown in figure 4.8 in a $\text{N}_2/5\%\text{H}_2$ atmosphere with a -40°C dew point. The required $p\text{O}_2$ was calculated in Thermo-Calc® with the SGTE pure substance database v.3. From figure 4.8, it can be seen that this atmosphere and temperature combination (indicated with a circle) is below the required $p\text{O}_2$ for MnO to be stable, but above the required $p\text{O}_2$ for metallic Mn to be stable ($\approx 10^{-32}$ atm.).

After heat treatment, samples were analyzed with XPS to ensure that the oxide was solely MnO. From the obtained spectra in figure 4.9a) and published values of the binding energy for multiple Mn-based oxides, it is clear that the film was predominantly MnO. Glow-discharge optical emission spectroscopy (GDOES) was

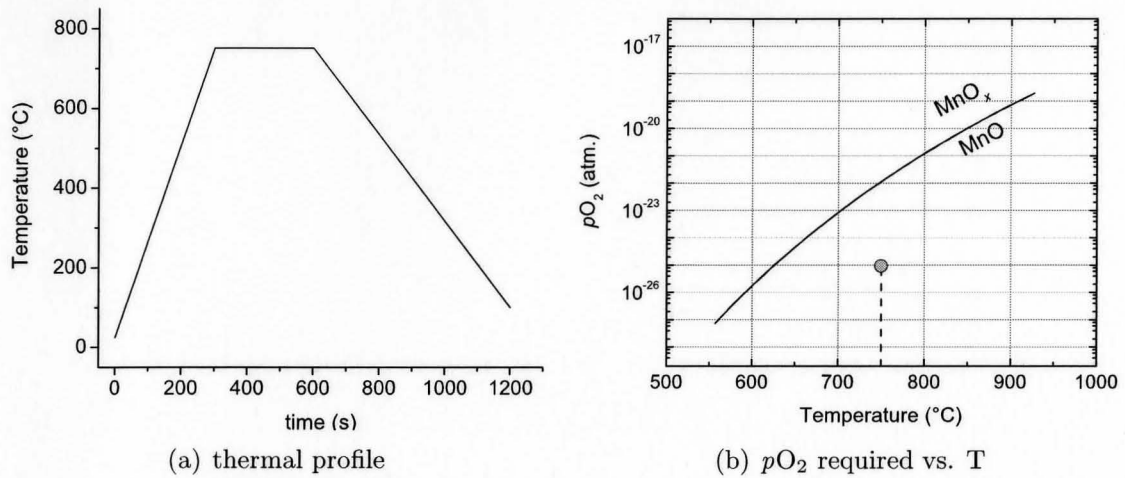


Figure 4.8: Heat treatment used to reduce the deposited film from MnO_x to MnO .

used to measure the thickness of the oxide (figure 4.9b) and it was found to be approximately 700nm. In comparison to the oxide found after annealing (figure 5.8), this was quite thick.

Subsequently, samples were dipped for various times in a galvanizing bath (Zn-0.2wt%Al, Fe saturated) or a pure Zn bath – both held at 460°C. Due to the slower reaction rate in pure Zn, longer reaction times were chosen compared to the Zn-Al bath. The experimental conditions explored are listed in table 4.3. Analysis was conducted by sectioning and polishing samples for SEM examination.

Table 4.3: Variables explored in MnO reduction experiments

Bath composition	Reaction time (s)
Zn	20
	60
Zn-0.2wt%Al	5
	10
	20

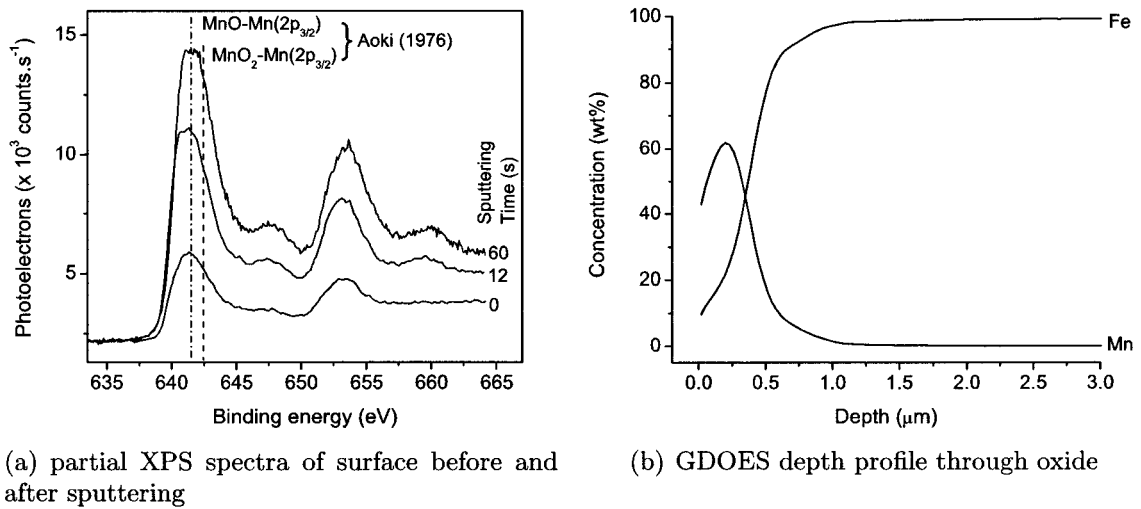


Figure 4.9: Size and nature of deposited and annealed film.

Although not as defined as the GDOES measurements in figure 4.9b), an EDX line scan of a sample before exposure to molten metal showed an oxide of Mn with similar thickness ($\sim 700\text{nm}$).

4.6 Reactive Wetting Kinetics/Wettability

As mentioned in §2.4, there has been little or no data published on reactive wetting kinetics when the system is limited by reactions before dipping (i.e. oxidation) and the formation of the inhibition layer. This is due to the fact that the incubation period is very short when the surface is free from oxides ($\leq 1\text{s}$) [Chen 2007], and the reactive wetting process is delayed by oxides on the surface to an extent which is not fully understood (§2.3.3). Moreover, the typical method of quantifying the reaction rate is to measure the amount of Al at the steel-Zn interface. This means that the transition from an oxidized surface to a reactively wet surface is not observed.

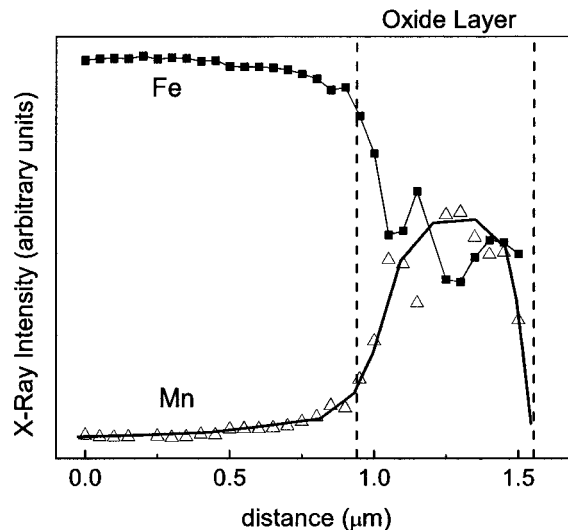


Figure 4.10: EDX line scan identifying MnO film and thickness similar to GDOES measurements in figure 4.9b).

To observe the reactive wetting process, specifically when limited by oxidation during annealing, a method of inferring the contact angle from a force balance was employed. The modified Rhesca® Force Balance Simulator used for the heat treatment experiments (§4.4) was employed to perform these measurements. A schematic of the device is given in figure 4.11 with the main areas of interest being the infrared furnace for annealing, an electrobalance to suspend the sample and measure forces acting on the sample during immersion in the the reactive Zn-Al-Fe bath. As well as modifications to allow rapid cooling, the drive system was modified to allow a more rapid transition from annealing to immersion in the bath - preventing further oxidation.

A submerged K-type thermocouple was used to maintain the bath temperature at $460 \pm 2^\circ\text{C}$. The composition of the bath was also fixed at 0.20 ± 0.02 wt% dissolved Al and was saturated with Fe (McDermid et al. 2007) as described in §4.2.2. By fixing the temperature and composition of the bath, all intrinsic properties such as the surface tension (γ_{LV}) and density (ρ_{bath}) of the molten alloy were held constant

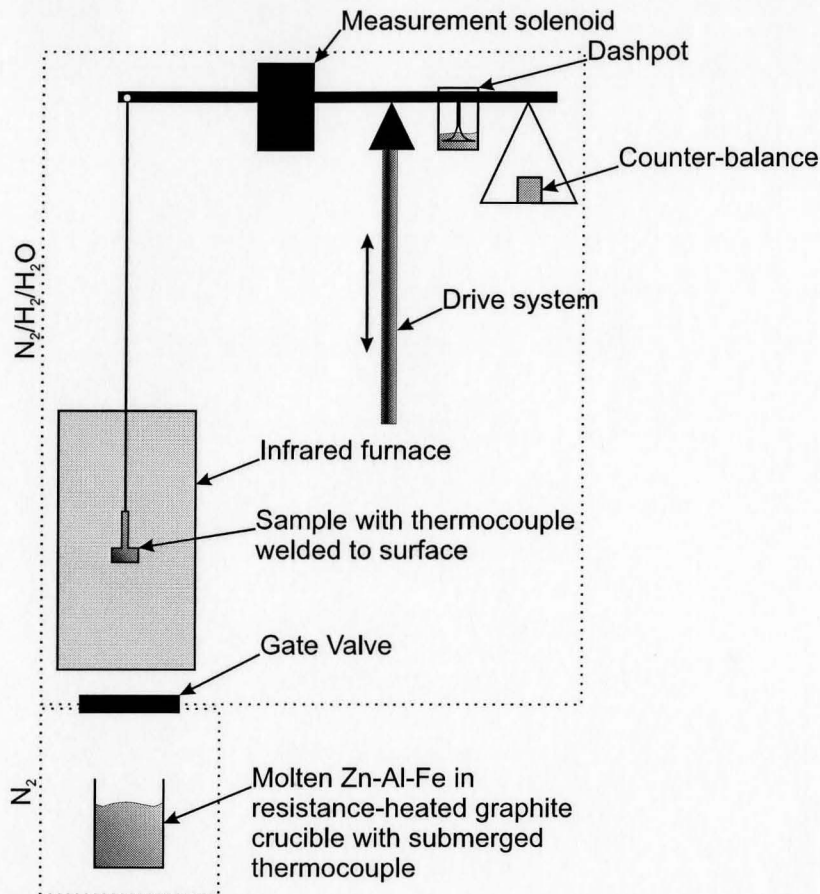


Figure 4.11: Schematic illustration of the wettability testing apparatus. Dotted lines represent controlled atmosphere boundaries.

for all experiments. Variations in measured values of γ_{LV} can be observed in metals and alloys due to surface oxidation (Roach and Henein 2005). To minimize this effect, a vacuum was drawn on the bath chamber followed by a constant flow of dry N₂ ($\sim 1\text{L}\cdot\text{min}^{-1}$) throughout the experiment. Additionally, the bath surface was skimmed immediately prior to dipping to minimize the amount of oxidation which could interfere with measurements.

Samples for reactive wetting experiments were cut from cold-rolled sheet using an abrasive water-jet to achieve the geometry shown in figure 4.12. A K-type control thermocouple ($\pm 0.2^\circ\text{C}$) was welded to the surface of the sample to provide feedback to the furnace controller.

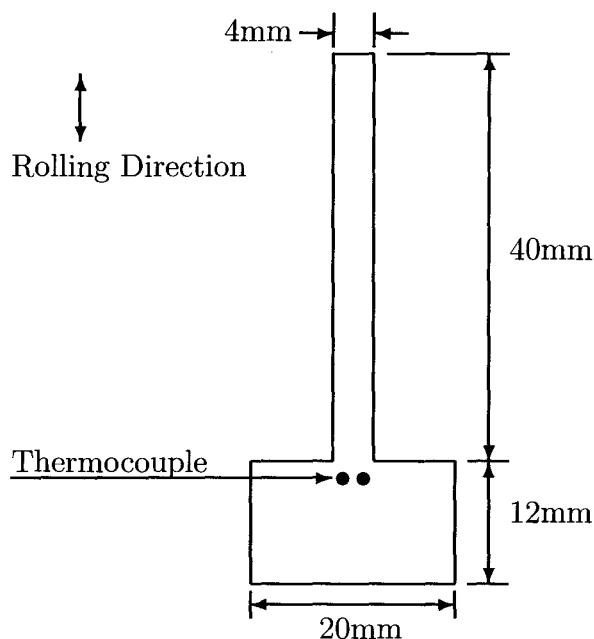


Figure 4.12: Sample geometry used for reactive wetting experiments.

The sample geometry was chosen to minimize mass and inertia acting on the balance, while maximizing width:thickness ratio (thereby limiting edge effects), and maintaining sufficient length to ensure that the sample rod was not significantly heated during annealing. Two distinct areas exist in figure 4.12: the thin, top portion was clamped to the drive rod; while the wider, bottom portion was dipped into the bath. To minimize the effect of the rough edges from water jet cutting, sample edges were ground with 1200 grit SiC paper.

The samples were heat treated using the same cycle as described in §4.4.2, but with linear cooling from the PAT to dipping temperature (figure 4.13) due to the constraints of the equipment controller to allow subsequent dipping. Process gas was used from the beginning of the cycle until the end of the isothermal section; after which N_2 was used for cooling as indicated in figure 4.13. Process gas pO_2 was fixed by controlling the dew point of the atmosphere, as shown in table 4.2, to explore the effect of the surface evolved during annealing on wettability.

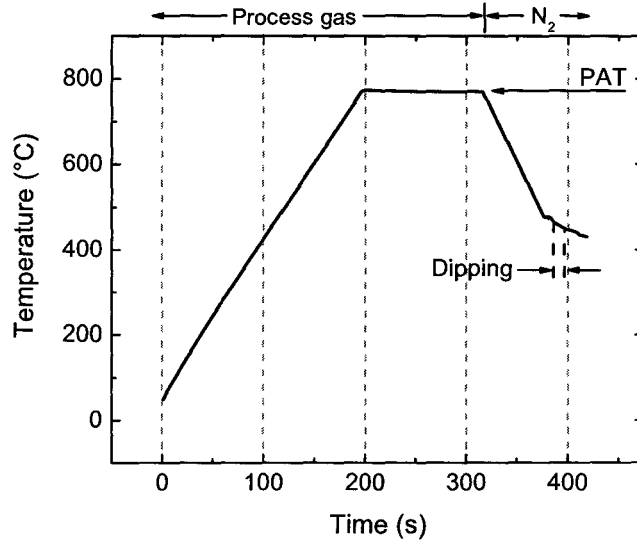


Figure 4.13: Thermal profile used for reactive wetting experiments with peak annealing temperature (PAT) and dipping labeled.

All samples were immersed in the Zn-Al-Fe bath to a depth of 8mm at a rate of $15\text{mm}\cdot\text{s}^{-1}$, resulting in a travel time of $\sim 0.533\text{s}$ from initial surface contact to the final depth. Sample contact with the bath was monitored by a continuity circuit. The sample was fully immersed for 10s while data was collected from both the thermocouple on the sample and the electrobalance at a rate of 6Hz.

The force measured by the electrobalance (equation 4.2) is composed of three parts: (i) the force of gravity (mg) which is constant for a sample of constant mass; (ii) a buoyancy force caused by a difference in pressure between the surface of the bath and the bottom of the sample which is equivalent to the displacement of liquid bath ($V_{\text{displaced}}\rho_{\text{bath}}g$) and (iii) the wetting force which is the surface tension of the bath (γ_{LV}) acting at the contact angle (θ) on the sample. The resultant force is the product of γ_{LV} , the length of the triple line (P), and cosine of the contact angle ($\cos\theta$).

This term can be thought of as a ribbon of constant force per unit length (γ_{LV}) acting on a specific width and resolved in the vertical direction.

$$\begin{aligned} F_{\text{measured}} &= F_{\text{gravity}} - F_{\text{buoyancy}} + F_{\text{wetting}} \\ &= mg - V_{\text{displaced}}\rho_{\text{bath}}g + P\gamma_{LV}\cos\theta \end{aligned} \quad (4.2)$$

If the surface is reactively wet, the contact angle decreases with time while buoyancy and gravitational forces remain constant. Thus, any change in F_{measured} is due to a change in the wetting force – an increasing value being indicative of the progression of wetting. Figure 4.14 shows how as the liquid moves up the sample, the contact angle decreases.

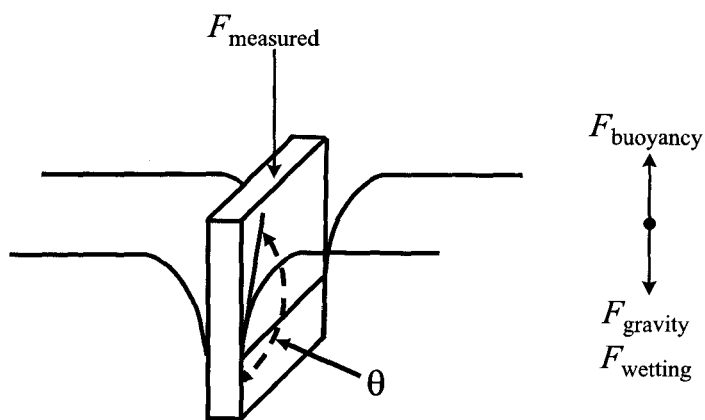


Figure 4.14: Schematic diagram of method used to measure forces during reactive wetting and components of F_{measured} .

4.6.1 Effect of the contact angle on F_{buoyancy}

Although the actual height of liquid on the sample and volume displaced changes during the experiment due to the change in contact angle, F_{buoyancy} remains constant

since the hydrostatic pressure at the bottom of the sample remains constant. This pressure exerted by the liquid can be calculated as:

$$p = \rho_{\text{bath}} g y \quad (4.3)$$

where y in equation 4.3 is the depth to which the sample is immersed in the liquid. It could be argued that the liquid height on the sample, a function of θ and the radius of curvature of the meniscus, should be used. This apparent depth, labeled h in figure 4.15, does not affect the hydrostatic pressure because the force exerted by γ_{LV} to create the curvature of the liquid surface balances the loss of gravitational potential energy with the creation of additional liquid surface area. This can be thought of as a criterion for mechanical equilibrium in a solid/liquid/vapour system.

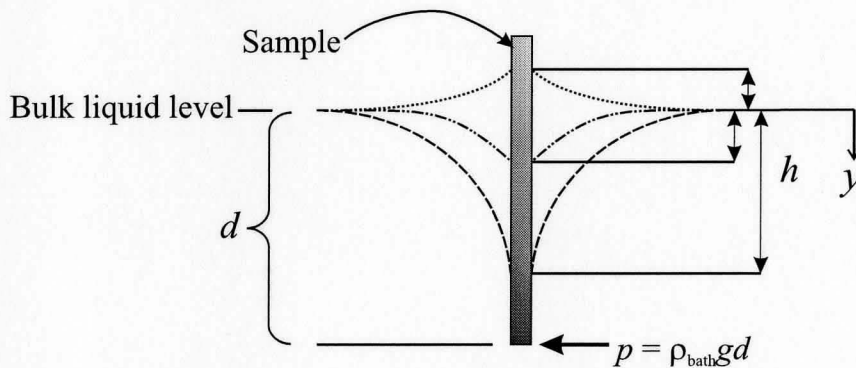


Figure 4.15: Effect of changing the contact angle on immersion depth, d , and apparent depth, h .

Thus, the hydrostatic pressure below the sample is the same as the bulk of the liquid at a depth d (labeled in figure 4.15). If this were not the case, gradients in pressure would result in pressure-induced fluid flow under the sample. For this reason, the contact angle does not have an effect on F_{buoyancy} and it remains constant throughout the experiment.

4.6.2 Observation of Interfacial Reaction Products

Investigation of any substrate/coating interfacial reaction products was conducted by dissolving the Zn overlay with $\text{H}_2\text{O}/10\%\text{H}_2\text{SO}_4$. This solution dissolves the Zn overlay and then slowly dissolves both the Fe_2Al_5 -inhibition layer and any Fe-Zn intermetallic compounds. By removing the sample after the metallic overlay is removed, any interfacial reaction products can be observed.

After removal of the overlay, a JEOL 7000F scanning electron microscope (SEM) was used to observe the morphology of the interfacial layer. In this case, a low accelerating voltage (10kV) was used to minimize the interaction volume and maximize the fraction of the detected signal which originated from the area of interest.

Chapter 5

Results

5.1 Introduction

As per the previous section, this chapter is laid out in an order which mimics the order of the industrial continuous hot-dip galvanizing process. Thus, the properties of these alloys as determined by dilatometry is first discussed followed by the evolution of the surface structures during heat treatment and finally the galvanizing reaction measurements.

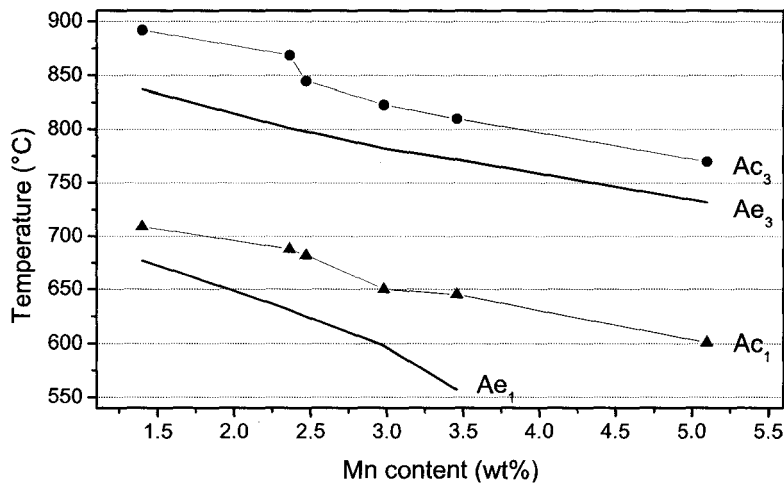
5.2 Hardenability Variations With Mn Content

A_{c1} and A_{c3} temperatures for all dilatometry samples, along with the PAT used in subsequent quenching experiments are given in table 5.1. The first two values were determined by heating the sample at a rate of $2^{\circ}\text{C}\cdot\text{min}^{-1}$ and the third was chosen as $\sim 50^{\circ}\text{C}$ above the A_{c1} for subsequent quenching experiments.

The measured transformation temperatures (A_{c1} and A_{c3}) show a marked decrease with increasing Mn content similar to that seen in the equilibrium calculations (figure 5.1), but the equilibrium values were consistently lower than those observed. This is likely due to the diffusive nature of carbide dissolution from the cold-rolled structure and because measurements were made at a heating rate higher than that which would be used for equilibrium measurements.

Table 5.1: Ac_1 and Ac_3 transformation temperatures determined with dilatometry and PAT used in subsequent quenching experiments.

Alloy Name	Ac_1	Ac_3	PAT
	°C		
CMn	709	892	940
DP590	688	869	920
DP-1	682	845	900
DP-2	650	823	875
DP-3	645	810	860
DP-4	601	770	820

Figure 5.1: Experimentally determined transformations temperatures during heating at $2^\circ\text{C}\cdot\text{min}^{-1}$ (Ac_x) compared with calculated equilibrium values (Ae_x).

It is noteworthy that DP-4 (5.10wt% Mn) does not have an Ae_1 temperature in figure 5.1. This is because at these levels of Mn, the alloy is partially austenitic at room temperature as illustrated with the Fe-Mn phase diagram in figure 5.2. The segregation and non-equilibrium structure of the as-rolled samples resulted in a detectable phase transformation for this sample despite the fact that no equilibrium transformation exists.

CCT diagrams for each of the alloys listed in table 4.1 except for IF (not used for its hardenability) are presented in figures A.1 through A.6 of Appendix A. The general trend of decreasing transformation temperatures (B_S , B_F , M_S , M_F) with

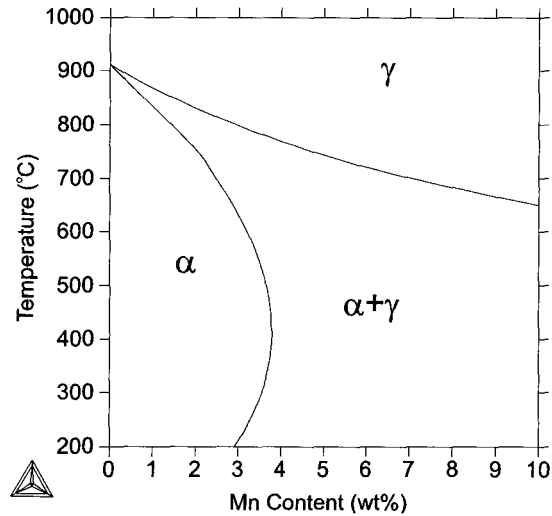


Figure 5.2: Partial Fe-Mn phase diagram illustrating effect of Mn content on low temperature γ stability, and subsequent lack of Ae_1 . Calculated with Thermo-Calc® and the TCS steels database v.2.

increasing Mn content indicates increased γ stability. For the range of compositions explored, the M_S varied from 425°C - 340°C with increasing Mn content (figure 5.3).

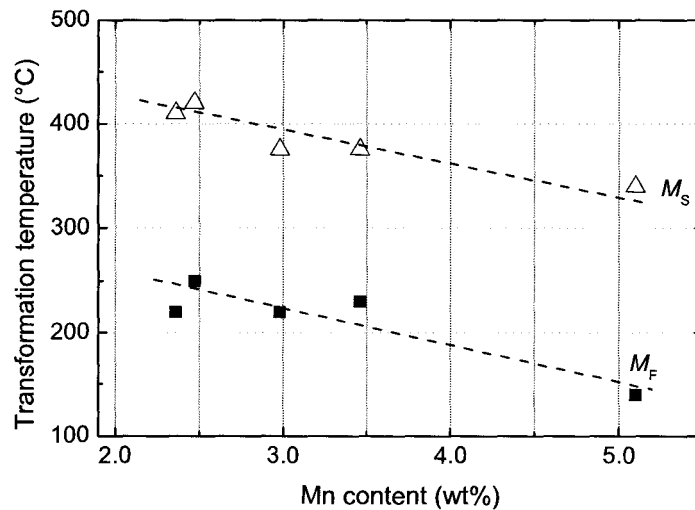


Figure 5.3: Experimentally determined transformations temperatures during cooling.

As well, a decrease in the critical cooling rate required to form a microstructure without bainite was observed from the location of the bainite ‘nose’ for each alloy. The $\gamma \rightarrow$ bainite transformation field for several alloys is shown in figure 5.4 where

it is evident that increased alloy Mn decreased the temperature of the bainitic nose and shifted it to longer times.

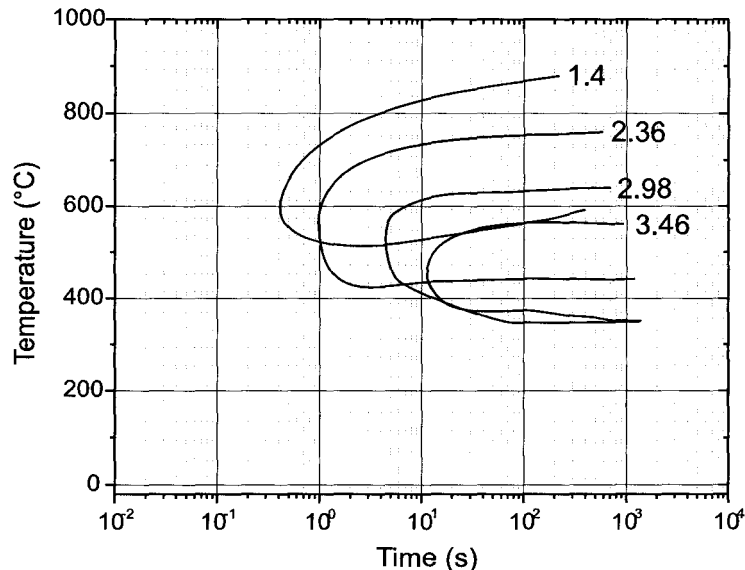


Figure 5.4: Variation in the bainite transformation field versus Mn content (wt%) during continuous cooling.

An examination of the extreme cases, the CMn alloy (1.4wt% Mn) exhibited no M_S temperature at the cooling rates explored while DP-4 was shown to only form martensite over the entire range of experimental cooling rates.

5.3 Selective Oxidation During Annealing

To separate segregation and oxidation during rolling from that caused by annealing, depth profiles were constructed for the as-received, cold-rolled samples as well as after heat treatment. No appreciable Mn surface segregation was observed for the as-received samples (figure 5.5) which allows all subsequent changes from the bulk concentration to be attributed to the effects of the heat treatment and process atmosphere. It should be noted that no detectable oxidized Si was found during the XPS examination. Carbon was also removed from the figures since surface contamination

with C from the environment is unavoidable and is therefore considered to be an artefact in XPS analyses (Menéndez et al. 2007). However, the as-received profiles show an increase in O content at the surface as well as a decrease in Fe content when compared to the bulk (figure 5.5). This is typical of a steel exposed to air, forming an Fe-based oxide as metallic Fe is unstable in air at room temperature (extrapolated from figure 2.9).

All alloys exhibited similar surface chemistry evolutions during annealing. As expected, all Fe-based oxides were reduced by all process atmospheres used. Furthermore, Mn segregated to the surface in varying amounts, showing in some cases a significant increase in concentration. Using XPS spectra, concentration depth profiles were constructed for all alloys and annealing atmospheres.

An example of the XPS spectra obtained as a function of sputtering depth, focused on the Mn-2p region, is shown in figure 5.6. In this figure, the variation in the rate of photoelectrons detected indicates a change in composition of the surface being analyzed - specifically a change in Mn content. As the sputtered depth increases, a steady state spectrum was obtained with much lower peak intensities. An analysis of the binding energies for the compounds present determined that the observed Mn-2p_{3/2} peak was consistent with MnO (Aoki 1976; Franzen et al. 1976; Foord et al. 1984; Strohmeier and Hercules 1984). This species was the Mn-oxide observed for all alloys and annealing atmospheres.

Figure 5.7 shows the impact of the annealing atmosphere on the surface chemistry of the IF sample. As this alloy contains only 0.14wt% Mn, the variation of the depth profiles with dew point is minor. The progression to higher Mn content alloys in figures 5.8 through 5.13 shows how this increased segregation and oxidation during heat treatment.

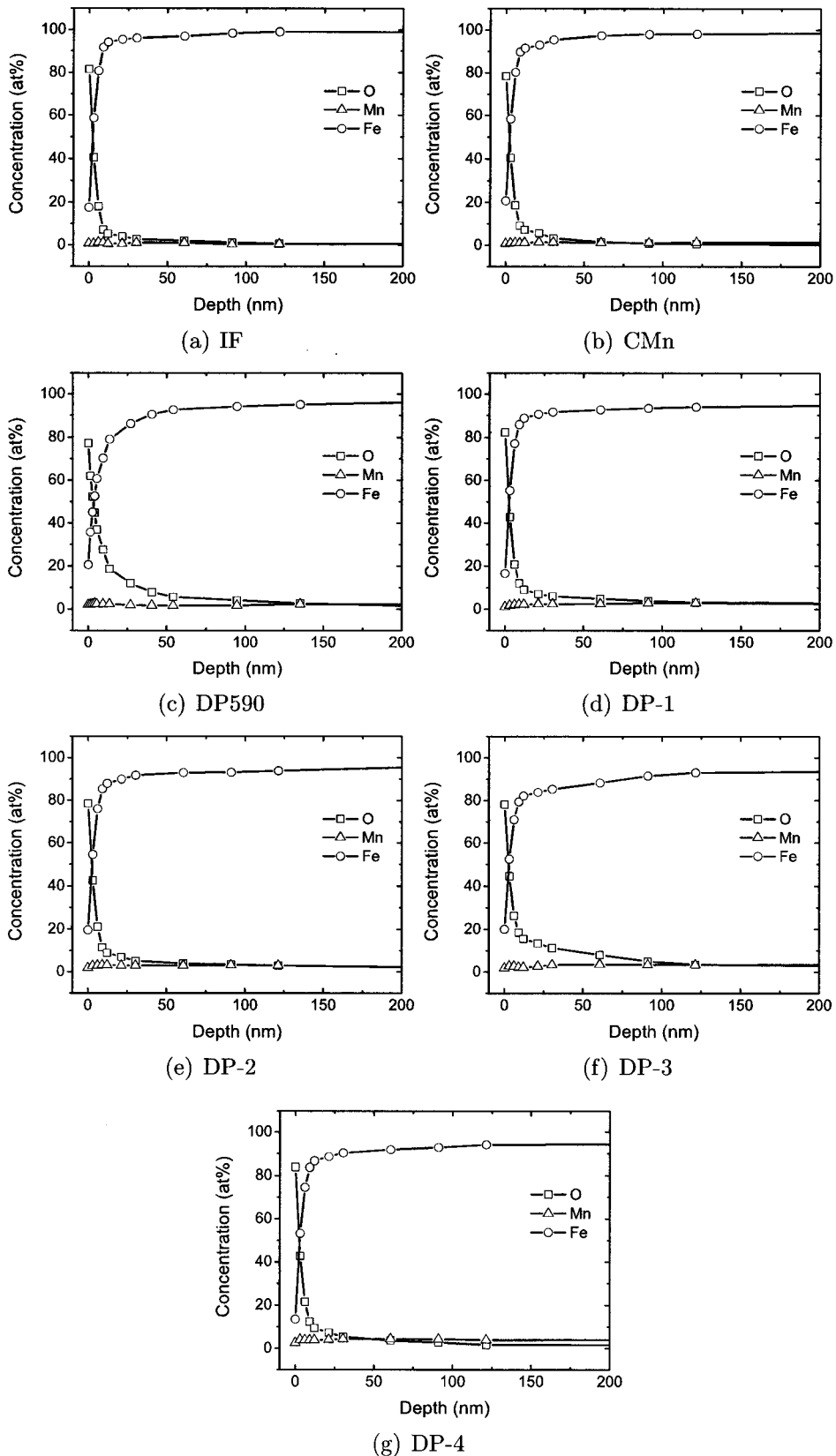


Figure 5.5: Compositional depth profiles for the as-received samples.

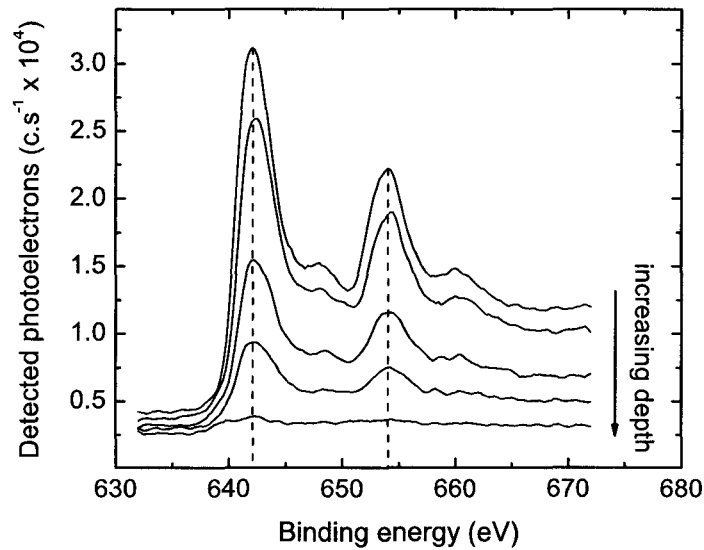


Figure 5.6: Partial XPS spectra of DP-4 sample showing Mn segregation to the surface after annealing at -50°C dew point.

Oxide thickness was assessed by measuring the depth at which the Mn concentration profile reached one-half of its maximum value, or the so-called full width at half-maximum (FWHM). The impact of varying the $p\text{O}_2$ by changing the dew point from -50°C to -30°C becomes more obvious in figure 5.14. In this case, the oxide is much thicker when annealing at -30°C . Even the IF sample, which contains a small amount of Mn (0.14wt%) and was used as a reference material, exhibited an increase in Mn FWHM from approximately 7 to 12nm.

Following these methods, the XPS depth profiles were able to show variations in oxide thickness as well as the nature of the oxide growth as a function of annealing atmosphere $p\text{O}_2$. Comparing the profiles for each atmosphere (figures 5.7–5.13), several trends can be observed:

1. At the lowest $p\text{O}_2$ (-50°C dew point):
 - Oxidation for all alloys is limited to the external surface

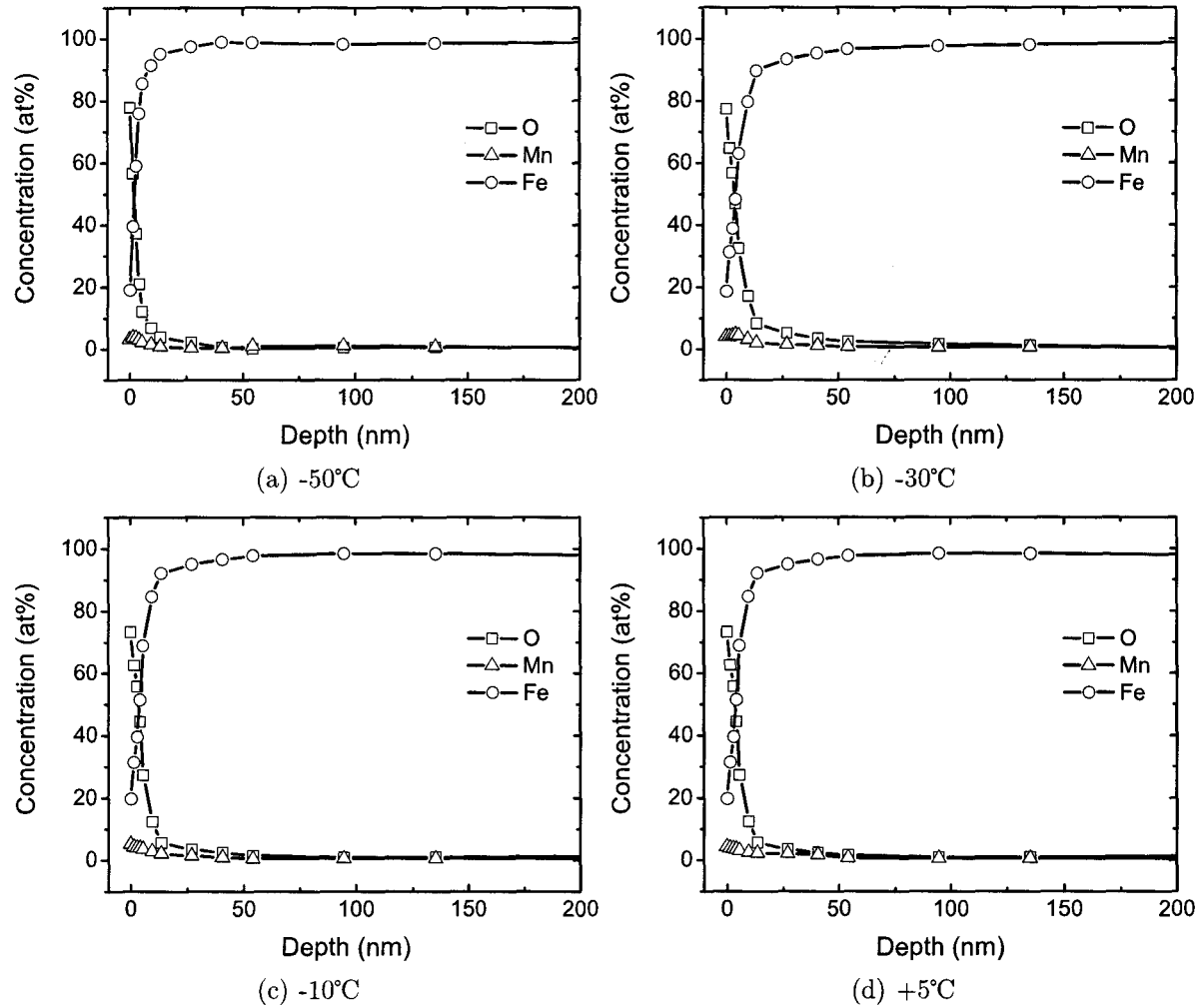


Figure 5.7: Compositional depth profiles for IF (0.14wt% Mn) samples after heat treatment in various dew point atmospheres.

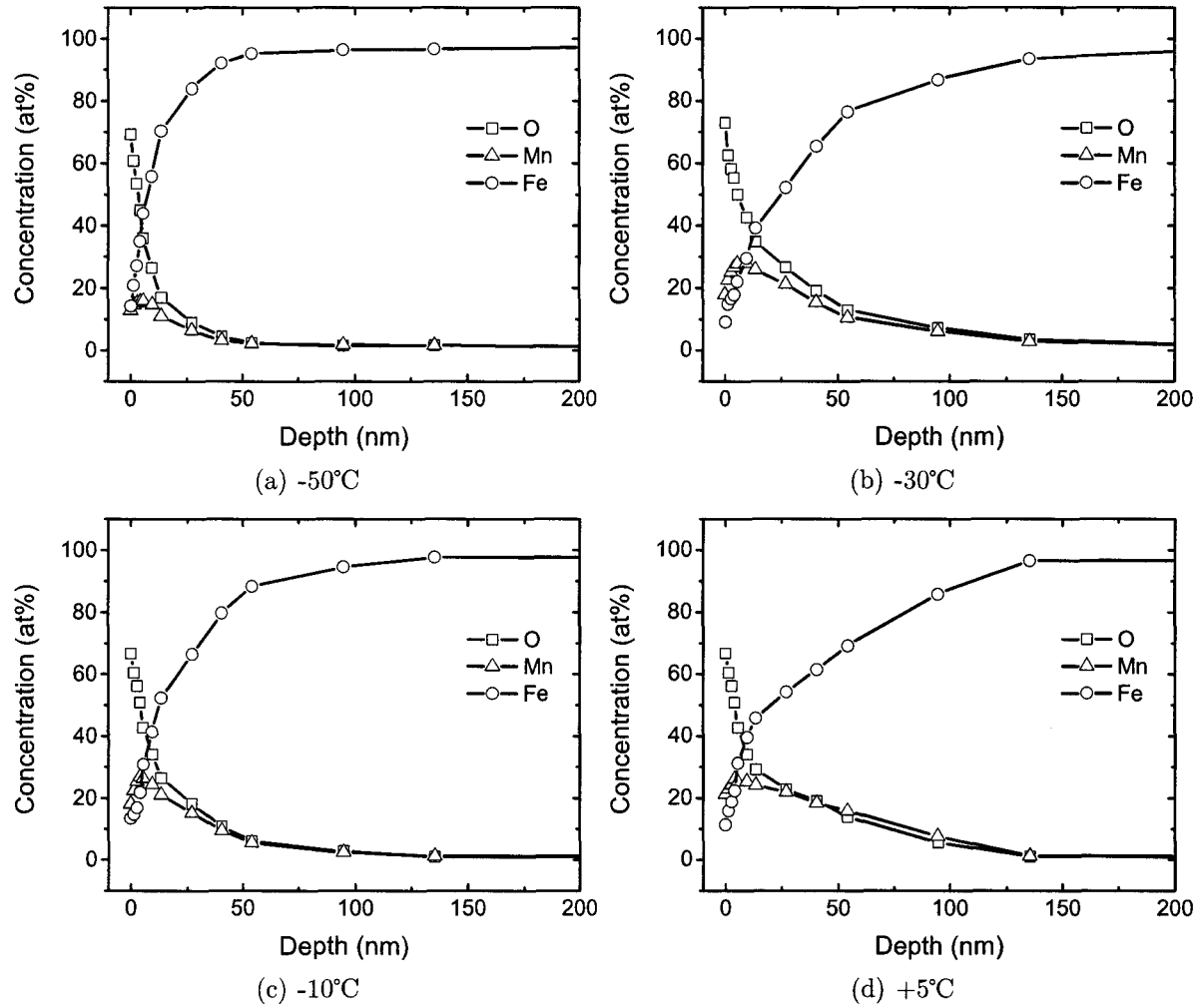


Figure 5.8: Compositional depth profiles for CMn (1.40wt% Mn) samples after heat treatment in various dew point atmospheres.

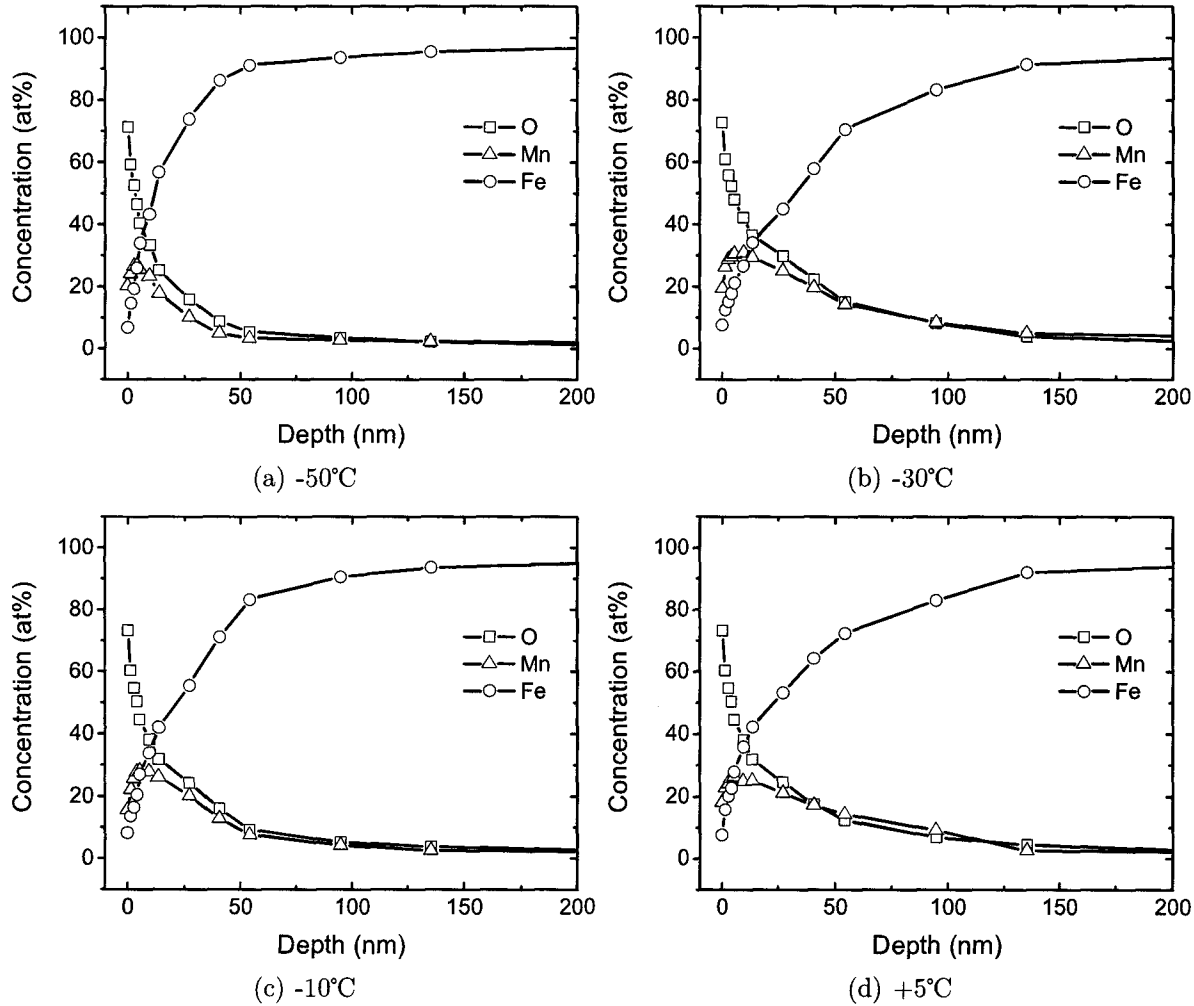


Figure 5.9: Compositional depth profiles for DP590 (2.36wt% Mn) samples after heat treatment in various dew point atmospheres.

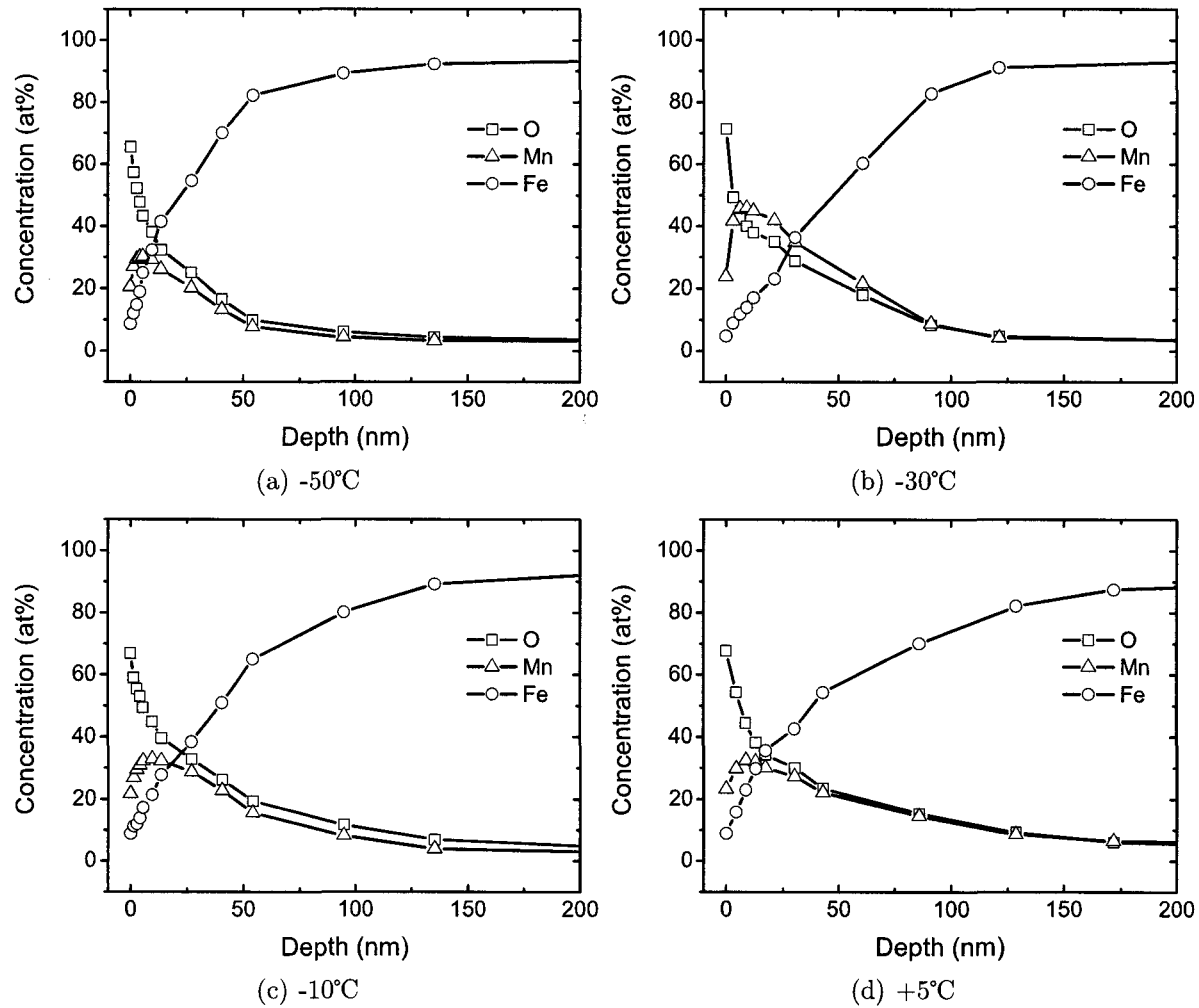


Figure 5.10: Compositional depth profiles for DP-1 (2.47wt% Mn) samples after heat treatment in various dew point atmospheres.

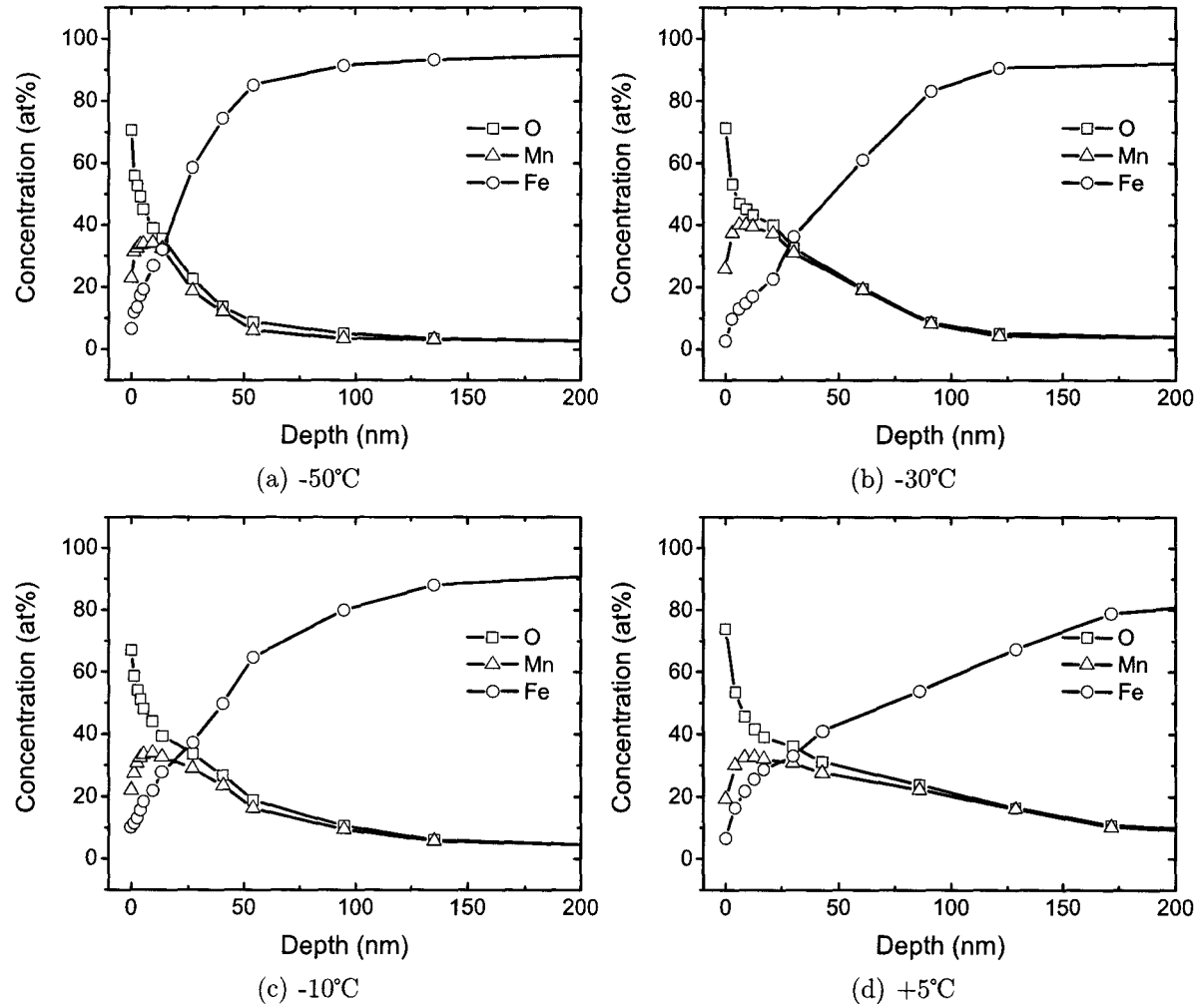


Figure 5.11: Compositional depth profiles for DP-2 (2.98wt% Mn) samples after heat treatment in various dew point atmospheres.

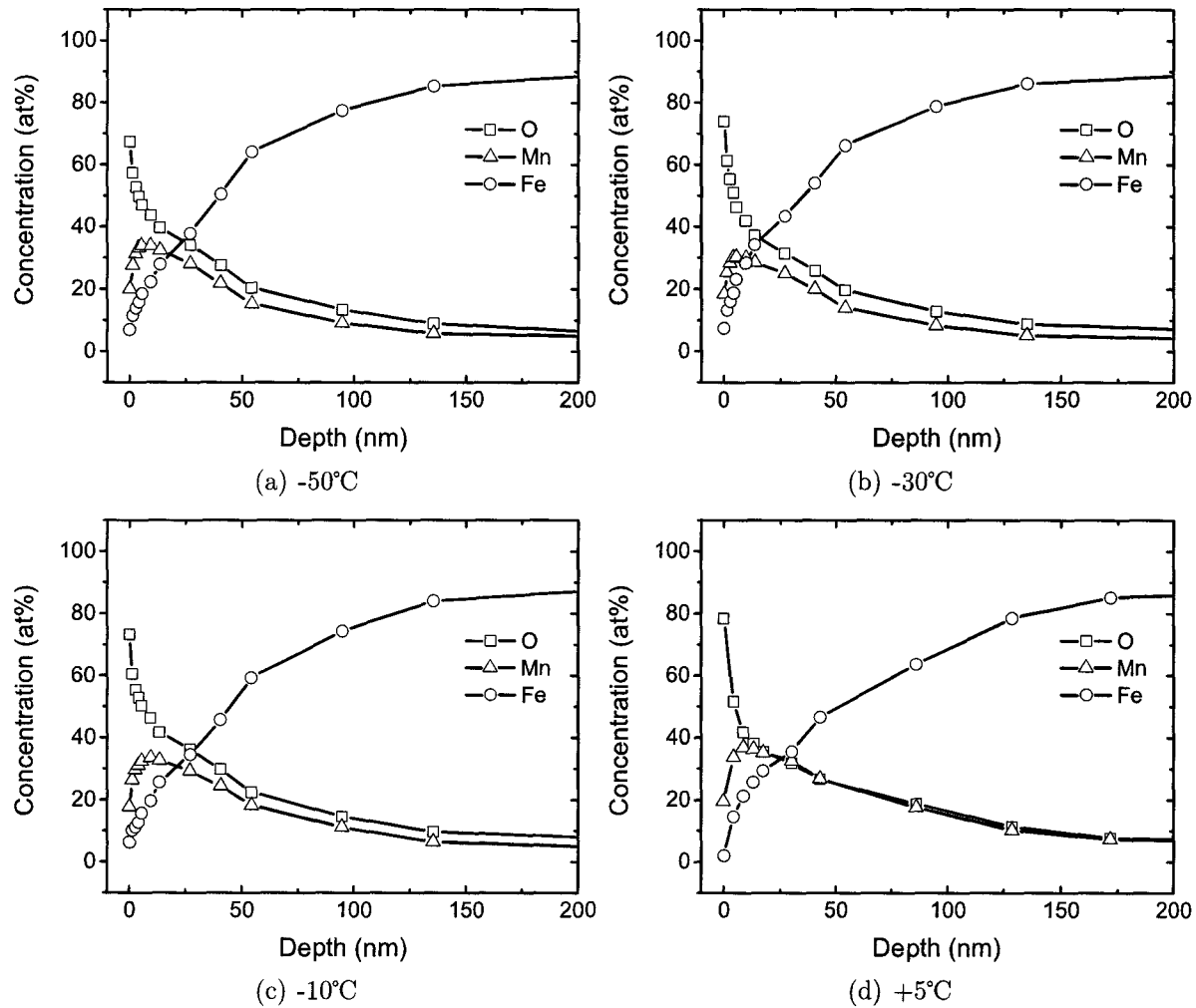


Figure 5.12: Compositional depth profiles for DP-3 (3.46wt% Mn) samples after heat treatment in various dew point atmospheres.

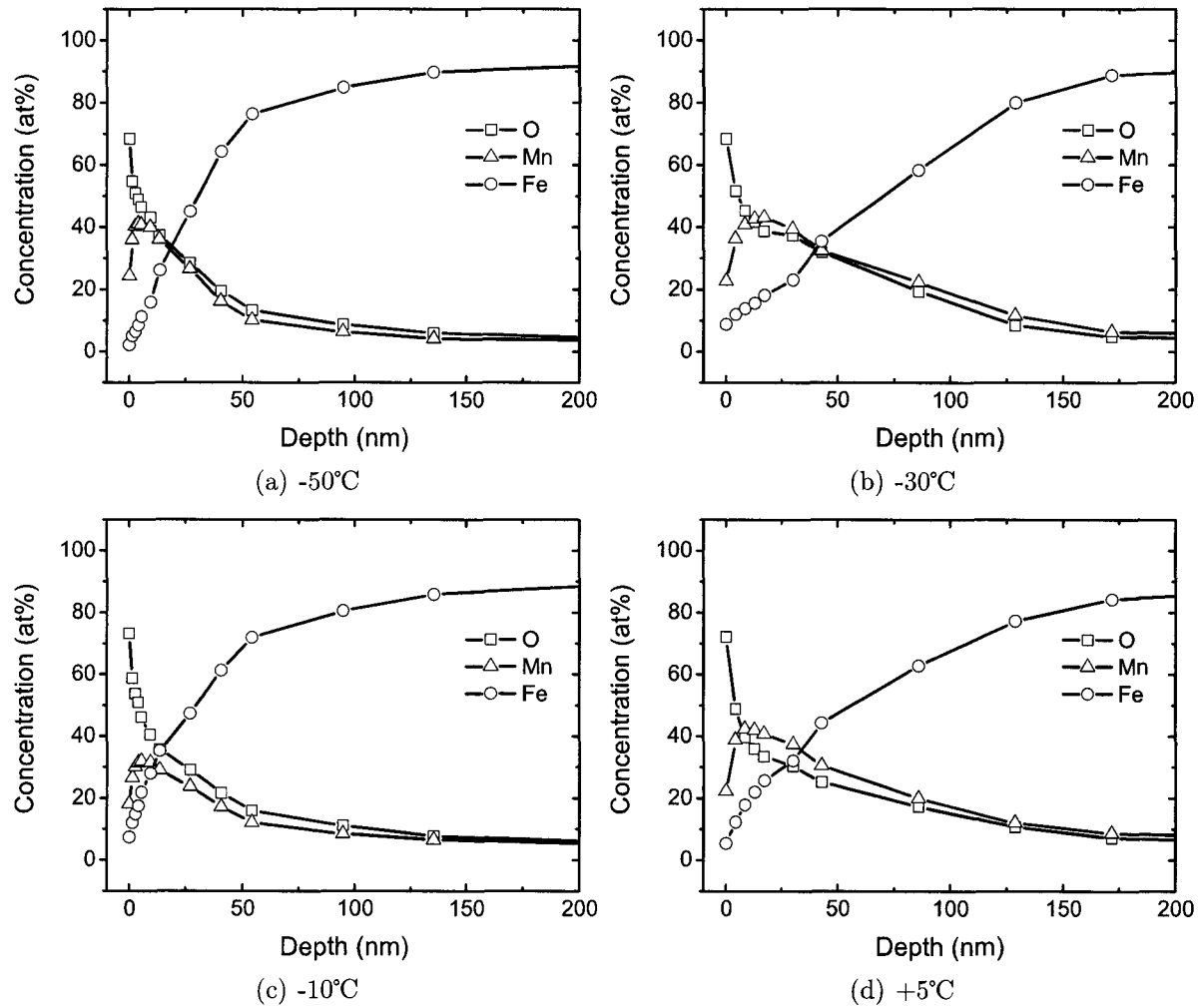


Figure 5.13: Compositional depth profiles for DP-4 (5.10wt% Mn) samples after heat treatment in various dew point atmospheres.

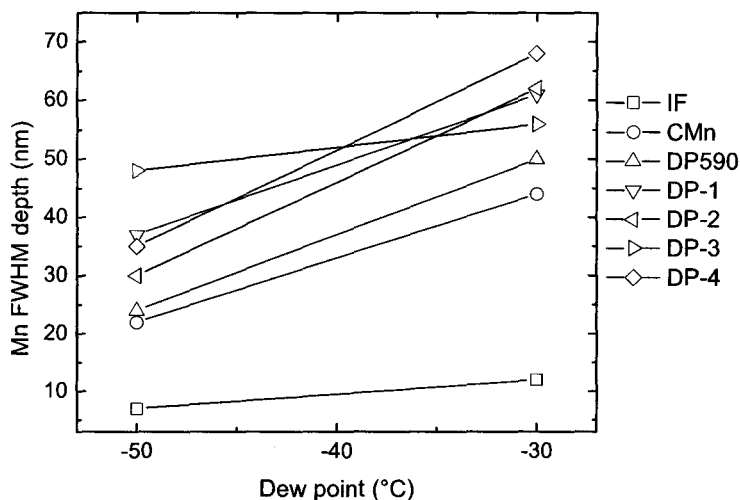


Figure 5.14: Change in oxide thickness from -50°C to -30°C dew point.

- The oxide thickness is minimal and tended to increase with Mn content.
2. At the industrially common pO_2 (-30°C dew point):
 - Oxidation remained external, but the thickness of the oxide increased significantly (figure 5.14) for all alloys.
 3. Using the intermediately high pO_2 (-10°C dew point):
 - The thickness of the external oxide was similar to that observed at the -30°C dew point.
 - The increase was not as significant as from -50°C to -30°C.
 4. At the highest pO_2 (+5°C dew point):
 - Both O and Mn enrichment continued to greater depths
 - Transition from external to internal oxidation

Although it is not obvious from the XPS curves at the +5°C dew point, the appearance of the surface after annealing allows one to conclude that the mode

of oxidation was different. After processing with the lower dew points, the surface appeared to be a 'tan' or 'straw' colour caused by a layer of MnO on the external surface. At the highest dew point (+5°C), the surface took on a more metallic luster, similar to the IF steel which has been shown to have less Mn and more Fe at the surface.

5.4 In-Situ Reduction of MnO

Separate and distinct observations were obtained regarding the samples with MnO deposited on the surface after being dipped in either a pure Zn bath or the galvanizing bath as described in §4.2.2.

5.4.1 Reaction with Pure Zn Bath

The interfacial microstructure observed for the samples dipped in pure Zn is found in figure 5.15 and was invariant with respect to reaction time. Contained within the reaction layer are three distinct regions. Immediately adjacent to the substrate is a discontinuous layer containing voids/pores where the original oxide film was deposited. Moving away from the substrate, the layer adjacent to the voids was composed of intermetallic compounds (IMCs) which are expected from the reaction between Zn and Fe (Tang 1989). Finally, the Zn overlay is found at the outer surface. Since IMCs were found at the interface and the oxide layer was no longer continuous, a process (either physical or chemical) must have removed the oxide.

Following immersion for 60s in the Zn bath, figure 5.15 shows a significant amount of voids/pores present at the steel/Zn interface. The discontinuity of this layer is likely due to the fact that the deposition technique employed did not produce a fully dense

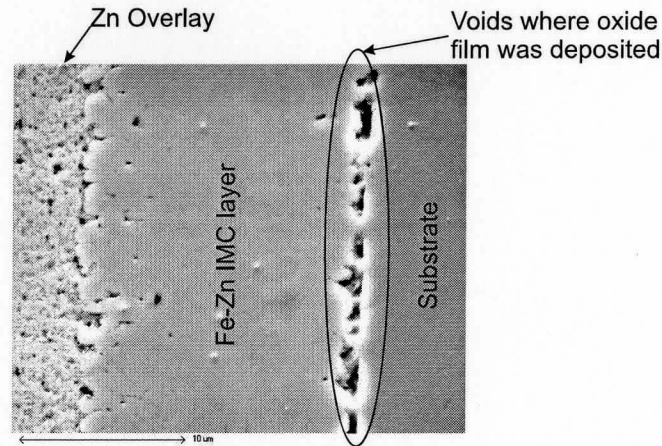


Figure 5.15: SEM photomicrograph of sample dipped in Zn for 60s showing the presence of oxides at the steel/Zn interface and formation of Fe-Zn IMCs. Labels correspond to regions found after both 20s and 60s reaction time.

oxide (Wei et al. 2007), and liquid metal penetration is probable. Consequently, a discontinuous oxide film remains at the steel/Zn interface after immersion.

Using the Zn and Fe signals to identify the steel/Zn interface allowed other elemental signals to be identified on a micrograph. Examining figure 5.16, it can be seen that the only detectable Mn was not found at the steel/Zn interface but at the IMC/overlay interface. This is the case for both 20s and 60s immersion times, the only difference being the thickness of the IMC layer. After 20s, the layer was approximately $10\mu\text{m}$ thick, while after 60s it was approximately $20\mu\text{m}$.

The observed interfacial structure can be explained with the following mechanism. Upon reaching the steel surface after penetrating the MnO film, the Zn reacted to form Fe-Zn IMCs and their rapid growth physically displaced the oxide. This mechanism is similar to that postulated by Jordan and Marder (1998) who used an Fe-oxide as a simulated inhibition layer (diffusion barrier) in a pure Zn bath. They found that the liquid Zn eventually penetrated the oxide and reached the steel surface to form the observed Fe-Zn IMCs. The growth of these Fe-Zn IMCs subsequently fractured the oxide layer and was then incorporated into the coating (figure 5.17).

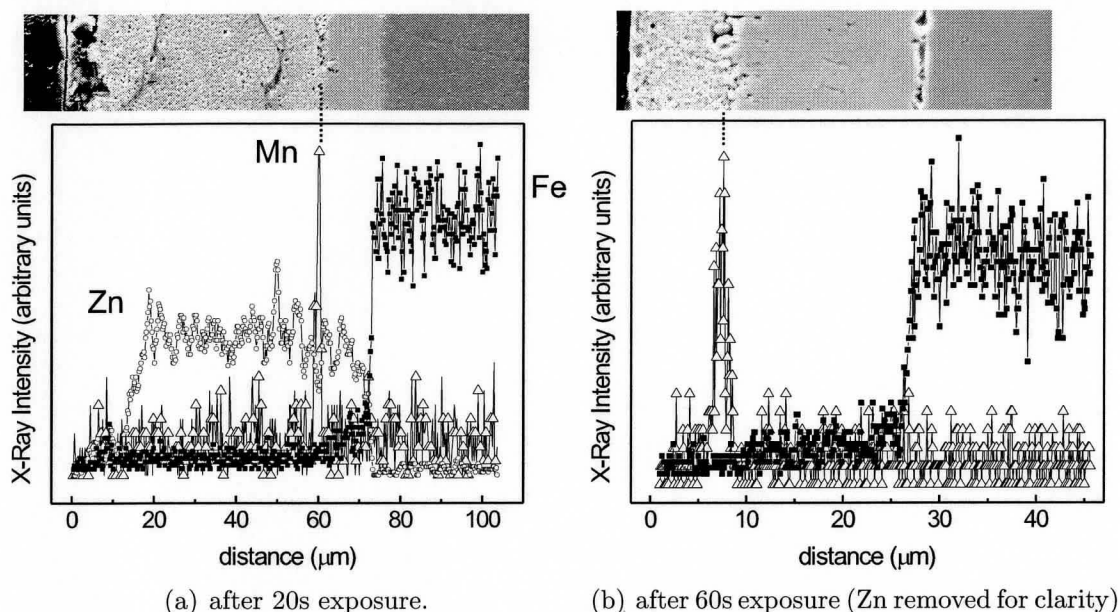


Figure 5.16: EDX line scan through interface of sample dipped in Zn bath. Illustrates physical removal of MnO film from steel surface to IMC/overlay interface. (PHILIPS)

Although voids/pores likely left by the oxide film were observed in the secondary electron images, Mn was not detected at the steel/Zn interface. Two reasons exist to explain this phenomenon. First, the oxide particles were likely pulled out during polishing resulting in no detectable Mn at the surface. Second, since Fe and Mn are electronically similar, their x-ray peaks overlap and when Fe is detected it relates to the substrate and creates a much greater signal than Mn. The lack of evidence of MnO at the steel/coating interface makes this work inconclusive regarding the mechanism of removal/reduction with pure Zn. The above observations do show, however, that the growth of Fe-Zn IMCs can physically displace a film of MnO which was quite thick compared to one which would be observed after annealing.

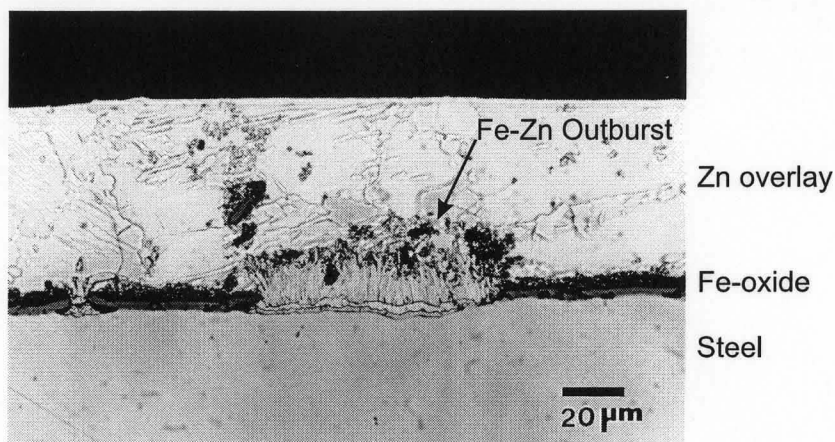


Figure 5.17: Micrograph of Fe-Zn outburst in a sample prepared with a thick Fe-oxide to act as a diffusion barrier for Zn. The oxide was displaced and incorporated into coating. From Jordan and Marder (1998).

5.4.2 Reaction with Zn-0.2wt%Al (Zn-Al) Bath

After 5s immersion time in the galvanizing bath, only trace amounts of the bath alloy had adhered to the steel due to the oxide present on the surface as shown in figure 5.18a), with the coating only partially adhering to the surface. An EDX line scan through a section of the coating in contact with the substrate shows an enrichment of Mn throughout the coating. This coating, as shown in figure 5.18b) was $\sim 3\mu\text{m}$ - much thicker than the original oxide.

Using the same technique on an area without any adhered Zn, it can be seen that a reaction had still occurred with the oxide (figure 5.19). Whereas the original thickness was approximately 700nm, it was observed that it had been reduced to approximately 400nm after 5s immersion in the galvanizing bath. Furthermore, the oxide was slightly enriched with Zn - likely due to the porous nature of the deposited film.

These two distinct observations offer a measure of what is occurring at early times when MnO is exposed to Al in the bath. At first, the Al is reducing the thickness of the oxide and the Mn is dissolving in the bath alloy.

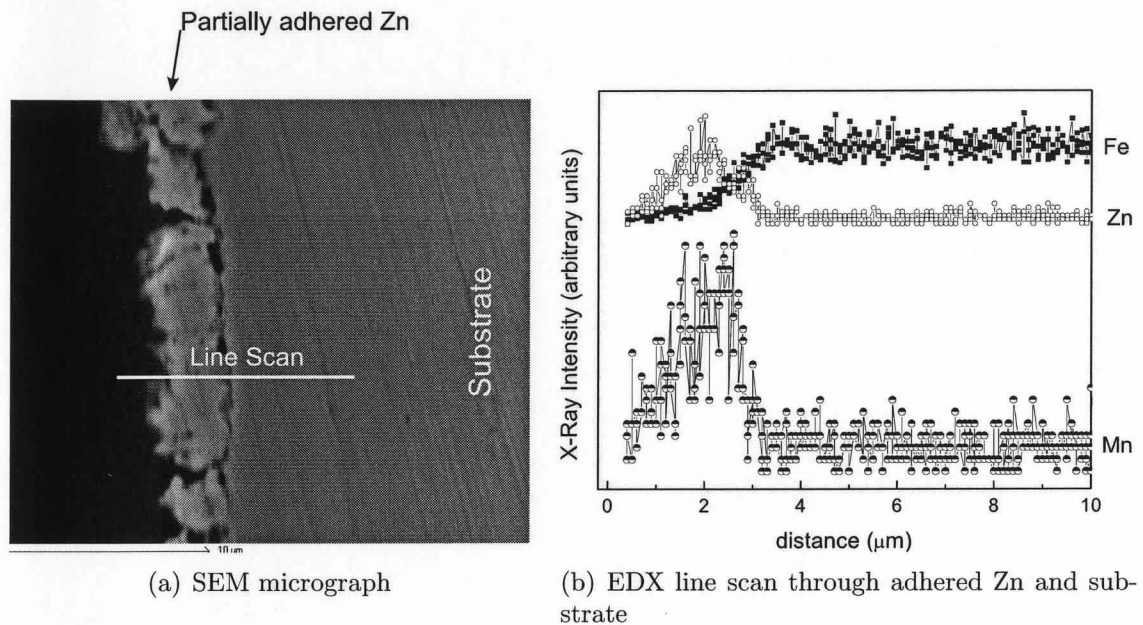


Figure 5.18: Sample after immersion in Zn-Al bath for 5s showing discontinuous coating containing dissolved Mn as well as remaining oxide.

For samples immersed for more than 5s, the interfacial microstructure for the Zn-Al dipped samples was significantly different from the pure Zn dipped samples. In this case, residual oxides cannot be seen and there was no distinct IMC layer. An EDX line scan shows a significantly different distribution of alloying elements through the interface. Figure 5.20 indicates that after both 10s and 20s, there was significant segregation of Al to the steel/coating interface. This accumulation of Al can be attributed to the formation of an Fe-Al rich interfacial layer after MnO reduction since there was not any Mn or O detected.

Adhesion of the bath alloy without the formation of Fe-Zn IMCs, and the lack of oxides at the interface after both 10s and 20s indicates that when Al is added to the bath, a different mechanism is operative. Moreover, since the sample immersed for only 5s showed a significant decrease in the oxide thickness and dissolution of

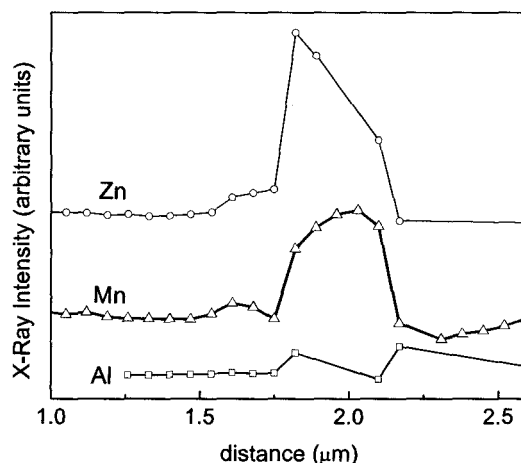


Figure 5.19: EDX line scan across external surface for sample dipped in Zn-Al bath for 5s showing remaining MnO.

Mn into the coating, the process of aluminothermic reduction was occurring and was time-dependant - requiring transport of Al to the steel surface.

5.5 Reactive Wetting Measurements

Each wetting curve contains common features with two distinguishable stages. First, immediately after immersion, F_{measured} abruptly decreases. This is indicative of contributions from F_{buoyancy} and F_{wetting} when $\theta \gg 90^\circ$ while the sample is moving to the final immersion depth. After F_{measured} reaches a minimum, it increases and is representative of the reactive wetting process since F_{buoyancy} and F_{gravity} are constant. Data from measurements before the minimum is achieved is not representative of any process of interest, and all data analysis was performed at or beyond this point. A typical wetting curve for an IF sample annealed at a dew point of -30°C is shown in figure 5.21. It shows a rapid change of F_{measured} with time due to the change in contact angle - which is indicative of reactive wetting. The minimum in F_{measured} for this sample was achieved approximately 1s after the sample touched the surface.

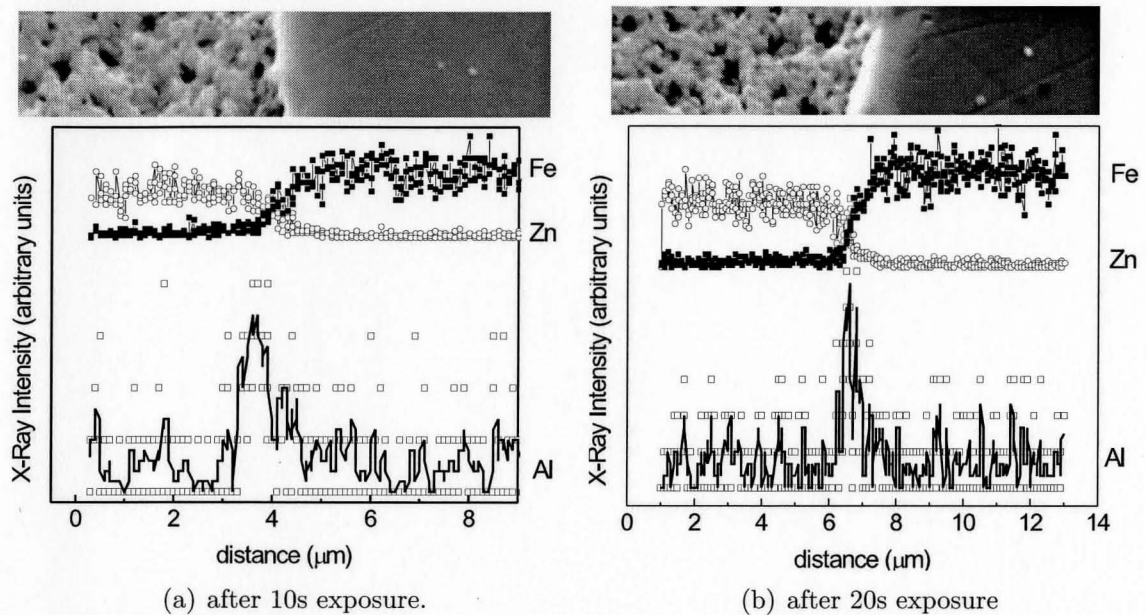


Figure 5.20: EDX line scan through interface of sample dipped in Zn-Al bath. There was no appreciable Mn increase at the interface.

With knowledge of the properties of bath alloy (ρ_{bath} and γ_{LV}), θ can be explicitly calculated by re-arranging equation 4.2 such that:

$$\theta = \cos^{-1} \left(\frac{F_{\text{measured}} - mg + V_{\text{displaced}} \rho g}{P \gamma_{\text{LV}}} \right) \quad (5.1)$$

Although ρ_{bath} is easily determined, determination of γ_{LV} is more difficult and values cannot be readily found in the literature for dilute Zn-Al-Fe alloys. Therefore, a different course has to be taken to analyze the data. Re-arranging equation 4.2 yields a geometry independent wetting term which includes θ and γ_{LV} (equation 5.2).

$$\frac{F_{\text{measured}} - mg + V_{\text{displaced}} \rho_{\text{bath}} g}{P} = \gamma_{\text{LV}} \cos \theta \quad [\text{N.m}^{-1}] \quad (5.2)$$

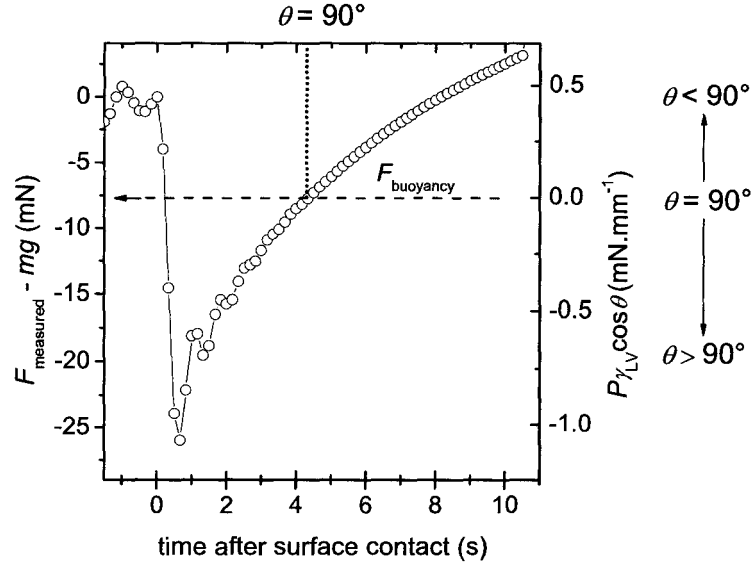


Figure 5.21: Wetting curve for IF sample annealed at -30°C dew point showing transition from obtuse to acute contact angle.

Using this result, a limiting case when $\theta=90^{\circ}$ can be considered such that the right hand side of equation 5.2 is equal to zero since $\cos(90^{\circ})=0$. This is equivalent to:

$$\begin{aligned}
 F_{\text{measured}} - mg &= -V_{\text{displaced}}\rho_{\text{bath}}g + P\gamma_{\text{LV}}\underbrace{\cos\theta}_0 \\
 &= -F_{\text{buoyancy}}
 \end{aligned}
 \tag{5.3}$$

Using equation 5.3 with $\rho_{\text{bath}}=6.5\text{g}\cdot\text{cm}^{-3}$ (Liu 2006), it is seen that for the curve in figure 5.21, the initial contact angle was larger than 90° , reached 90° at approximately 4s, and continues to decrease with increasing time. Confirmation of these calculations was conducted by measuring the height of the wetted surface on a sample after the experiment. Since in this case the final value of θ was acute, the wetted height should, and did, exceed the immersion depth.

The effect of dew point ($p\text{O}_2$) on the wetting curves for high Mn alloys was significant. There are two distinct regimes which can be identified in figure 5.22: the

curves for mid-range dew points (-30°C & -10°C), and for the extreme dew points (-50°C & $+5^{\circ}\text{C}$). Having a consistently negative wetting force for the mid-range dew point samples indicates that the contact angle was considerably larger than 90° for all reaction times. Conversely, the extreme dew-points exhibited a decreased, but still consistently negative, wetting force ($\theta > 90^{\circ}$). Unlike the IF sample in figure 5.21, the forces in figure 5.22 always exceeded F_{buoyancy} , caused by an obtuse contact angle (equation 5.3).

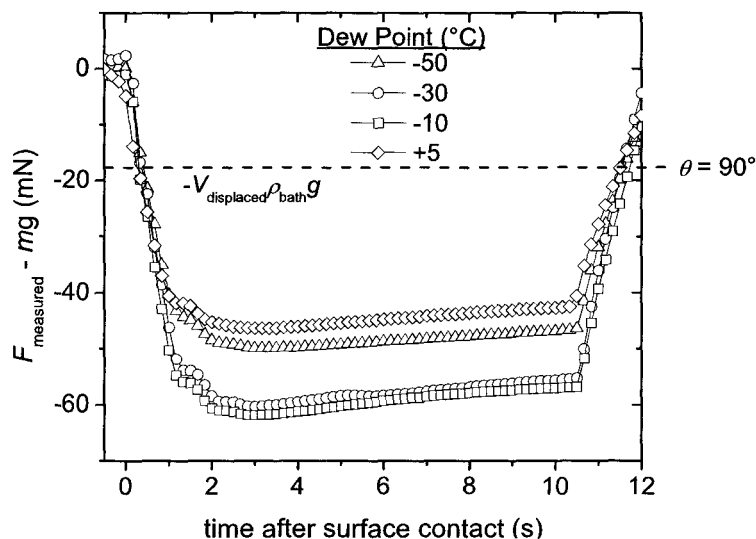


Figure 5.22: Effect of annealing dew point on wetting curve for DP-3 alloy.

The trend between alloys for -50°C and -30°C dew points was that for a fixed dew point, the wetting force was more negative with increasing Mn content and remained that way throughout the experiment. Figure 5.23 shows the significant differences between the wetting curves obtained for the IF sample (0.14wt% Mn) and the higher Mn alloys. A positive slope was observed in all cases after a minimum in F_{measured} was achieved, indicating the forward progression of the reaction through a decrease of the contact angle. To enhance clarity, only curves for four alloys are shown. Those which are not shown lie between the others according to their alloy content.

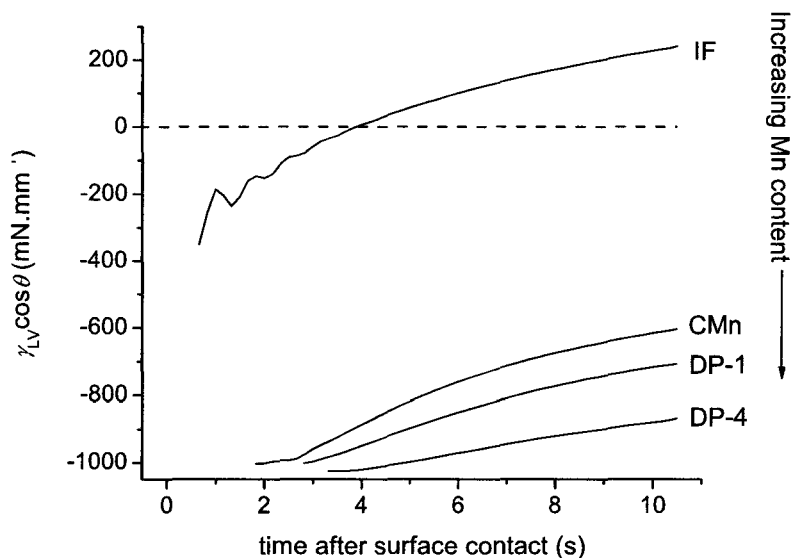


Figure 5.23: Variation of the wetting force for various samples annealed in -30°C dew point atmosphere.

The metric chosen to compare the effect of alloy Mn content and annealing atmosphere on reactive wetting was the wetting force at the earliest representative moment. This time coincides with F_{measured} reaching a minimum. By choosing this time, reactions occurring soon after immersion are represented. Several other reasons exist for choosing a single point in time for analysis, and a rigorous explanation behind this choice is found in Appendix B. Hereafter, the term wetting force will refer to the quantity ' $\gamma_{\text{LV}}\cos\theta$ ' taken at the point when the minimum force was measured or the wetting force per unit perimeter.

As seen in figure 5.24, the initial wetting force offers a reasonable measure of the progression of wetting and allows observations and conclusions to be drawn about the wetting behaviour in the same way that they would be with the complete wetting curve from which this value is derived. Both figures 5.23 and 5.24 indicate that the IF steel reacts more rapidly with a decreased, but still negative, initial wetting force. Moreover, since the wetting curves did not tend to cross, evaluation at any point

in time would show similar trends, but the absolute magnitude of the measurement would not necessarily show the same variations during initial reaction with the bath.

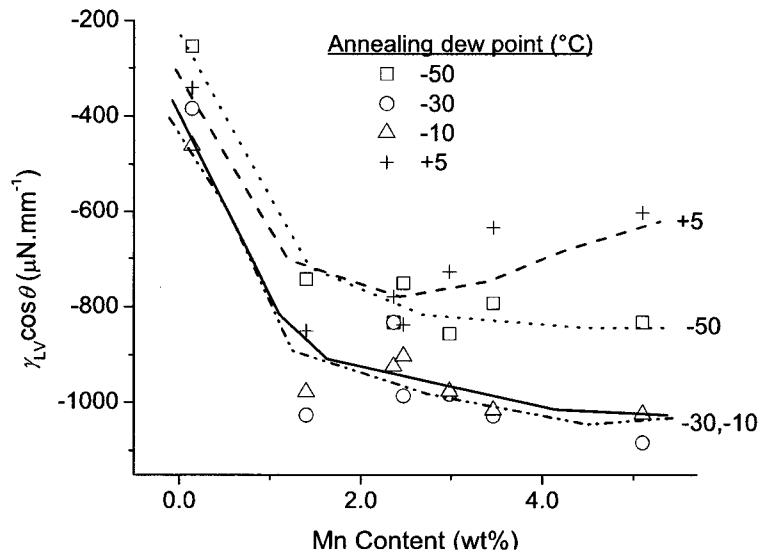


Figure 5.24: Effect of Mn content on initial wetting force for various dew points.

Figure 5.25 shows the results of this method of analysis vs. dew point, while figure 5.26 shows the same data vs. $p\text{O}_2$ of the annealing atmosphere, which is different for each alloy due to the variations in the PAT (table 4.2). Although each vary in magnitude, all alloys showed a similar 'U'-shaped trend. These figures indicate that at the lowest dew point (and consequently lowest $p\text{O}_2$), the contact angle is the smallest, or wetting has progressed the furthest at the time of the measurement. As the dew point was increased to the intermediate dew points (-30°C and -10°C), wetting had not progressed as far, as indicated by the increased magnitude of $\gamma_{LV}\cos\theta$. Finally at the highest dew point ($+5^\circ\text{C}$), the system has again reached approximately the same degree of wetting as it had at the lowest dew point. It should be noted that the y-axis scale in figures 5.25(a) and 5.26(a) are different from the rest due to the large difference in initial wetting force between the IF steel and the other alloys.

Several summary observations can be made from the wetting curves and figures 5.25 & 5.26 regarding the reactive wetting behaviour:

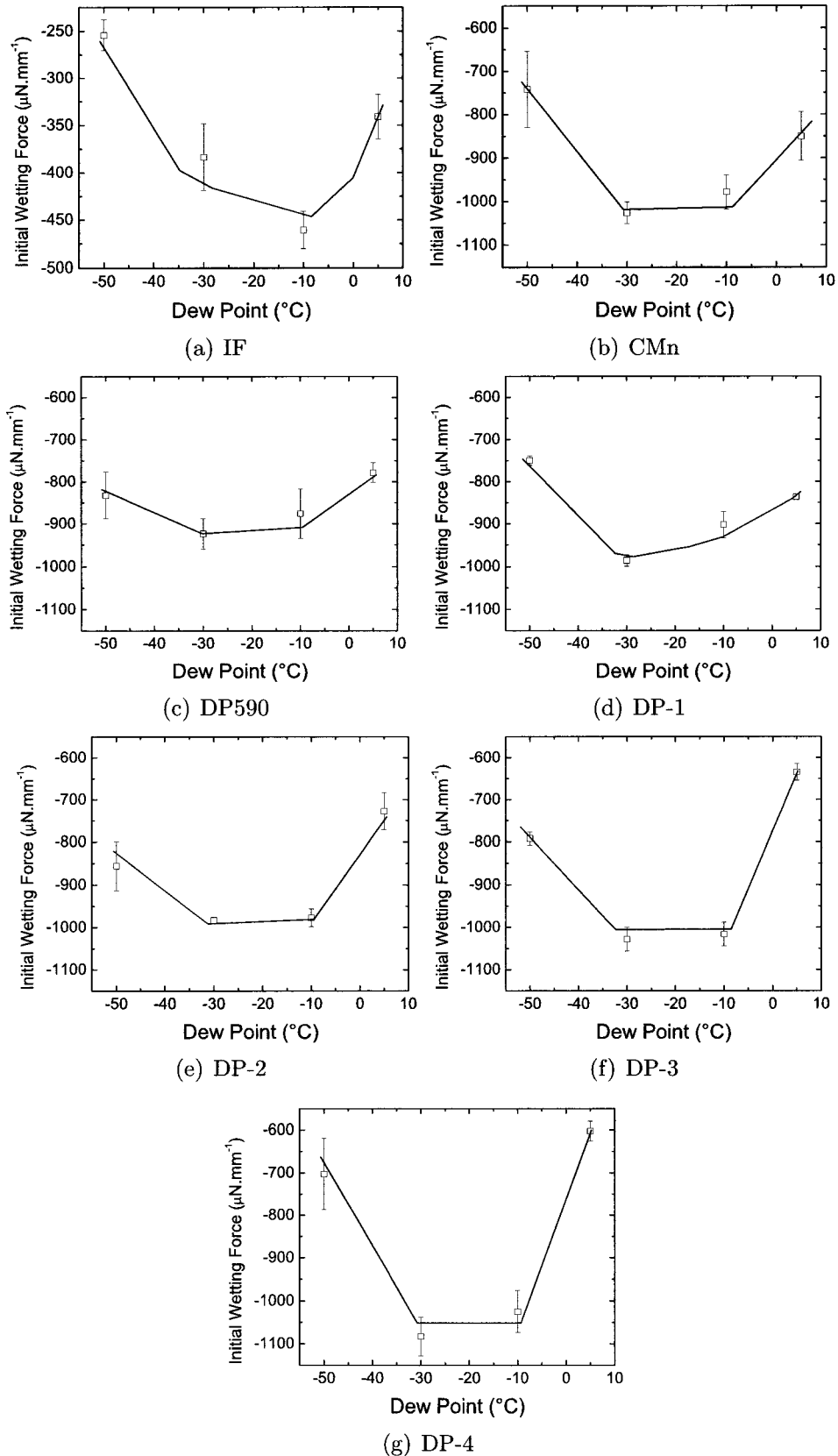


Figure 5.25: Initial wetting force vs. dew point during annealing. Note: different y-axis range for IF sample.

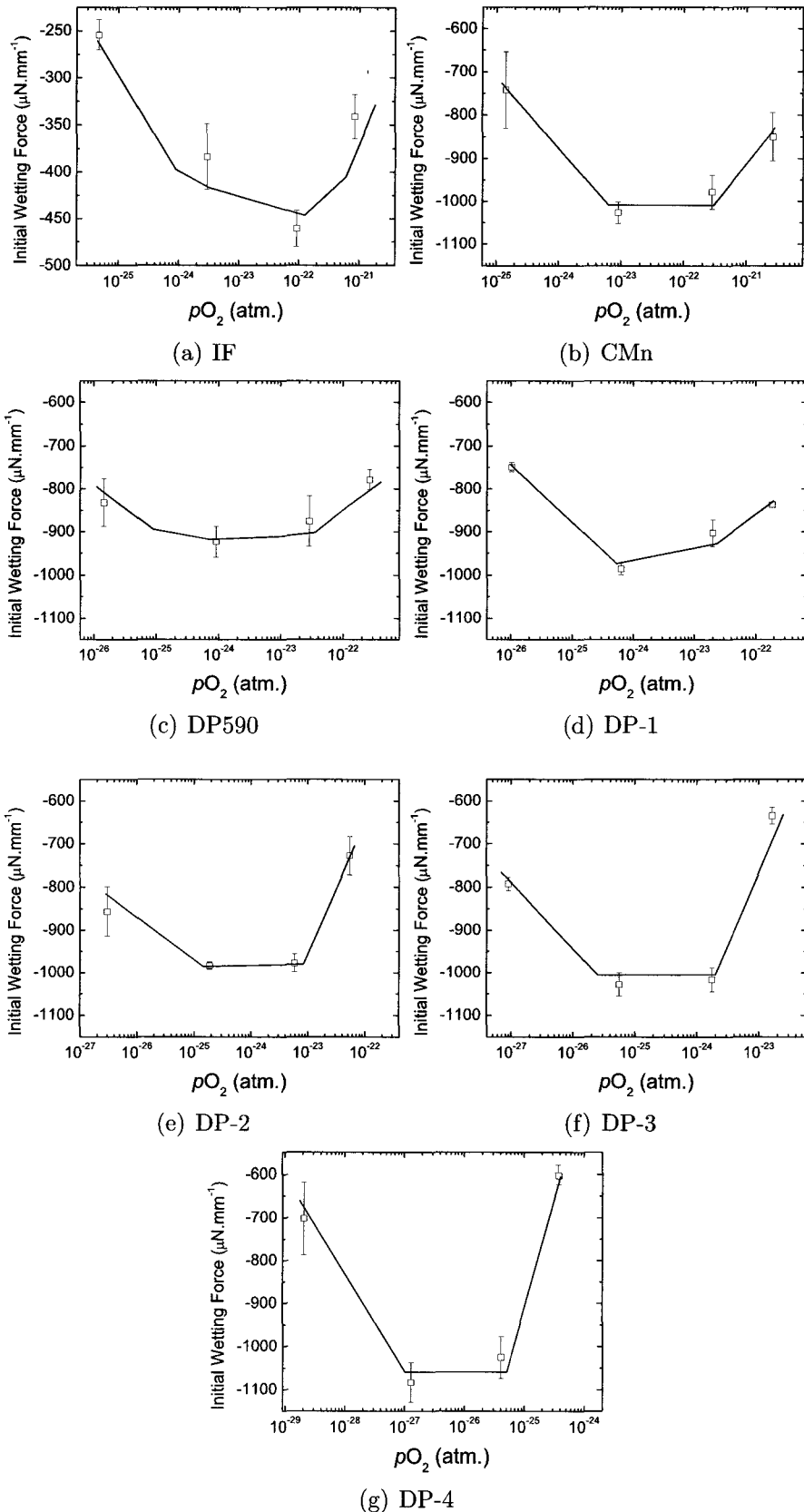


Figure 5.26: Initial wetting force vs. $p\text{O}_2$ during annealing. Note: different x-axis for all samples due to different $p\text{O}_2$ due to different PAT, and different y-axis range for IF sample.

1. In all cases the initial wetting force was negative, but with varying magnitudes as a function of the dew point. This is indicative of an obtuse initial contact angle ($\theta > 90^\circ$).
2. The gradient of all curves was positive after reaching a minimum, irrespective of the Mn content or annealing atmosphere (as shown in figures 5.22 and 5.23). Thus, reactive wetting progressed after this point in all cases.
3. The IF steel exhibited the best wetting at all dew points. Moreover, at every dew point explored, the wetting force for the IF steel exceeded any other steel at any dew point (figure 5.24).

The error bars shown in figures 5.25 and 5.26 represent the standard deviation of repeated measurements (between 5 and 10 for each annealing atmosphere and alloy).

Steel/coating interfacial reaction products also varied with Mn content. Figure 5.27a) and b) show how the IF and CMn alloy had a well developed and continuous layer of Fe_2Al_5 crystals. With increasing alloy Mn content, DP-1 processed under the same conditions exhibited a discontinuous layer of Fe_2Al_5 with some Fe-Zn IMC crystals on the surface (figure 5.27c)). Increasing the Mn content to 3.0wt% and 3.5wt%, with DP-2 and DP-3 respectively, increased quantities of Fe-Zn IMCs on the surface (figure 5.27d) and e)). This phase is likely $\zeta\text{-FeZn}_{13}$, as observed by others (Baril and L'Esperance 1999). It should be noted that the appearance of Fe-Zn IMCs as shown in figures 5.27c), d) and e) are representative of baths containing less than 0.14wt% dissolved Al (Guttman 1994). Subsequently, this is evidence that the local dissolved bath Al was being reduced during an experiment with the higher Mn steels.

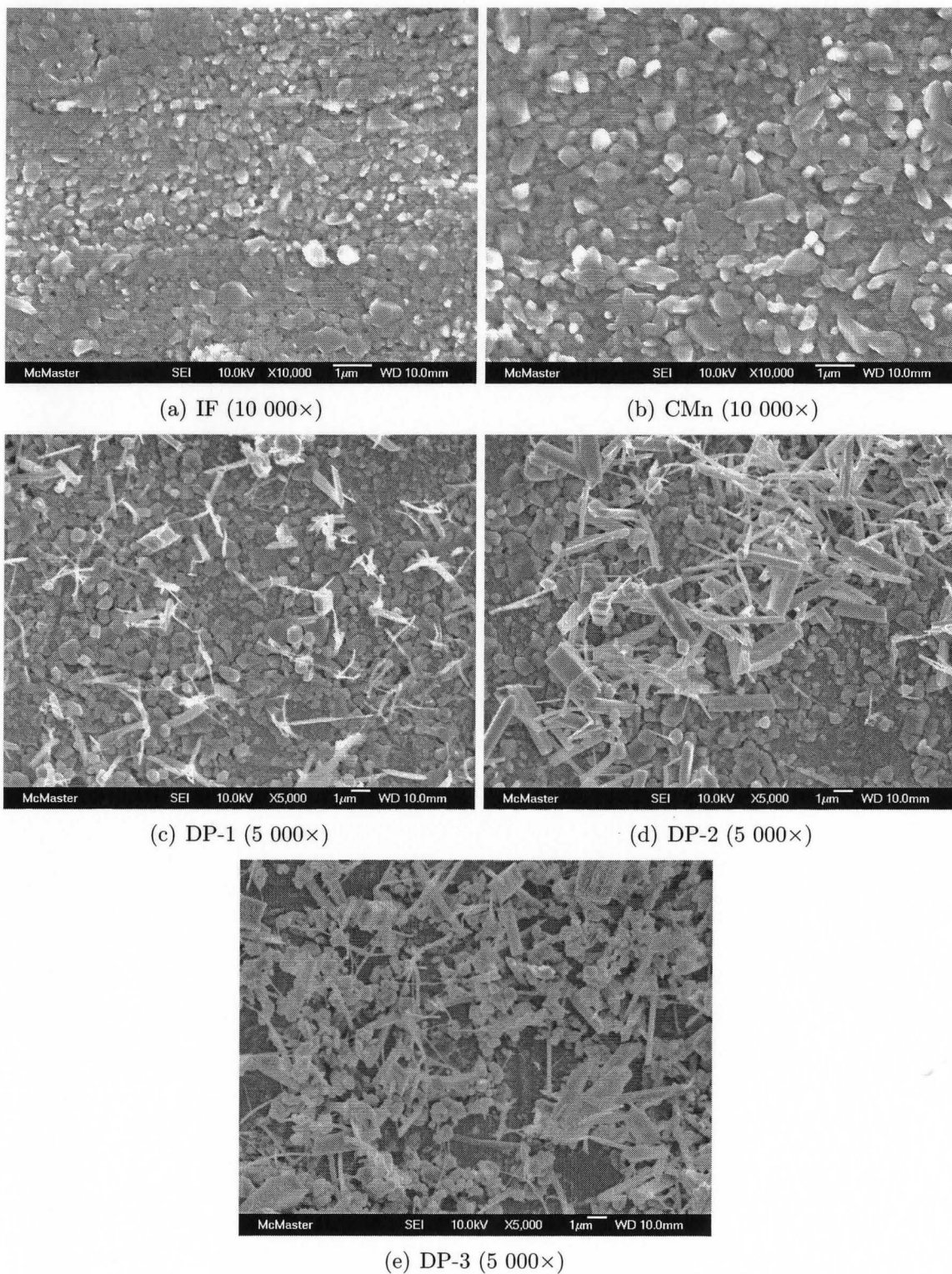


Figure 5.27: Impact of Mn content on steel/coating interfacial structures observed after dipping samples annealed at -30°C dew point. Zn was dissolved with $\text{H}_2\text{O}/10\%\text{H}_2\text{SO}_4$.

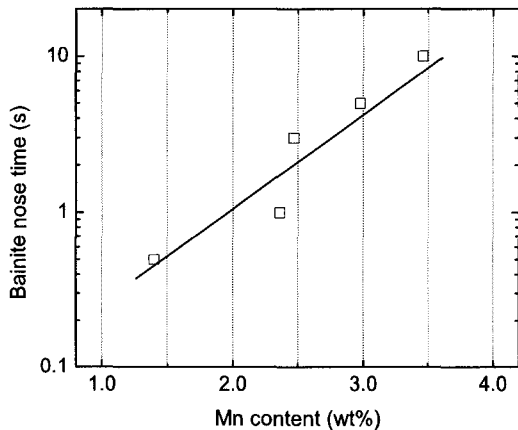
Chapter 6

Discussion

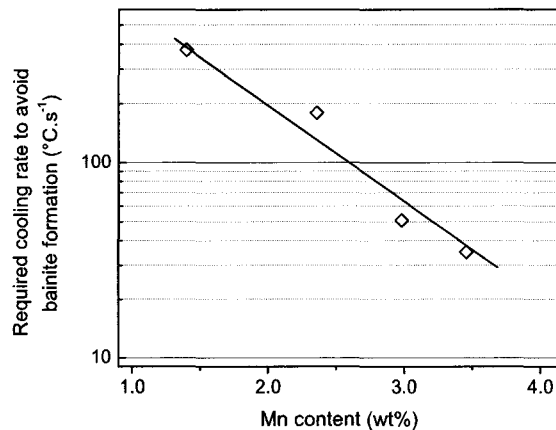
6.1 Increasing Hardenability with Mn Additions

Two common metrics are used for quantifying hardenability. First is the location of the bainite nose. The magnitude with which Mn affected this parameter was shown in figure 5.4. By shifting this curve towards lower cooling rates, it becomes ‘easier’ to avoid bainite formation and form the desired $\alpha + \alpha_M$ microstructure. Figure 6.1a) summarizes the time at which the bainite nose was observed during continuous cooling. To obtain a complete picture of the effect of Mn on bainite formation during cooling, the time to the bainite nose must be combined with the temperature and include the annealing temperature to calculate the required cooling rate. Since Mn decreases the intercritical annealing temperature (figure 4.5) and increases the time to the bainite nose, the decrease in critical cooling rate with increasing alloy Mn content is large and is shown in figure 6.1b). The result encompasses orders of magnitude difference between the alloys - from $\sim 350^\circ\text{C}\cdot\text{s}^{-1}$ for the CMn (1.40wt% Mn) alloy to $\sim 35^\circ\text{C}\cdot\text{s}^{-1}$ for the DP-3 (3.46wt% Mn) alloy. A value could not be calculated for DP-4 since it exhibited no transformation to bainite at the cooling rates explored.

Lowering the M_S is the other parameter which is related to hardenability. Its variation with Mn content is shown in figure 6.2. These values correspond well with the study by Zhao (1992) as given by the dashed line. When this value is below $\sim 460^\circ\text{C}$,



(a) Variation in bainite 'nose' position vs. Mn content during continuous cooling.



(b) Cooling rate required to avoid bainite transformation when intercritical annealing temperature is considered.

Figure 6.1: Contribution of Mn to delay of bainite formation during cooling.

it ensures that α_M does not form until after galvanizing – preventing tempering which could otherwise occur during dipping in the 460°C bath.

The mechanism which is attributed to the improvement in hardenability with increasing Mn content is mainly related to solubility of C in γ (Tanaka et al. 1979). As shown in figure 6.3, both C and Mn partition appreciably to γ during intercritical annealing. Subsequently when cooling, Mn and C are rejected from α into γ , further stabilizing it until the composition/temperature reaches a point that the transformation to α_M occurs. This enrichment with Mn and C also decreases the cooling rate required for this transformation to occur and subsequently allows more Mn and C to diffuse during cooling - compounding the effect of Mn and C partitioning. This mechanism explains why both the critical cooling rate was reduced (figure 6.1) and the observed decrease of the M_S temperature with increasing Mn content (figure 6.2).

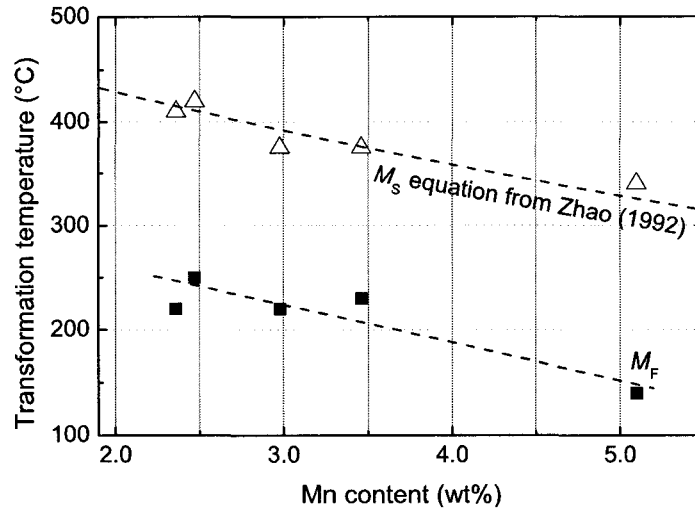


Figure 6.2: Experimentally determined transformations temperatures during cooling with M_S equation from Zhao (1992).

6.2 Oxidation Growth Modes During Annealing

Although not entirely clear from the depth profiles in figures 5.8 - 5.13, by measuring the depth at which the Mn concentration has reached one-half of the maximum enrichment or the full-width at half-maximum (FWHM), a more obvious relationship can be seen. Figure 6.4 shows this relationship for all the alloys where a clear transition from internal to external oxidation is observed between the -10°C and $+5^\circ\text{C}$ dew point atmospheres despite the fact that there was not a definite second peak in the Mn profiles from figure 5.8 - 5.13. Both the -30°C and -10°C dew point atmospheres yield similar results, and thus it can be presumed that the limitation in this range of $p\text{O}_2$ arises not from the transport of O_2 to the surface, but from Mn diffusion in the alloy and oxide.

Increasing the dew point to $+5^\circ\text{C}$ caused a significant increase in the FWHM Mn depth due to the promotion of internal oxidation. This is caused by the flux of oxygen into the alloy greatly exceeding the flux of the oxidizing species (Swisher 1970); in this case Mn. Calculation of the transition was originally formalized by Wagner (1959)

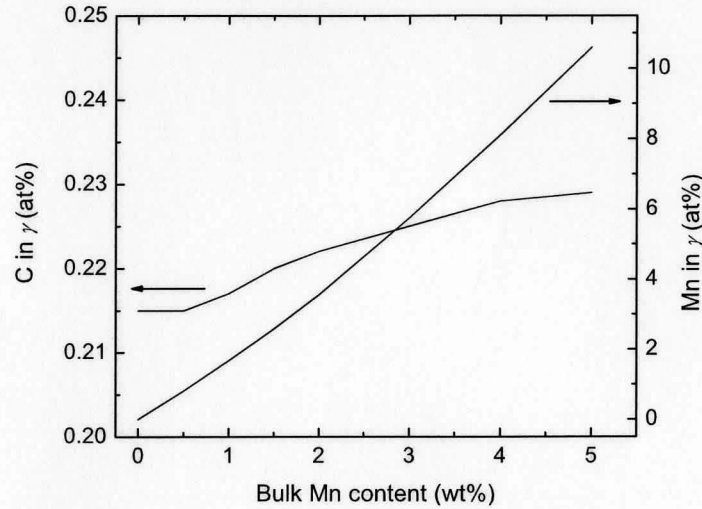


Figure 6.3: Partitioning of C and Mn to γ during annealing at a temperature to produce 30% γ +70% α with 0.07wt% C. Calculated with Thermo-Calc[®] and the TCS steel database v.2.

with an explicit calculation of the critical molar fraction of oxidizable solute (A) required to observe external oxidation to AO_ν :

$$N_{A,\text{crit}}^o = \left[\frac{\pi g^* V_{\text{alloy}} N_{\text{O}}^s D_{\text{O}}}{2\nu V_{\text{AO}_\nu} D_{\text{A}}} \right]^{\frac{1}{2}} \quad (6.1)$$

where g^* is the critical volume fraction of oxide particles needed to block the inward diffusion of oxygen, N_{O}^s is the mole fraction of oxygen dissolved at the surface, D_{O} is the diffusivity of oxygen in the alloy, D_{A} is the diffusivity of A in the alloy, V_{AO_ν} is the molar volume of the oxide (AO_ν) and V_{alloy} is the molar volume of the alloy. N_{O}^s is proportional to $p\text{O}_2$, and therefore as the dew point is increased, $N_{A,\text{crit}}^o$ also increased. Another way to consider this is by fixing the solute content and calculating the critical N_{O}^s required to shift to internal oxidation:

$$N_{\text{O}}^s \geq (N_{\text{A}}^o)^2 \left[\frac{2\nu V_{\text{AO}_\nu} D_{\text{A}}}{\pi g^* V_{\text{alloy}} D_{\text{O}}} \right] \quad (6.2)$$

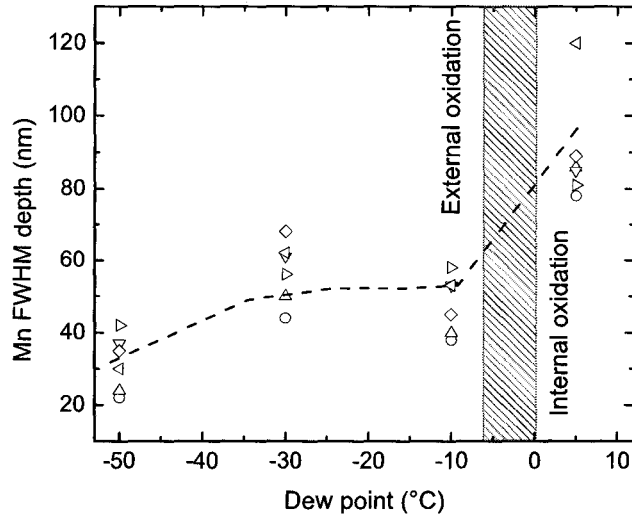


Figure 6.4: Effect of changing the dew point on the depth of Mn enrichment.

Equation 6.2 accurately portrays what is observed in figure 6.4 - at higher pO_2 , the shift to internal oxidation is observed. Calculation of critical values with equations 6.1 and 6.2 are hampered by several factors: (i) the model was developed for a binary system neglecting any interactions between elements other than the solute and oxygen in the solvent; (ii) the model was developed for single crystals and thus, the application of these models does not reflect polycrystalline alloys with short-circuit diffusion paths for oxidation, which frequently results in oxide growth at the grain boundaries prior to significant bulk oxidation (Thorning and Sridhar 2007).

6.3 Relating Surface State to Wettability

As shown in §5.4, the process of reducing a layer of MnO in a galvanizing bath is slow, particularly compared to the formation of the Fe-Al inhibition layer (Chen 2007), and this step may act as the rate-limiting step in the galvanizing process with higher Mn alloys - effectively adding an additional process step and an additional source of Al consumption. The results obtained when dipping the samples with MnO deposited

on the surface in a pure Zn bath agree with the results of Hashimoto et al. (2003) who also showed the presence of oxides at steel/Zn interface of a 1.4wt%Mn - 0.14wt%Si steel after annealing in various atmospheres and dipping in a pure Zn bath. This exemplifies the need for Al not only to form the inhibition layer, but also the secondary role of reducing residual (or in this case quite thick) oxides on the surface formed during annealing.

From the interfacial structures shown in figure 5.27, the differences between samples with varying Mn content is obvious. When the amount of Mn in the alloy is increased, the inhibition layer becomes less continuous with both exposed steel and crystals of Fe-Zn IMCs present. Since the bulk dissolved Al in the bath remained constant between these experiments and exceeded 0.14wt%, the driving force for nucleation of Fe_2Al_5 should exceed all other IMCs and it should be the only phase present on the steel surface (Guttman 1994). Subsequent analyses of the bath compositions indicated that there was no depletion of Al to account for the formation of Fe-Zn IMCs - indicating that the depletion is limited to the immediate vicinity of the sample. A decrease of the local dissolved Al would change which IMC is favoured for precipitation, as seen with the higher Mn alloys (figure 5.27). Since it was observed that the higher Mn alloys had a thicker layer of MnO on the surface after annealing, the appearance of Fe-Zn IMCs at the steel/coating interface (figure 5.27) is implicit evidence of in-situ aluminothermic reduction of MnO (equation 2.7). This local depletion is attributed to the stagnant nature of the bath in these experiments. If processed in a commercial CGL, this alloy may not have formed the observed Fe-Zn IMCs due to the rapid mixing in the bath, resulting in a continuous replenishment of Al at the steel surface. A decrease in wettability has been noted by Oren and Goodwin (2004) in other galvanizing experiments when compared to a CGL and has also been attributed to the issue of Al supply. Accordingly, this phenomenon has become more

prevalent in recent years with higher alloy grades, again due to the need for Al not only to form the inhibition layer, but to also reduce oxides on the surface.

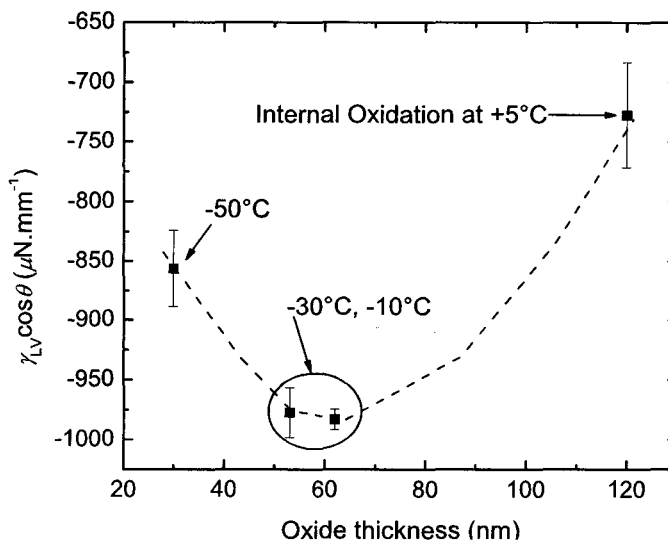


Figure 6.5: Variation of initial wetting force as a function of oxide thickness for DP-2. Transition to internal oxidation at +5°C dew point caused significant improvement in wetting.

The relationship between annealing atmosphere, oxide thickness, and wettability is more obvious when the wetting force calculated in §5.5 is plotted against oxide thickness. By doing this, figure 6.5 shows how the increase in oxide thickness caused by an increase in dew point from -50°C to -30°C and -10°C causes a significant decrease of the initial wetting force. This trend is reversed when the dew point was increased to +5°C, and this force was greatly increased - which, as shown in §6.2, can be attributed to the transition from external to internal oxidation. Moreover, figure 6.5 indicates that the reduction of the oxide on the surface acts as the rate limiting step when the oxide is relatively thin (i.e. ~100nm). The curve in figure 6.5 is representative of the curves observed for all alloys since the relationship between dew point and oxide thickness (figures 5.8 - 5.13) as well as dew point and wetting force (figure 5.25) are similar.

Since it has been shown in the literature that wetting does not occur when the steel surface is covered with oxides (Drillet et al. 2004), the wetting curves are essentially measuring how rapidly the meniscus is moving up the sample when limited by the reduction of MnO at the triple line (figure 6.6). Since this reduction process increased the consumption of dissolved Al from the bath and the bath in these experiments was stagnant, measurements at early times before Al was consumed from the region around the sample are the most representative. Therefore, the initial wetting force offers the most, and possibly only, viable data from the wetting curves which can be related to the *continuous* process. It allows one to infer how much of the reaction has occurred after a specific increment of time has passed, and therefore acts as a kinetic measurement.

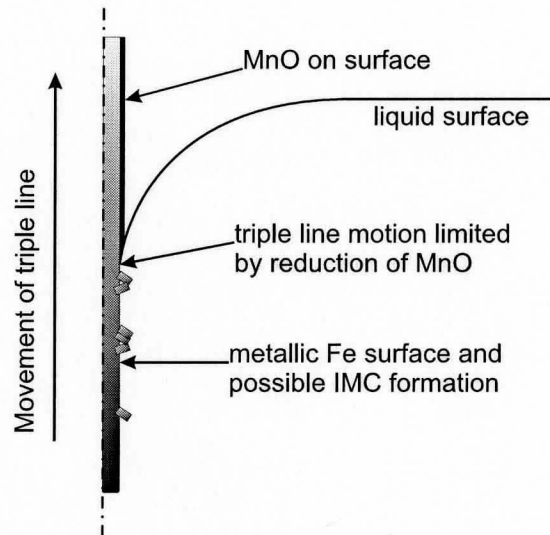
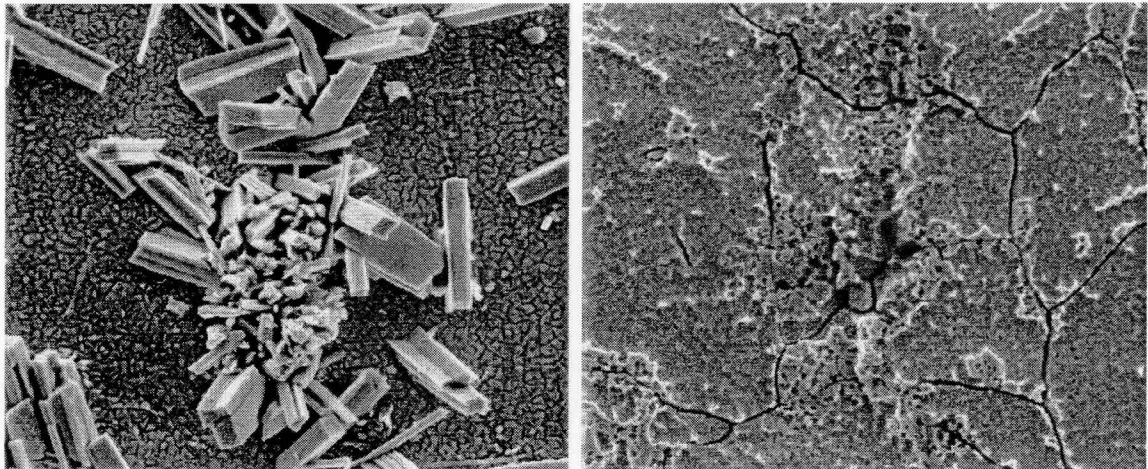


Figure 6.6: Limitation of triple line motion by reduction of MnO during reactive wetting.

The explanation of the effect of internal oxidation on wettability agrees with the observation of Bode et al. (2004) concerning the effect of Mn enrichment on wettability. Using this technique in a CGL would not be difficult as a method similar to the experiments conducted (saturation of the process gas with water) could be employed. Moreover, if the choice has to be made between using a low dew point to

limit external oxidation with a low pO_2 or promoting internal oxidation with a high pO_2 , it is quite likely that using a 'wet' gas would be more practical.

As calculated in Khondker et al. (2007), through the process of aluminothermic reduction, it is thermodynamically possible to reduce any amount of MnO, as long as a constant supply of Al is available (i.e. infinite mixing in the liquid) and sufficient time is available. Although this is reasonable in a CGL, experiments show different results. Grain boundaries, acting as short-circuit diffusion paths result in increased oxidation in these areas (Thorning and Sridhar 2007). Once reduction of the MnO film is complete (faster within the grains due to less oxidation), precipitation of Fe_2Al_5 would begin within the grain. At this point, there would be two competing processes consuming Al from the bath. The first is the continued reduction of MnO toward the grain boundaries, and the second is the coarsening and eventual breakdown of the inhibition layer within the grains. The thicker oxide at the grain boundaries would cause an increased consumption of Al and create a depletion of Al in those regions - enough to cause preferential precipitation of Fe-Zn IMCs rather than the inhibition layer at these sites. This is the situation observed by many authors (Guttman 1994; Guttman et al. 1995; Baril and L'Esperance 1999) and shown in figure 6.7 for galvanizing experiments. Perhaps if there was mixing of the liquid during these experiments to emulate a CGL, different results would be obtained - but this is yet to be proven.



(a) after removal of overlay and Al containing IMCs

(b) after removal of all IMCs

Figure 6.7: Correspondence between steel grain boundaries and outbursts. From Baril and L'Esperance (1999).

Chapter 7

Conclusions

A method to measure the wettability of Mn-containing steels with MnO layers evolved during intercritical annealing has been described and demonstrated. By utilizing a modified Rhesca® Force Balance Simulator, the motion of the galvanizing bath meniscus on the sample was evaluated as a function of alloy chemistry and pO_2 during annealing. It was shown that:

1. MnO on the surface of these steels greatly reduced the wettability with a galvanizing bath (Zn-0.2wt%Al, Fe-saturated)
2. The strong dependence of reactive wetting on the surface state evolved during annealing was attributed to the process which occurred before the formation of the inhibition layer. This was the reduction of MnO with Al in the bath which, subsequently, allowed reactive wetting to proceed.
3. By varying the pO_2 in a $N_2/5\%H_2$ gas during annealing, the wettability could also be varied. The use of a very high pO_2 (+5°C dew point) or very low pO_2 (-50°C dew point) greatly improved the ability of all alloys to be reactively wet over a conventional -30°C dew point atmosphere. This was due to a change in the amount of external oxidation during annealing. A low pO_2 produced a thin external oxide, while a high pO_2 resulted in internal oxidation which, since it wasn't in contact with the bath, did not adversely affect reactive wetting.

4. The additional step of aluminothermic reduction acts as the rate-limiting step with a relatively thin layer ($\sim 100\text{nm}$), and is required to produce a metallic Fe surface, allowing dissolution of Fe and formation of the inhibition layer as laid out in figure 7.1.

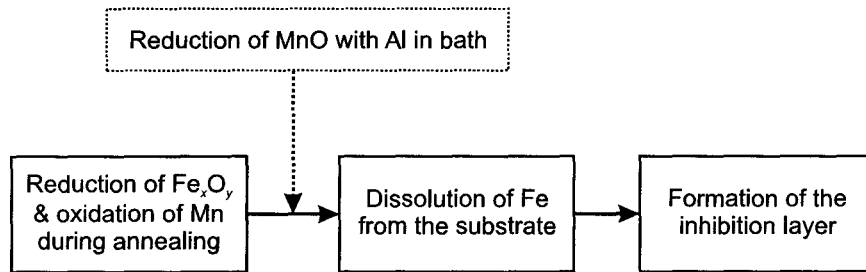


Figure 7.1: Schematic of known steps in galvanizing with the additional step of aluminothermic reduction of MnO during immersion in the Zn-Al-Fe bath.

5. Although specific values of the contact angle could not be inferred by the wetting force measurements, it was shown that $\theta > 90^\circ$ does not have the same implications as it does in non-reactive systems. Many alloys had a final value of θ which was obtuse but reactive wetting had occurred and there was adhesion of the coating to the surface. In future studies, the contact angle should only be used as a measure of kinetics, degree of wetting or wettability (degree of wetting per unit time), not to draw a conclusion as to whether a substrate is wettable or non-wettable since it is not solely the capillary forces which cause the liquid metal to adhere to the substrate.
6. Increasing the Mn content of DP steels offers a great advantage in that they can be annealed at lower temperatures and quite easily form α_M because of the increased hardenability Mn imparts. This needs to be weighed against the ability of a CGL to process these steels at a pO_2 which ensures that they can be successfully galvanized.

Chapter 8

Recommendations

As high-Mn alloys are still relatively un-explored, several steps are required both to continue this work and pursue other interesting facets:

1. Use the same thickness steels in the future with this technique to facilitate measurements.
2. Explore high Si steels to compare hardenability
 - Compare the galvanizability of alloys with the same improvements in hardenability with Si to the same increase in hardenability with Mn (likely different alloy contents)
3. Conduct MnO reduction experiments with mixing of the bath to simulate the industrial process where the supply of Al to the surface is more rapidly replenished.
 - This is crucial as the limitations of a stagnant bath cause a significant local depletion of Al in experiments - creating a situation which does not accurately represent the industrial process.
4. Look into deformation mechanisms in these higher Mn steels.
 - Variations in stacking fault energy may make stress-assisted, strain-induced transformations possible - improving work-hardening and ductility.

5. Measurement of γ_{LV} and ρ for common bath chemistries will allow comparison of wetting kinetics ($d\theta/dt$) between baths compositions and temperatures.
6. Austenitize the DP-3 or DP-4 alloys to produce a 100% α_M microstructure. Since $D_{Mn}^\gamma < D_{Mn}^\alpha$ and $D_O^\gamma < D_O^\alpha$, it is reasonable to presume that oxidation can also be decreased as long as the effect of decreasing diffusion rates exceeds the effect of increasing temperature on pO_2 .
 - If successful, these alloys could be candidates for galvanized, martensitic steels.

Bibliography

- Adda, Y., Ambroise, M. H., & Barbier, F. 1994, *Materials Science Forum*, 155-156, pp. 511–526.
- Aksay, I. A., Hoge, C. E., & Pask, J. A. 1974, *The Journal of Physical Chemistry*, 78, pp. 1178–1182.
- Aoki, A. 1976, *Japanese Journal of Applied Physics*, 15, pp. 305–311.
- Baril, E. & L'Esperance, G. 1999, *Metallurgical and Materials Transactions A: Physical Metallurgy and Materials Science*, 30A, pp. 681–695.
- Bernard, G. 1977, *Proceedings of the International Symposium for High-Strength, Low-Alloy Steels (Microalloying 75)*, New York, NY, pp. 552–566. Union Carbide Corp.
- Bleck, W. & Beste, D. 2004, *Proceedings of Galvatech '04*, Chicago, Il, pp. 349–360. AIST.
- Bode, R., Meurer, M., Schaumann, T. W., & Warnecke, W. 2004, *Proceedings of Galvatech '04*, Chicago, Il, pp. 107–118. AIST.
- Borzillo, A. R. & Hahn, W. C. 1969, *Transactions of the ASM*, 62, pp. 729–739.
- Chen, L. 2007. *Short Term Formation of the Inhibition During Continuous Hot-Dip Galvanizing*. M.A.Sc. thesis, McMaster University.
- Cvijovic, I., Parezanovic, I., & Spiegel, M. 2006, *Corrosion Science*, 48, pp. 980–993.
- Drillet, P., Zermout, Z., Bouleau, D., Mataigne, J., & Claessens, S. 2004, *Proceedings of Galvatech '04*, Chicago, Il, pp. 1123–1134. AIST.

- Dubois, M. 1998. Mn in the galvanized coating. In F. E. Goodwin (Ed.), *Zinc-Based Steel Coating Systems: Metallurgy and Performance*, pp. 39–50. Warrendale, PA: The Minerals, Metals and Materials Society (TMS).
- Ebrill, N., Durandet, Y., & Strezov, L. 2000, *Metallurgical and Materials Transactions B*, 31B, pp. 1069–1079.
- Foord, J. S., Jackman, R. B., & Allen, G. C. 1984, *Philosophical Magazine A: Physics of Condensed Matter: Structure, Defects and Mechanical Properties*, 49, pp. 657–663.
- Franzen, H. F., Umana, M. X., McCreary, J. R., & Thorn, R. J. 1976, *Journal of Solid State Chemistry*, 18, pp. 363–368.
- Frenznick, S., Statmann, M., & Rohwerder, M. 2004, *Proceedings of Galvatech '04*, Chicago, Il, pp. 411–417. AIST.
- Garandet, J. P., Drevet, B., & Eustathopoulos, N. 1998, *Scripta Materialia*, 38, pp. 1391–1397.
- Ghosh, G. & Olson, G. B. 1994, *Acta Metallurgica et Materialia*, 42, pp. 3361–3370.
- Guttman, M. 1994, *Materials Science Forum*, 155-6, pp. 527–548.
- Guttman, M., Leprêtre, Y., Aubry, A., Roch, M. J., Morea, T., Drillet, P., Maigne, J. M., & Baudin, H. 1995, *Proceedings of Galvatech '95*, Chicago, Il, pp. 295–307. AIST.
- Hashimoto, I., Saito, K., Nomura, M., Yamamoto, T., & Takeda, H. 2003, *Tetsu-to-Hagané*, 89, pp. 31–37.
- Huin, D., Saint-Raymond, H., Loison, D., Bertrand, F., & Cornu, M. J. 2004, *Proceedings of Galvatech '04*, Chicago, Il, pp. 1135–1144. AIST.
- Jordan, C. E. & Marder, A. R. 1998, *Metallurgical and Materials Transactions B: Process Metallurgy and Materials Processing Science*, 29, pp. 479–484.

- Jordan, C. E., Zuhr, R., & Marder, A. R. 1997, *Metallurgical and Materials Transactions A: Physical Metallurgy and Materials Science*, 28, pp. 2695–2703.
- Khondker, R., Mertens, A., & McDermid, J. R. 2007, *Materials Science and Engineering: A*, 463, pp. 157–165.
- Liu, Y. & German, R. M. 1996, *Acta Materialia*, 44, pp. 1657–1663.
- Liu, Y. H. 2006, *Metallurgical and Materials Transactions A: Physical Metallurgy and Materials Science*, 37A, pp. 2767–2771.
- Marder, A. R. 1989. Microstructural characterization of zinc coatings. In F. E. Goodwin (Ed.), *Zinc-Based Steel Coating Systems: Metallurgy and Performance*, pp. 55–82. Warrendale, PA: The Minerals, Metals and Materials Society.
- Marder, A. R. 2000, *Progress in Materials Science*, 45, pp. 191–271.
- Marmur, A. 1996, *Colloids and Surfaces A: Physicochemical and Engineering Aspects*, 116, pp. 55–61.
- McDermid, J. R., Kaye, M. H., & Thompson, W. T. 2007, *Metallurgical and Materials Transactions B: Process Metallurgy and Materials Processing Science*, 38B, pp. 215–230.
- Menéndez, A., Pereiro, R., Bordel, N., & McDermid, J. R. 2007, *Journal of Analytical Atomic Spectrometry*, 22, pp. 411–414.
- Nakano, J., Malakhov, D. V., Yamaguchi, S., & Purdy, G. R. 2007, *Calphad: Computer Coupling of Phase Diagrams and Thermochemistry*, 31, pp. 125–140.
- Nishiyama, Z. 1978. *Martensitic Transformation*, Chapter Introduction to Martensity and Martensitic Transformation. New York: Academic Press.
- Oleford, I., Leijon, W., & Jelvestam, U. 1980, *Applications of Surface Science*, 6, pp. 241–255.

- Oren, E. C. & Goodwin, F. E. 2004, Proceedings of Galvatech '04, Chicago, Il, pp. 737–749. AIST.
- Renaux, B. & Sylvestre, A. 1989, Proceedings of 2nd International Conference on Zinc Coated Steel Sheet, Tokyo, Japan, pp. SB3/1–SB3/6. ISIJ.
- Roach, S. J. & Henein, H. 2005, Metallurgical and Materials Transactions B: Process Metallurgy and Materials Processing Science, 36, pp. 667–676.
- Rocha, R. O., Melo, T. M. F., Pereloma, E. V., & Santos, D. B. 2005, Materials Science and Engineering A, 391, pp. 296–304.
- Shi, L. 2004, Proceedings of Galvatech '04, Chicago, Il, pp. 241–247. AIST.
- Speich, G. R. & Miller, R. L. 1979. Mechanical properties of ferrite-martensite steels. In R. A. Kot and J. W. Morris (Eds.), *Structure and Properties of Dual-Phase Steels*, pp. 145–182. New Orleans, LA.: The Metallurgical Society of AIME.
- Strohmeier, B. R. & Hercules, D. M. 1984, Journal of Physical Chemistry, 88, pp. 4922–4929.
- Sun, S. & Pugh, M. 2000, Materials Science and Engineering A, 276, pp. 167–174.
- Swisher, J. H. 1970. Internal oxidation. In *Oxidation of Metals and Alloys*, pp. 235–267. Metals Park, OH: American Society for Metals.
- Tanaka, T., Nishida, M., Hashiguchi, K., & Kato, T. 1979. Formation and properties of ferrite plus martensite dual-phase structures. In R. A. Kot and J. W. Morris (Eds.), *Structure and Properties of Dual-Phase Steels*, pp. 221–241. New Orleans, LA.: The Metallurgical Society of AIME.
- Tang, N. 1989. Thermodynamics and kinetics of alloy formation in galvanized coatings. In F. E. Goodwin (Ed.), *Zinc-Based Steel Coating Systems: Metallurgy*

and Performance, pp. 55–82. Warrendale, PA: The Minerals, Metals and Materials Society (TMS).

Thorning, C. & Sridhar, S. 2007, *Philosophical Magazine*, 87, pp. 3479–3499.

Vanden Eynde, X., Servais, J. P., & Lamberigts, M. 2002, *Surface and Interface Analysis*, 33, pp. 322–329.

Vanden Eynde, X., Servais, J. P., & Lamberigts, M. 2003, *Surface and Interface Analysis*, 35, pp. 1004–1014.

Wagner, C. 1959, *Z Elektrochem*, 63, pp. 772–790.

Wang, H., Gao, F., Ma, X., & Qian, Y. 2006, *Scripta Materialia*, 55, pp. 823–826.

Wei, J., Nagarajan, N., & Zhitomirsky, I. 2007, *Journal of Materials Processing Technology*, 186, pp. 356–361.

Wetzig, K., Baunack, S., Hoffman, V., Oswald, S., & Präbeler, F. 1997, *Journal of Analytical Chemistry*, 358, pp. 25–31.

Young, T. 1805, *Philosophical Transactions of the Royal Society of London (1776-1886)*, 95, pp. 65–87.

Zhao, J. 1992, *Materials Science and Technology*, 8, pp. 997–1003.

Appendix A

Continuous Cooling Transformation Diagrams

The following are the continuous cooling transformation (CCT) diagrams generated for each alloy explored in this study for a range of cooling rates from the most rapid available with He ($\sim 150^{\circ}\text{C}\cdot\text{s}^{-1}$) to slow, controlled cooling using the induction furnace present in the dilatometer ($1^{\circ}\text{C}\cdot\text{s}^{-1}$ and in some cases $0.5^{\circ}\text{C}\cdot\text{s}^{-1}$).

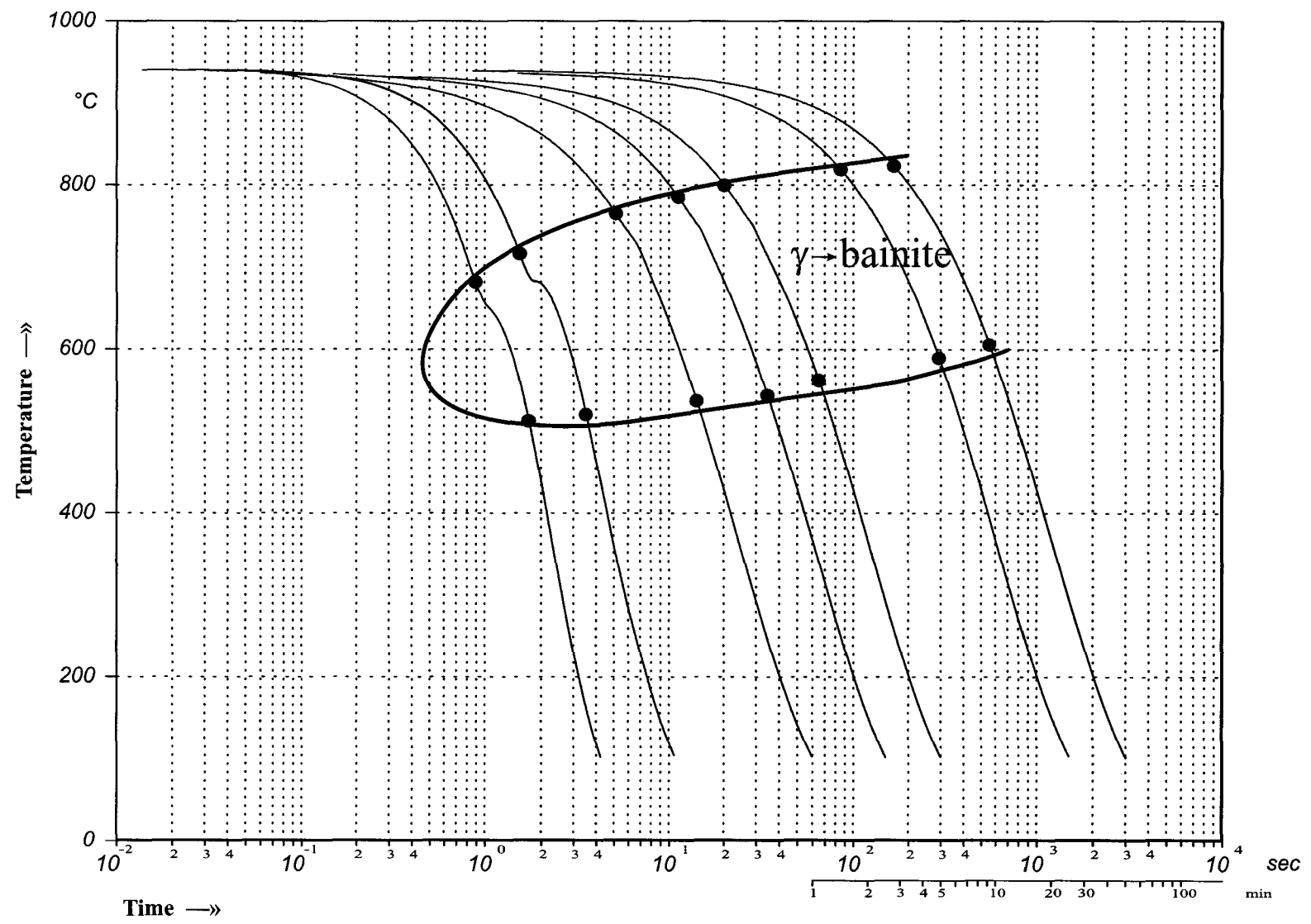


Figure A.1: CCT diagram generated from dilatometry for CMn alloy.

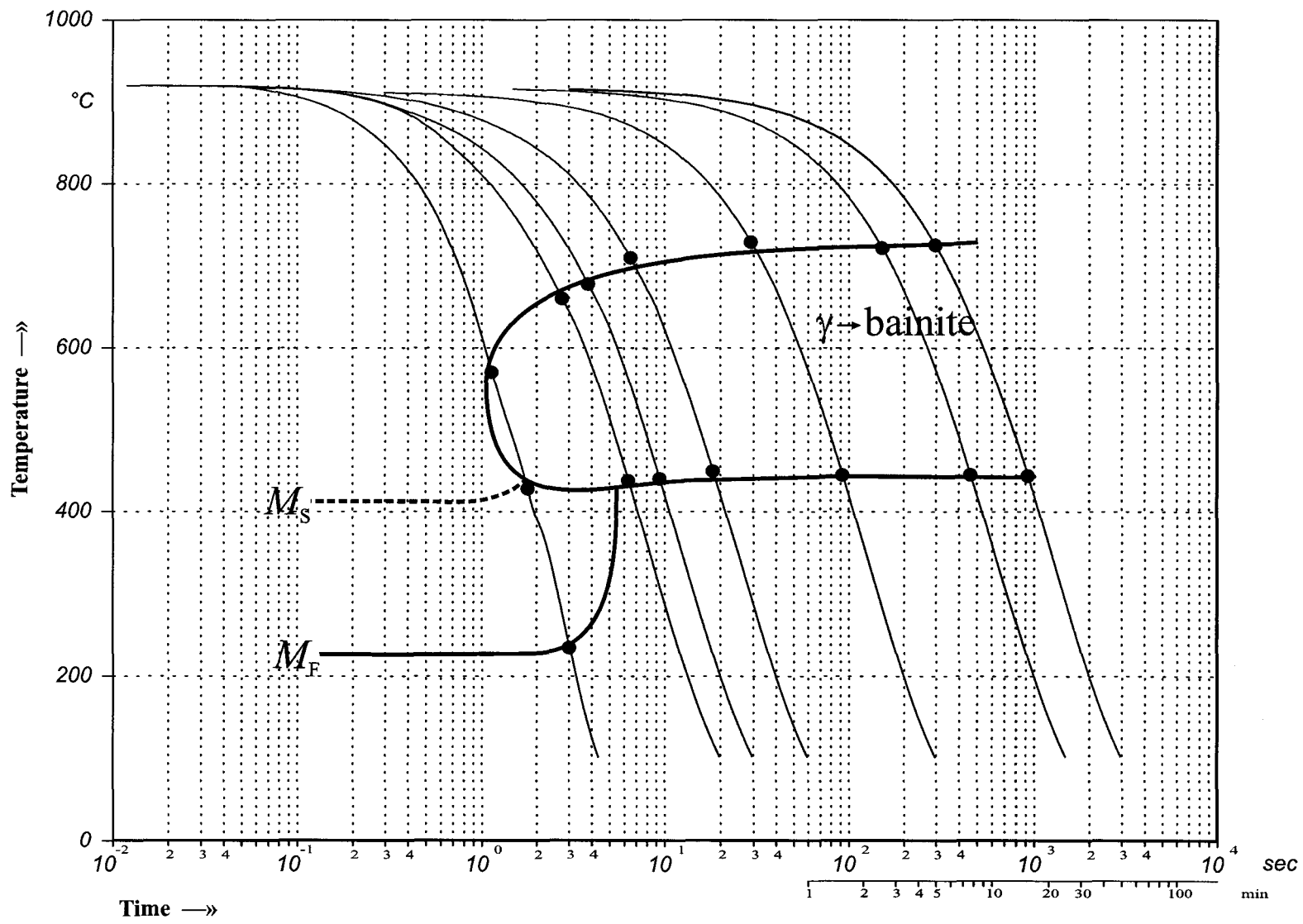


Figure A.2: CCT diagram generated from dilatometry for DP590 alloy.

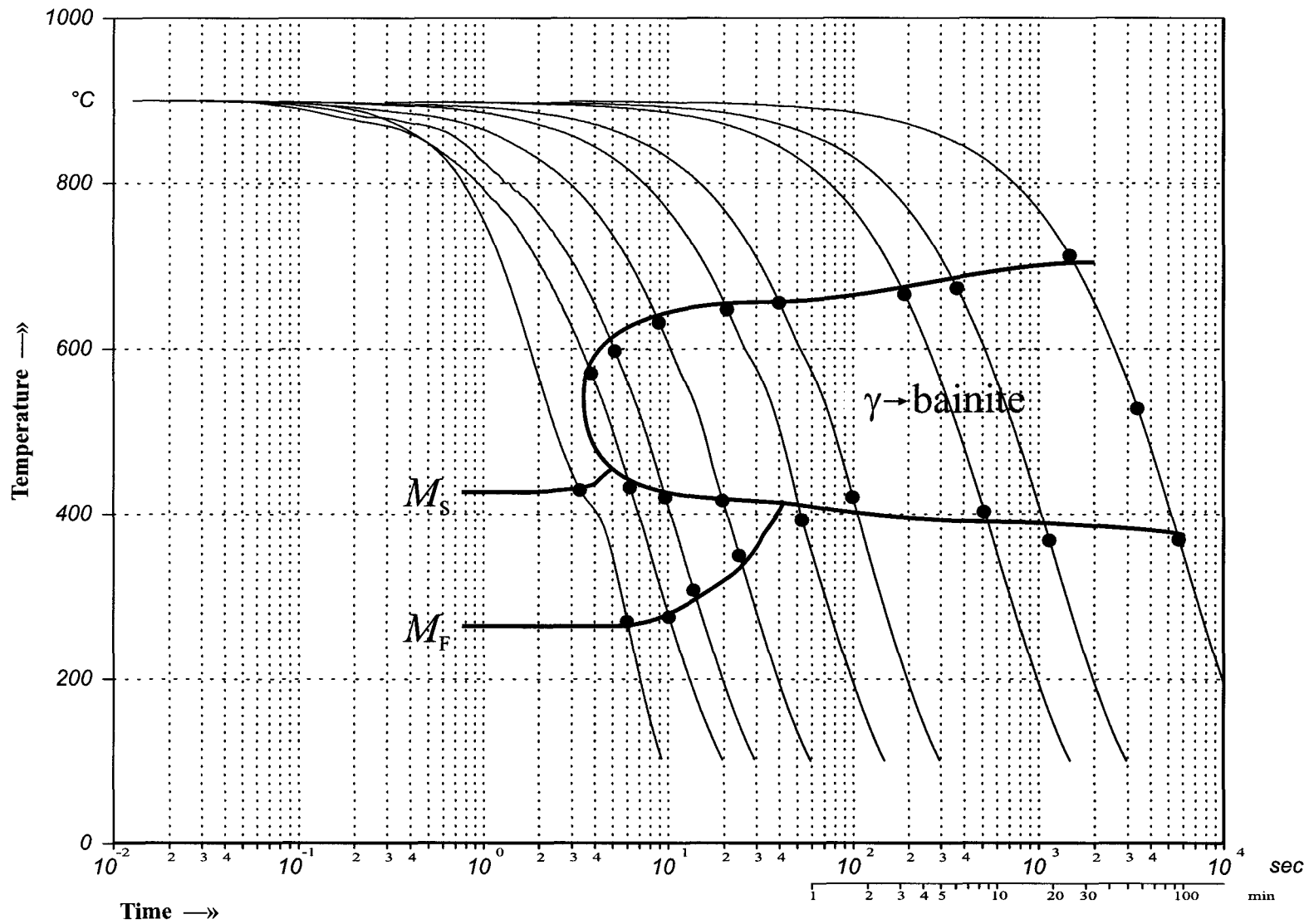


Figure A.3: CCT diagram generated from dilatometry for DP-1 alloy.

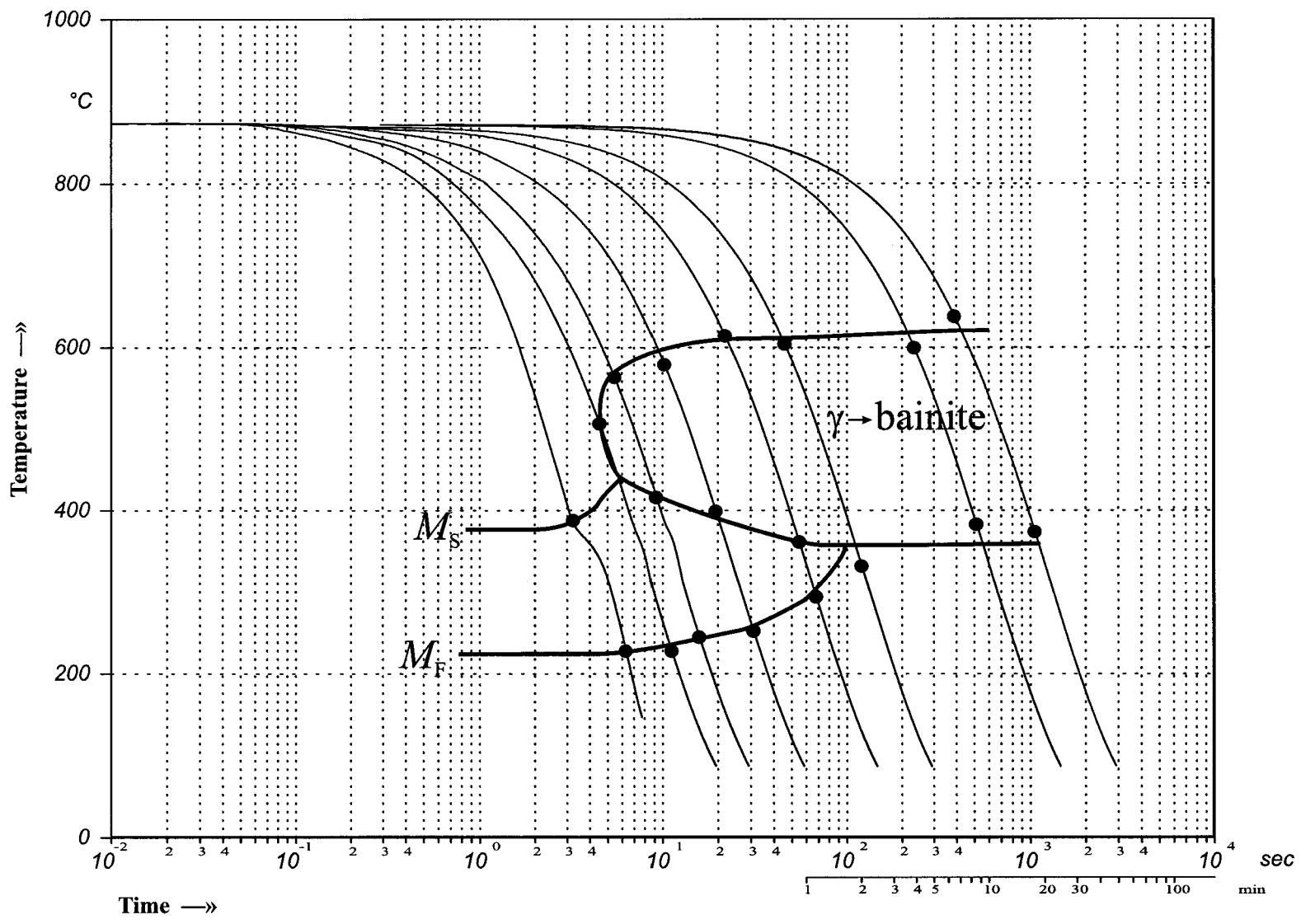


Figure A.4: CCT diagram generated from dilatometry for DP-2 alloy.

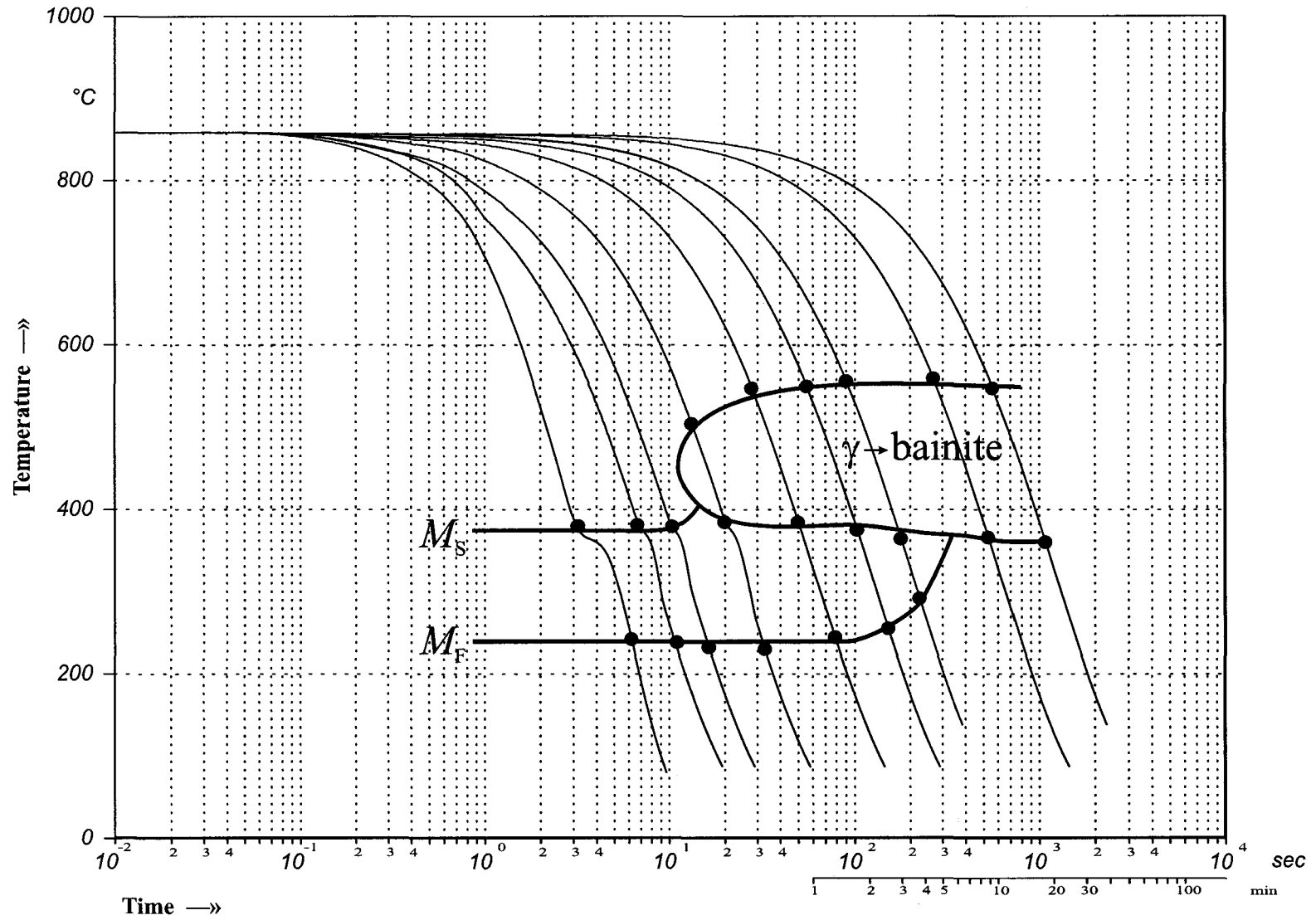


Figure A.5: CCT diagram generated from dilatometry for DP-3 alloy.

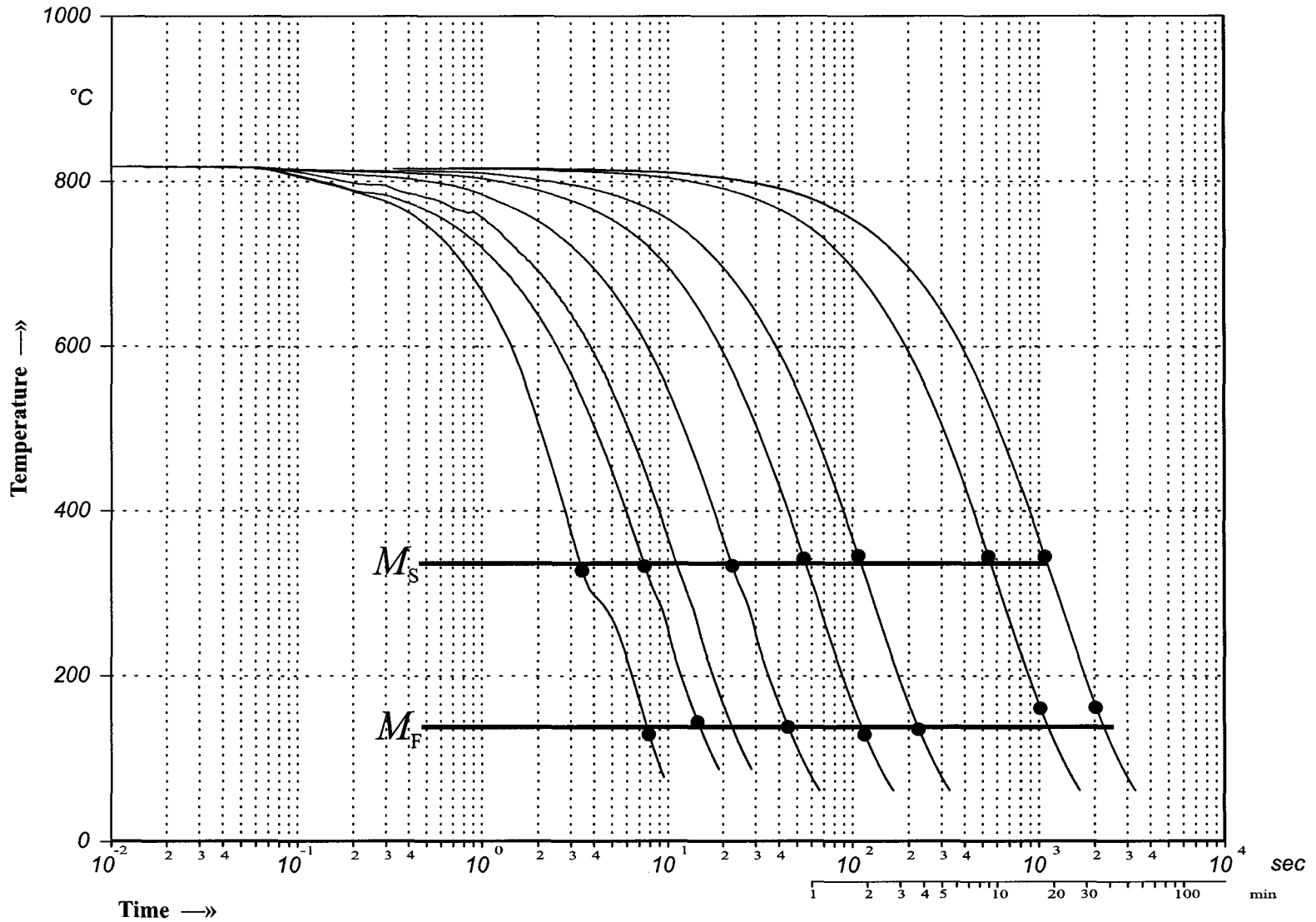


Figure A.6: CCT diagram generated from dilatometry for DP-4 alloy.

Appendix B

Initial Wetting Force as a Measure of Reactive Wetting

To reduce the data and obtain a kinetic parameter which could be compared between alloy systems, the obvious choice is to use the gradient of the wetting curves – after conversion to wetting force ($\gamma_{LV}\cos\theta$). Unfortunately, without values for γ_{LV} this is not possible because the gradient does not reflect the position of curves as shown in figure 5.22 which is a measure of the contact angle, and therefore how far the reaction has progressed. Since the only component of F_{measured} which changes over time is F_{wetting} , the following can be written:

$$\frac{\partial F_{\text{measured}}}{\partial t} = P\gamma_{LV} \frac{\partial(\cos\theta)}{\partial t} = P\gamma_{LV} \frac{\partial(\cos\theta)}{\partial\theta} \cdot \frac{\partial\theta}{\partial t} = P\gamma_{LV}(-\sin\theta) \frac{\partial\theta}{\partial t} \quad (\text{B.1})$$

and subsequently,

$$\frac{\partial\theta}{\partial t} = -\frac{\partial F_{\text{measured}}}{\partial t} \cdot \frac{1}{P\gamma_{LV}\sin\theta} \propto -\frac{\partial F_{\text{measured}}}{\partial t} \cdot \frac{1}{\sin\theta} \quad (\text{B.2})$$

Not only do equations B.1 and B.2 contain γ_{LV} , but also θ – implying that the gradients of F_{measured} and θ are dependent on the instantaneous contact angle which can only be calculated with γ_{LV} . Calculation of the instantaneous contact angle for

different values of γ_{LV} are shown in figure B.1 illustrating its effect on not only the value of θ , but also $\frac{\partial\theta}{\partial t}$ even with small variations.

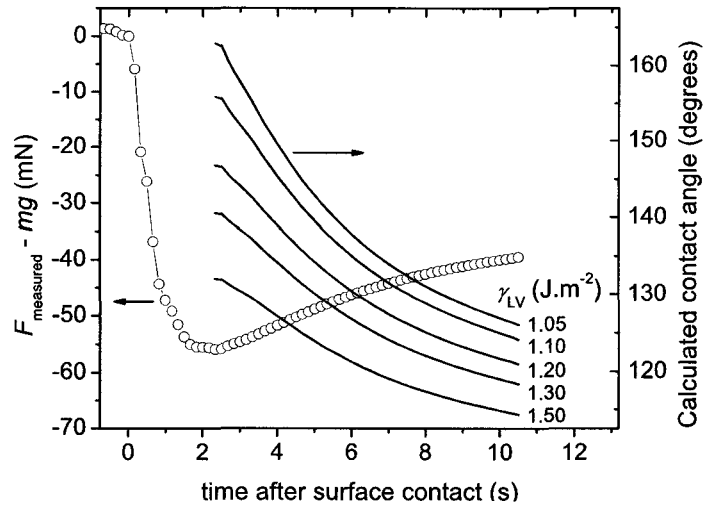


Figure B.1: Effect of γ_{LV} on contact angle calculation and subsequent value of $\frac{\partial\theta}{\partial t}$.

This is further illustrated with a plot of $\frac{\partial\theta}{\partial t}$ vs. θ in figure B.2 showing that at larger values of θ , the impact is the most significant – and this is a reflection of the case in early stages of reactive wetting. Therefore, without an accurate assessment of γ_{LV} , $\frac{\partial\theta}{\partial t}$ cannot be calculated with any certainty. Instead, since the wetting curves between alloys and conditions tend not to cross, an assessment of the reaction at any particular moment in time can be quoted and compared as a metric of the degree of wetting – and since it is an absolute measurement rather than incremental it can even act as a measure of the kinetics to that point.

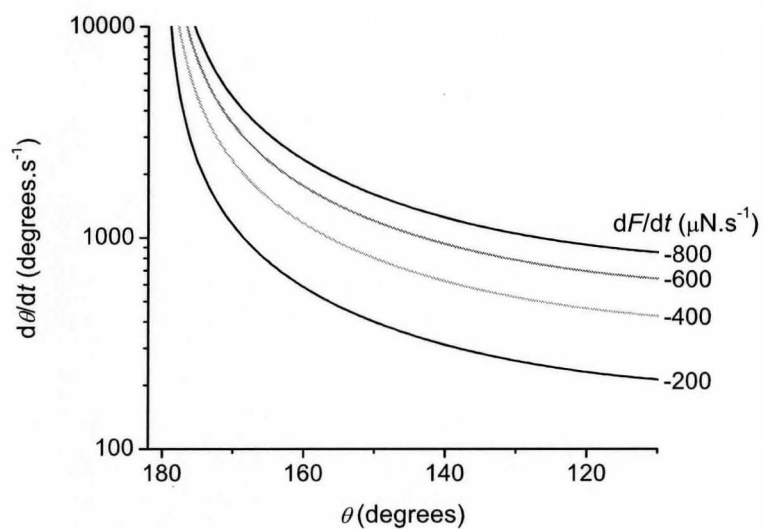


Figure B.2: Effect of θ on the calculated rate of contact angle evolution ($\frac{\partial\theta}{\partial t}$).

Appendix C

Measurements and Analysis Using a Force Balance

To do an analysis and explicitly quantify data pertaining to the contact angle, it must first be assumed that the contact angle is fixed across the width of the plate. This is reasonably valid, and would be increasingly valid with a wider sample because the edges do show an increase in the liquid height when compared to the cold-rolled surface.

From figure 5.25 or 5.26 it can be seen that DP-4 exhibited improved wettability at the -50°C dew point over alloys with much less Mn. This seems counterintuitive as under identical conditions, an alloy with more Mn would have a thicker oxide after annealing and decreased wettability. This can be explained by looking at the time required to reach a minimum value of F_{measured} .

Since, as mentioned previously, all samples were dipped at $15\text{mm}\cdot\text{s}^{-1}$ to a depth of 8mm, the time from surface contact to the final depth was $\approx 0.533\text{s}$. This time should also correspond with the minimum force measured with the electrobalance because the contact angle will be the largest when first dipped in the bath and decrease as the exposure time is increased. As shown in figure C.1, none of the alloys exhibited a minimum at 0.533s and the time required for the electrobalance to measure the minimum force increased with sample thickness. The reason for this

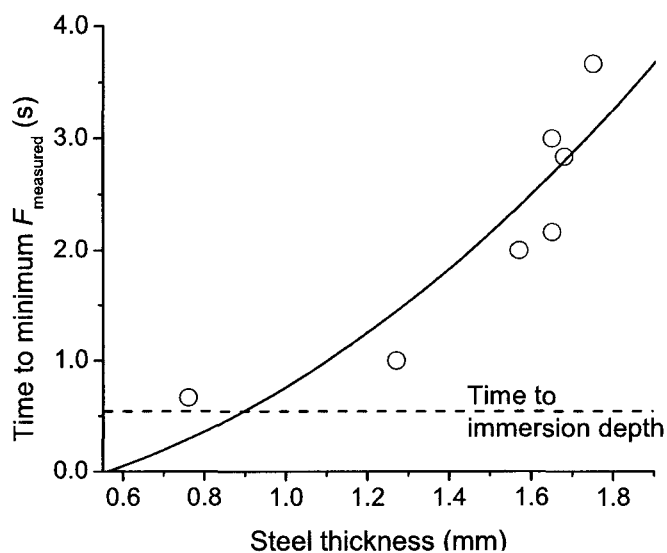


Figure C.1: Effect of substrate thickness on the dynamic response of the electrobalance during dipping; measured as the time required to reach minimum in F_{measured} .

is that the balance contains safeguards to dampen changes in the force which could adversely effect the signal:noise ratio. This was accomplished via a dashpot, labeled in figure 4.11, which prevents rapid changes in F_{measured} . This mechanism had a more significant impact on the thicker steels because when they were dipped, F_{buoyancy} was greater than that for the thinner steels. Coincidentally, the thickness of the steels also generally increased with Mn content – resulting in an increased initial contact angle, and increasing the magnitude of F_{measured} . The result is that the initial wetting force was perceived as being smaller (improved wetting) because by the time a measurement can be taken, more of the reaction had progressed - as illustrated in figure C.2. Therefore, alloys should not be compared directly with each other unless they are the same thickness during experiments.

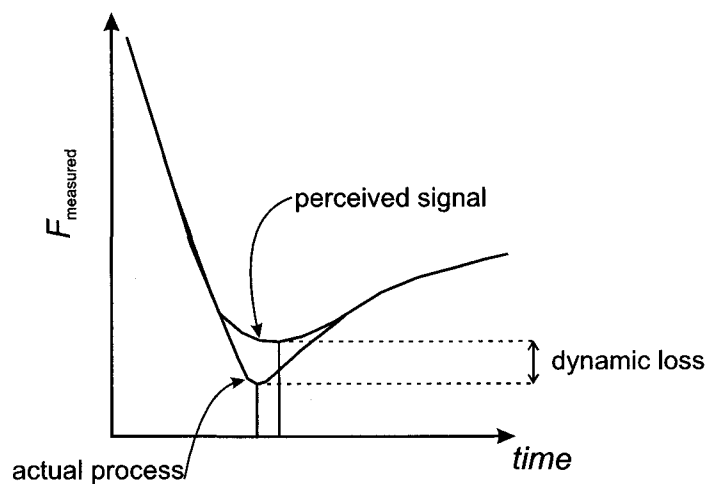


Figure C.2: Illustration of dynamic loss in the F_{measured} signal with thicker substrates. Subsequently, thicker samples exhibit an erroneous improvement in wettability.